UNIVERSITY OF STRATHCLYDE

FACULTY OF ENGINEERING

Electronic and Electrical Engineering

Dielectric Exploration and PD Detection in High Voltage Insulation

By

Abdul Samad

Thesis for the degree of Doctor of Philosophy

June 2024

Declaration of Authorship

This thesis is the result of the author's original research. It has been composed by the author and has not been previously submitted for examination which has led to the award of a degree.

The copyright of this thesis belongs to the author under the terms of the United Kingdom Copyright Acts as qualified by University of Strathclyde Regulation 3.50. Due acknowledgement must always be made of the use of any material contained in, or derived from, this thesis.

Signed………Abdul Samad…………………………

Date: ………04-06-2024……………………………

Acknowledgements

First of all, I would like to express my sincere and deepest thanks to Prof. Siew who was the main supervisor until December 2022 and Dr. Given from Jan 1st, 2023, following the retirement of Prof. Siew, for their expert guidance and encouragement. I am grateful for their insightful advice, understanding and patience in helping me for the completion of this thesis. Special thanks are dedicated to Prof. J. Liggat for sharing the knowledge on materials processing and experimental techniques, and Dr. Igor Timoshkin and many of the High Voltage Laboratory members for providing their opinion, discussion and technical support when undertaking my experimental works. I am grateful to the University of Strathclyde for awarding the Student Excellence Award (SEA) to partially fund my PhD. Moreover, financial assistance from the University of Strathclyde for my research works and conference attendance is kindly acknowledged as well.

Last but not least, I would like to thank my parents, my wife, my whole family, and friends for continuous and unconditional love and support. Dear God, the journey of my PhD was not an easy one, but I put my faith in you. At times when I was flooded with endless problems, you made ways out of no way. I shall always remember that in my heart I plan my course, but you determine my steps. Thank you for the abundant blessings in my life.

ABSTRACT

Polymeric materials degrade over time, leading to insulation failures. Finding new materials with strong dielectric properties and robust mechanical strength is crucial for reliable electricity supply. These materials must address defects from manufacturing faults, water tree traces, or mechanical stresses. Polyurethane (PU) is known for its self-healing properties, notably its ability to recover from surface dents due to high elasticity. However, self-healing decreases with increased hardness. This study investigates PU's dielectric breakdown properties at varying hardness levels, revealing an increase in breakdown strength with hardness. Balancing hardness and self-healing are essential, providing insights into PU's dielectric properties. In parallel to engineering novel insulating materials, detecting defects early is crucial to prevent deterioration from partial discharges (PDs). Detecting PDs using acoustic emission (AE) signals is not fully explored for cable insulation. Therefore, the study investigates acoustic pulse propagation from PD events in polymer using finite element methods (FEM) in COMSOL. An analytical model in MATLAB quantifies the impact of multiple propagation paths in a cylinder, aided by a Perfect Matched Layer (PML) in the COMSOL model for reflection-free modelling. The models reveal that acoustic pulse magnitudes decrease rapidly with distance, following the inverse square law. Moreover, the study also explores the effects of PU hardness on the propagation characteristics of the AE signal, revealing a high decay rate in AE signal peak magnitude and energy with increasing PU hardness. Frequency spectra analysis indicates stronger attenuation of higher frequency components with distance. The study's revelations on the impact of PU hardness on AE signal characteristics provide engineers with valuable insights for material selection in high voltage systems and applying the AE detection technique to locate the PD events. Industries stand to benefit from material choices, leading to enhanced system reliability and potential cost savings in maintenance.

Contents

List of Figures

xviii

List of Tables

List of Appendices

Appendix 1:

Appendix 2:

List of Acronyms

Acoustic Emission	AE
crossed-link polyethene	XLPE
Current Transducer	CT
Differential Scanning Calorimetry	DSC
direct current	DC
Dissolved Gas Analysis	DGA
Ethylene Propylene Rubber	EPR
Fast Fourier Transform	FFT
Finite Element Analysis	FEA
Fourier Transform Infrared Spectroscopy	FTIR
Gas-Insulated Switchgear	GIS
high frequency current transducer	HFCT

high voltage	HV
high voltage alternating current	HVAC
high voltage direct current	HVDC
high-density polyethylene	HDPE
linear low-density polyethylene	LLDPE
low-density polyethylene	LDPE
medium-density polyethylene	MDPE
Nylon 6,6	Nylon
partial discharge	PD
pico coulombs	pC
polyethylene	PE
polypropylene	PP
polytetrafluoroethylene	PTFE

Polyurethane	PU
Siemens per meter	S/m
time difference of arrival	TDOA
time of arrival	TOA
Ultra high molecular weight	UHMW
ultra-high frequency	UHF

Polyurethane

Chapter 1

INTRODUCTION

The increasing demand for electricity has spurred a global expansion of electric power networks, necessitating innovative approaches to meet public energy demands while ensuring reliable generation, transmission, and distribution. In response, initiatives are underway to interconnect national grids across continents, forming a "super grid" primarily reliant on conventional energy sources. The European grid integration exemplifies strides towards a unified energy network, enhancing efficiency, reliability, and sustainability across nations. In contrast, the United States maintains three separate grids (Eastern, Western, and Texas) owing to historical, regulatory, and geographical nuances. However, this evolving infrastructure is adaptable to incorporate diverse energy types, including renewables like solar and wind. Key to its success are the installation of Extra High Voltage (EHV) and Ultra High Voltage (UHV) AC transmission lines. However, HVDC transmission is gaining more attraction than HVAC as the HVDC transmission provides technical advantages over EHV and UHV AC transmission, including lower transmission losses over long distances, increased transmission capacity, control of power flow, enhanced stability and reliability, and the ability to interconnect asynchronous power systems. These benefits make HVDC transmission particularly suitable for long-distance transmission, integration of renewable energy sources, cross-border power exchanges, and improving grid resilience and flexibility [1].

The transmission of electrical energy over long distances is a complex process that relies on various electrical components. In HVDC transmission system, one critical aspect of this process is the choice of cable insulation material. The insulation material plays a vital role in ensuring that power utilities operate safely and efficiently. However, the dielectric breakdown of the insulating materials can have serious consequences. This phenomenon can be caused by various factors, including electromechanical stress, thermal effects, tracking failure, and internal discharge within the insulating material. It is essential to note that evaluating solid dielectrics goes beyond assessing the magnitude of the applied voltage; the duration for which the voltage is applied is also crucial.

1.1 Research Background and Motivation

Historically, until 1960, ceramic materials and oil-impregnated paper were widely used for insulating high-voltage components due to their ability to withstand high electric fields and provide adequate insulation. However, these materials had limitations such as bulkiness, susceptibility to moisture, and limited mechanical flexibility, which restricted their applicability in modern electrical systems.

Polymeric materials, on the other hand, offer several advantages over traditional insulation materials. They are lightweight, flexible, and resistant to moisture, making them suitable for a wide range of applications. Additionally, polymeric materials can be tailored to specific performance requirements, offering enhanced dielectric properties and improved resistance to electrical and environmental stresses.

Therefore, the move from conventional ceramic and oil impregnated paper insulation to polymeric materials in 1960s has been a remarkable change in the field of high voltage insulation. Because of easier processing, high resistance to degradation, low cost, high operating temperature, and high dielectric strength, crossed-link polyethene (XLPE) is widely being used as an insulating material in high-voltage applications since 1980s [2-4]. XLPE is degraded by electric stress and water [5]. The water from residual moisture, environment, and surroundings penetrates the polymer and forms a water tree which, on drying, leaves behind its traces [6]. These channels or tubules provide the conducting path to the electric charges. Over time, this can lead to the initiation of partial discharge (PD) or the formation of electrical trees. Usually, water trees do not cause an insulation breakdown, but these can create PD or electrical trees, which are recognised as the primary factors contributing to insulation failure [7]. To overcome this problem, researchers tried to improve the manufacturing technology by adding water tree retardant materials as well as developing semi conducting materials with higher purity [8]. Further research revealed that not only can the traces of water trees initiate the formation of electrical trees, but the presence of protrusion or roughness of the surface of the polymeric insulation can also initiate the formation of electrical trees [9]. Moreover, at the interphase of different materials during the manufacturing of the power cables, the formation of voids or cavities cannot be entirely avoided. Under high electric stress, these voids can initiate the PDs or electrical trees, propagating through the insulation and causing the insulation breakdown [10, 11].

In the early 1990s, polymer nanocomposites were created by adding nanosized fillers to the polymer matrix. These composites improved the material's

mechanical strength and gained attention from various automobile industries [12-14]; however, their application in electrical insulating industries was initially overlooked. It wasn't until 1994 that Lewis [15] introduced the concept of incorporating nanometre-sized fillers into the polymer matrix, sparking interest in the potential property improvements that could benefit electrical insulation. The dispersion of the nanofillers such as nanoparticles or nano-clays, within the polymer matrix, exhibited improved dielectric, thermal, and mechanical properties [16]. Although polymer nanocomposites showed an improved dielectric performance in some cases but the opposite has also been reported where these nanofillers had adverse effects on the dielectric breakdown characteristics [17]. Nevertheless, the use of nanocomposites in electrical insulation is limited because of the challenges related to cost, manufacturing pure nanosized filler, and uniform dispersion of nanofillers in polymer matrix [17].

Therefore, exploring new insulation materials with good dielectric characteristics and robust mechanical strength is crucial to ensure reliability and continuous electric supply. These materials should also be capable of effectively addressing the defects that may arise due to manufacturing faults, the presence of water tree traces, or mechanical stresses. Polyurethane (PU) is a well-established family of material studied for its potential of self-healing capabilities. PU is composed of urethane repeating units. The synthesis of PU involves polymerising poly-isocyanates, macro polyols, and the inclusion of chain extenders [18-20]. The soft segments are the macro polyols, such as polyether or polyester polyol. In contrast, the isocyanates (aromatic or aliphatic) and chain extenders (small diols or diamines) are known as the hard segment. The hard phase in PU acts as physical linking points, contributing to the mechanical strength. Meanwhile, the flexible

polymer chains in PU provide them with the desired characteristics of flexibility and elasticity. Figure 1.1 shows the structure of the PU matrix where the soft segment highlighted by the blue lines connected with the orange rectangles which represent the hard segments while the green lines between the hard segments are the chain extenders. By carefully selecting the appropriate raw materials and adjusting the relative ratios of the hard and soft segments, the phase-separated structure can be easily modified, leading to variations in the properties of PU. Additionally, PU, like many other self-healing materials, faces a trade-off between mechanical strength and self-healing capacity, which can result in compromised restoration of mechanical properties after damage occurs [19].
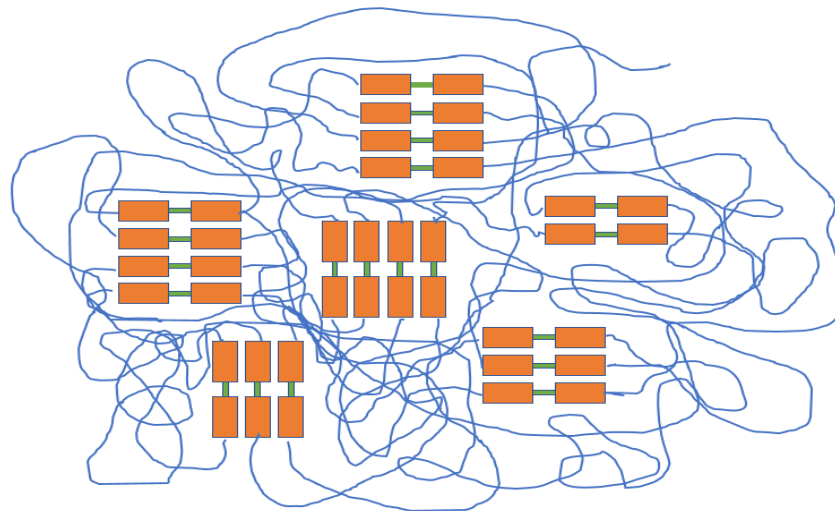
Figure 1.1: Structure of Polyurethane. Thin blue lines represent soft segment, orange rectangles hard segment, while green thick lines represent chain extenders.

The self-healing properties of PU may offer a compelling solution to mitigate the challenges associated with discharge initiation at defects such as voids or traces of water treeing. Through its self-healing capabilities, PU may effectively repair these defects and restore the structure of the insulation matrix. If successful, then

this unique characteristic will not only help to prevent the initiation of discharges but also will enhance the overall reliability and performance of the insulation system. However, a significant challenge lies in understanding the dielectric properties of PU. One of the aims of this study is to investigate the dielectric characteristics of PU with different levels of hardness, as this is closely linked to the self-healing capability of PU. Additionally, the dielectric breakdown characteristics of Nylon 6,6 (Nylon) and polypropylene (PP) were also examined. The inclusion of Nylon and PP in the study alongside PU variants serves the purpose of comparison among members of different polymeric families. Each material represents a distinct family of polymer with unique properties, and their examination allows for a thorough understanding of how different polymers, each with specific characteristics, respond to dielectric breakdown conditions.

Moreover, to ensure reliability and continuous electric supply, in parallel with the engineering of novel insulation materials, it is necessary to carry out suitable monitoring techniques to observe the life of the power cables. Numerous electrical methods, such as electromagnetic wave detection and individual discharge pulse measurement, have recently been utilised [21, 22] to detect PDs at the initial stage but these methods has limitations like electromagnetic signal can be masked by the background noise. Nevertheless, the initiation of PD due to cavity-type defects with regular geometries has been investigated and proved that the acoustic signal emitted is detectable within an audible frequency range [23]. The mechanism of such acoustic emission was explained by the vibration of the cavity wall caused by a PD event [23]. But, the acoustic emission (AE) detection technique is believed to be more appropriate for liquid and gas insulation systems and yet not fully applied on solid insulating materials [24]. Nevertheless, a new photonic-acoustic

technique has been introduced in recent past for partial discharge detection in polymeric insulation cables [23, 25]. However, the AE technique is advantageous because AE methods are non-invasive and acoustic signals are not affected from electromagnetic interference. Further, if two or more acoustic sensors are coupled, then the signal from the fault can be analysed to locate the source of PD by the time of arrival (TOA) method or the time difference of arrival (TDOA) method. Apart from these merits, there are some challenges in using this technique to assess cable insulation, i.e. AE signals generated by PD can be masked by background noise, such as electrical interference or mechanical vibrations. As a result, analysis of the actual AE signal becomes very complex. In cable insulation, the occurrence of multiple PD events within the same void or across multiple voids can initiate multiple acoustic signals which propagate through the insulation and can lead to complex interactions while propagating through the insulation known as constructive or destructive interference. These interactions result in variations in the amplitude, phase, and shape of the signal. Constructive interference amplifies the acoustic signal, enhancing its detectability, while destructive interference attenuates or distorts the signal, posing challenges for accurate PD detection and localization. Understanding and mitigating the effects of interference are crucial for reliable PD diagnosis and effective insulation condition assessment in high-voltage systems. Apart from this, the physical characteristics of the insulation materials also affects the propagation characteristics of the AE signals. The extent to which the physical characteristics of the material contribute to the damping of acoustic signal is unclear, as there has been a lack of thorough examination on this matter [26].

1.2 Problem Statement:

The continuous exploration and development of new insulating materials with better dielectric strength and diagnostic techniques for monitoring the insulation performance of HV cables is crucial. Various detection techniques have been introduced to detect PD in HV insulation systems. One of the well-established detection techniques is the acoustic technique, which is commonly used for the condition assessment of liquid-predominant insulation systems like high voltage transformers. However, this detection technique is not typically utilized in HV cables with solid insulation. Studies have revealed that PD caused by regularly shaped cavity defects emits an acoustic signal in both audible and higher frequency range [23, 27] which can be detected and used to locate the source of PD. However, the propagation characteristics of the acoustic signal emitted from the PD event are still unknown. Researchers refrained from experimentally testing the propagation of acoustic signals in cable insulation materials due to technical challenges which include the need for specialized equipment, difficulties in accessing the cable insulation, or limitations in accurately measuring acoustic signals within the insulation, resource constraints, and safety concerns associated with working with high-voltage materials. The advancements in technology such as improved acoustic sensing techniques and simulation software can help overcome these challenges. Additionally, developments in materials science and instrumentation have made it more feasible to conduct experiments on cable insulation materials with greater precision and safety. Therefore, exploration of the potential of the AE detection technique to detect and locate PD in cable insulation can be useful for industry.

Thus, this study aims to investigate the propagation characteristics of AE signals through PU rods with different levels of hardness which is intended for use as an insulating material along with Nylon and PP, while AE signals were initiated by an electrical discharge event. This analysis includes an exploration of how the physical attributes of these materials influence the transmission of AE signals. In addition, this research also examines the dielectric properties of PU variants. Comparisons are also made with Nylon and PP to assess the dielectric behaviour of different PU variants.

The research findings can contribute exploring the potential of the use of AE technique to detect and locate the source of PD event. Moreover, it also contributes towards the development of new insulating materials capable of healing the manufacturing faults like the formation of void or cavity within the insulation material to restore the uniform distribution of the electrical field across the insulation..

1.3 Objectives and Scope:

A two-pronged approach is essential to tackle the challenges in high voltage transmission cable insulation. Firstly, it involves the exploration and development of new insulating materials that possess improved dielectric strength while being capable of healing the defects i.e., voids, cavities, and traces of water treeing. Secondly, it entails investigating non-invasive techniques for early detection and localisation of faults in transmission cables. By combining these efforts, the continuity of the electric power supply can be ensured, and the reliability of the electric power network can be enhanced. Therefore, the main objectives of this research are:

i) To investigate the dielectric breakdown characteristics of PU with different hardness levels.

The self-healing capability is greatly influenced by the hardness of the PU. Therefore, this investigation entailed a detailed exploration of how the hardness variations in PU influence their behaviour when subjected to electrical breakdown conditions. The results of the study will help to achieve the intricate balance between hardness, self-healing capability, and dielectric strength of PU. In addition to PU variants, Nylon and PP were included in study as comparison materials.

ii) To model the propagation characteristics of the acoustic pulse in polymers emitted from an electrical discharge.

The propagation of acoustic pulse in polymers is mainly influenced by reflections and scattering. Therefore, analysis of the effects of reflections on the propagating acoustic pulse in polymeric materials were conducted using Finite Element Analysis (FEA) methods of COMSOL Multiphysics and MATLAB. The results will help the engineers and industries in quantifying the effects of reflections on the propagating acoustic pulse while detecting and locating the PD faults using AE methods.

iii) To investigate the propagation characteristics of an acoustic pulse from an electrical discharge event in polymeric materials.

The physical characteristics of the polymeric materials greatly influence the propagation capability of the AE pulse. Therefore, this study involved the analysis of the effects of the material hardness on the propagation characteristics of acoustic pulse, for instance, the impact of hardness on the magnitude of propagating acoustic pulse, propagation

velocity of the acoustic pulse, capability of the acoustic pulse to propagate through the material with different levels of hardness, impact of hardness of the material on energy dissipation of an acoustic pulse, and effects of hardness on the spectrum of the propagating acoustic pulse. The results provide the foundation for implementing the AE detection technique to detect and locate PD events in cable insulation.

1.4 Significance of the Research

The significance of this research holds far-reaching implications for both academia and industry. One notable aspect is the positive correlation between the hardness of PU and its dielectric breakdown strength, indicating an increase in dielectric strength with higher hardness levels in PU. Based on these observations, engineers from academia and industry can further explore the delicate balance between the dielectric strength and self-healing capabilities of PU to design and implement a new high voltage insulating materials for underground power cables and cable joints. This innovation could lead to enhanced efficiency and reliability in various electrical systems, contributing to the broader field of electrical engineering.

Additionally, it introduces a model designed to measure and understand the effects of acoustic reflections and scattering. This model serves as a tool to quantitatively assess the impact of scattering and reflections when interpreting the acoustic signals obtained while locating the source of PD using the AE technique in underground power cables, cable joints and transformer oil. This has practical relevance for both the power industry and engineers. The ability to detect and

locate faults using acoustic signals could improve maintenance practices in power systems, thereby promoting a more reliable and resilient electrical infrastructure.

Furthermore, practical considerations such as cable structure and sensor attachment play crucial roles in the effectiveness of AE-based fault detection methods. Understanding how the structure of the cable and the placement of sensors influence signal propagation and reception is essential for optimizing fault detection accuracy. Moreover, the presence of metallic objects like rail lines near the cable can introduce additional complexities, potentially interfering with signal transmission and reception. Thus, researchers and engineers must account for such external factors when designing and implementing AE-based fault detection systems for underground power cables.

1.5 Contribution of Research

The project delved into two aspects of electrical insulation and fault detection, yielding significant contributions to both understanding and practical application. First, it focused to investigate the dielectric properties of PU with different levels of hardness. The results revealed a noteworthy trend: as the hardness of PU increased, its dielectric properties exhibited improvement. However, this enhancement can come with a caveat; the higher hardness levels may potentially compromise self-healing capabilities of PU. These insights are invaluable for engineers and industries, offering guidance in selecting optimal materials for cable insulation or joints, while also exploring the delicate balance between dielectric strength and self-healing abilities.

In parallel, the project explored the application of the AE technique for detecting and locating PD in cable insulation. This involved a comprehensive investigation encompassing both simulation and experimental work. Initially, the propagation characteristics of acoustic pulses in cylindrical rods were simulated, resembling HVDC cable structures, using COMSOL Multiphysics. These simulations resulted in a distorted pulse due to reflections from the radial boundary. Additionally, a MATLAB model was developed to understand the impact of reflections on propagating AE pulses, further refining fault detection methodologies. Further, the implementation of PML to mitigate the reflections can be useful for engineers and researchers while analysing the AE signal propagation without the reflections.

Moreover, the project contributed novel experimental setups for studying AE signals in cable insulation at a laboratory scale. By employing cylindrical polymeric rods similar to cable structures, enabled to establish a platform for in-depth analysis of AE phenomena and assess the suitability of AE emission techniques for PD detection and localization. Although the significant drop in AE signal magnitude in polymers was observed, limiting its effectiveness for detecting PD in cable insulation. However, its use to detect and locate faults in cable joints cannot be ruled out.

1.6 Thesis Outline

This thesis is divided into 10 chapters.

Chapter 1 Contains the introduction, Research background, objectives and scope, and significance of research.

Chapter 2 Provides a review on the polymeric insulating materials and PD detection techniques being applied in industry and challenges related to these.

Chapter 3 Provides the details of modelling the acoustic pulse in MATLAB and COMSOL Multiphysics. While Chapter 4 Present the comprehensive outcomes and discussion from the modelling of acoustic pulse propagation characteristics.

Chapter 5 Provides an insight into the experiments used throughout this research.

Chapter 6 to 9 contains a detailed analysis of the materials used in this research. This includes the structural and morphological characterisation of polymers used in the research (Chapter 6), Dielectric spectra and DC conductivity measurement of all the polymers (Chapter 7), Dielectric breakdown strength of polymers (Chapter 8), and propagation characteristics of an acoustic pulse from discharge in Nylon, PP and PU with different levels of hardness (Chapter 9).

Chapter 10 contains the conclusions and recommendations for the future work.

Chapter 2

Review of polymeric insulations and fault detection techniques

2.1 Introduction

This chapter explores the background knowledge and understanding of polymeric insulating materials, encompassing their electrical characteristics. The advantages and shortcomings of each material, including polyethylene (PE), XLPE, epoxy resins, and PU, are reported based on existing literature. Emphasis is placed on PU, this study's primary material of interest.

Furthermore, the chapter examines common failure reasons for cable insulation. It also explores various detection techniques employed to identify and locate faults, namely electrical, chemical, and acoustic methods. The advantages and limitations of each technique are thoroughly explained, with particular attention given to the acoustic detection technique, which is the focus of this study.

2.2 Polymeric insulating materials

Polymeric insulating materials are critical in ensuring the safety, reliability, and efficient operation of the HV electrical system. With the increasing demand for electricity and the continuous expansion of HV transmission and distribution networks, there is a growing need for advanced polymeric materials that offer enhanced electrical insulation properties, improved performance, and increased reliability. Polymeric materials offer several advantages over traditional insulating

materials like porcelain or glass in HV power transmission and distribution networks. These advantages include their lightweight nature, ease of manufacturing, excellent dielectric properties, and the ability to be moulded into complex shapes. Moreover, polymeric materials resist environmental factors such as moisture, UV radiation, and pollution, making them suitable for most of outdoor and indoor HV installations [28].

The performance requirements for insulating materials in HV applications are stringent. These materials must withstand high electric fields, exhibit low dielectric losses, possess good thermal stability, and have sufficient high mechanical strength to endure the stresses associated with electrical operations. Additionally, considerations such as long-term ageing effects, which encompass factors like degradation of insulation properties over time due to environmental exposure, electrical stress, and thermal cycling, must be carefully evaluated. Moreover, compatibility with other components in the insulation system, including adhesives, coatings, and structural elements, is essential to ensure seamless integration and optimal performance of the overall electrical insulation system.

Over the past decade, significant progress has been made in developing polymeric insulating materials with enhanced performance characteristics. Researchers have explored novel material chemistries, including nanocomposites, blends, and hybrid systems, to improve their electrical and mechanical properties [29, 30]. Advances in polymer synthesis, processing techniques, and surface modification of the polymers resulted in improved breakdown strength, reduced partial discharge activity, and increased resistance to tracking and erosion in insulating materials [31-33].

However, despite these advancements, there are still several challenges being faced by industry and researchers. For example, achieving a delicate balance between improving electrical properties and maintaining other essential characteristics such as mechanical strength, thermal stability, and long-term reliability is complex. Understanding degradation mechanisms, including electrical, thermal, and environmental ageing, is still evolving. Moreover, the standardisation of testing methods and the establishment of reliable performance evaluation criteria for polymeric insulating materials are ongoing research areas. Below is a summary of frequently employed polymeric materials for high voltage insulation applications and the difficulties linked with their utilisation.

2.2.1 Polyethylene

Polyethylene belongs to the polyolefin family, which are higher molecular weight hydrocarbons. The polyethylene family includes linear low-density polyethylene (LLDPE), low-density polyethylene (LDPE), medium-density polyethylene (MDPE), high-density polyethylene (HDPE), Ultra high molecular weight polyethylene (UHMW), and XLPE. During the polymerisation of ethylene, straight chains of polymers are formed. Branching can occur from these chains. The varying degree of these branches in molecular structure defines the classification of polyethylene.

Figure 2.1 shows the structures of the members of polyethylene family. HDPE has a linear structure with the lowest amount of side chains which are also short in length. This allows free movement of the polymer molecules and allows dense crystalline structures to form in the polymer. Similarly, UHMWPE is similar in structure to HDPE but has longer backbones and thus a higher molecular weight.

Moreover, LLDPE has a similar structure to HDPE but contains a higher number of side chains results in the formation of dense crystalline regions. Unlike LDPE, the chains of LLDPE can slide over each other when elongated without being entangled. This ensures higher tensile strength and higher puncture resistance as compared to LDPE.
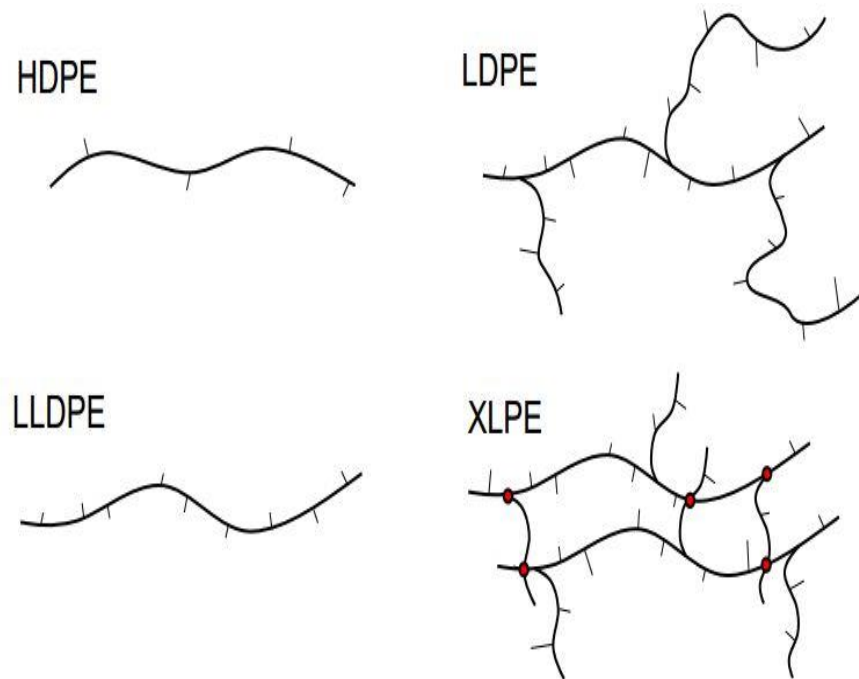
Figure 2.1: shows the polymerization structures of the different members of the polyethylene family [34].

Furthermore, XPLE is a high-density polyethylene that has covalent bonds between the polymer chains. These factors help the polymer to form 3-dimensional polymers with higher molecular weight. These bonds during polymerisation ensure that the polymer`s compact structure has better physical properties.

HV power cables are often insulated with polyethylene due to their excellent dielectric properties and affordability. However, the maximum operating temperature of the PE can limit its use. XLPE is an alternative option that can

improve the overload withstand temperature up to 140°C compare to PE which has 95° C, but may produce by-products during manufacturing that negatively impact dielectric properties. To combat this, the insulation must undergo a process to remove these by-products, which can be time-consuming and expensive. Considering this, researchers are exploring HDPE, which has a higher crystallinity and melting point to replace XLPE. However, it is important to note that residual metallic catalysts used during the synthesis of HDPE can impact the material's cleanliness, which can result in the synthesis of a non-uniform insulation matrix. During the service, the non-uniform insulation matrix results in a non-uniform distribution of the electric field and leads to insulation failure [35].

2.2.2   Epoxy Resins

Epoxy resins belong to the thermosetting polymers category, consisting of resins and hardeners. When these components are combined, they yield an end product with better dielectric properties, making them good for certain HV electrical insulations like bushings [36]. The curing or hardening process of epoxy resins involves mixing a curing agent or hardener with the resin, transforming the compounds into a thermoset form. During this process, the curing agents interact with the epoxide rings, creating robust covalent bonds, which predominantly define the resin's intended use.

One critical aspect of epoxy resins is their "pot life," which refers to the limited time availability after the initial mixing of the resin and hardener. During this window, the material must be applied to the intended job. As time progresses, the material's viscosity increases, rendering the mixture and it becomes useless if not utilised promptly. Careful attention to the pot life is essential to ensure practical

application and optimal performance of epoxy resins in electrical insulation applications [36].

2.2.3   Nanocomposites:

A composite material is "a multi-component material having different phase domains in which one type of phase domain is a continuous phase" [34]. The continuous domain is called the matrix, and the filler is the other phase. Polymeric hydrocarbons have a versatile processing portfolio, which allows the introduction of inorganic materials to enhance their physical and chemical properties. The fillers can be of different shapes and sizes. These physical characteristics of the filler, along with its distribution in the polymer matrix and interaction with the polymer, influence the physical and chemical properties of the composite material. Apart from the distribution of the filler, the interaction of the filler with the polymer matrix is a critical factor in defining the properties of the composite. The interaction of the filler with the polymer can occur at both atomic levels through hydrocarbons, van der Waals forces, or polar interactions and on a larger scale through surface roughness or mechanical interlocking. Any interaction between the filler and polymer matrix depends upon the surface area of the filler interacting with the polymer. Therefore, the filler size is the main influential factor in defining the properties of the composite. The smaller size of the filler provides more surface area per mass, due to which the influence of the interaction zone becomes more evident. If the filler size is 1-100 nm, it is usually called nanofiller, and the composite is called nanocomposite.

2.2.4   Surface Treatment of the Fillers:

Usually, the filler particles are immiscible in a polymer matrix, making it difficult to achieve a homogeneous dispersion of filler in the polymer matrix. Agglomeration of the fillers in the polymer matrix alters the properties of the composite. To overcome this problem, fillers are put under surface treatment. This results in the better distribution of the filler in the matrix, improving the adhesion between the polymer matrix and the filler, and the formation of the clusters is avoided. It is to be noted that the thickness of the modified layer plays a vital role in defining the properties of the composite. The most used techniques for the surface treatment of the filler are the plasma technique, grafting of the functional polymeric molecules to the hydroxyl groups existing on the particle surface, and chemical treatment of the particle's surface [37]. These techniques make the surface of the particles more conducive to adhesion to the polymer.

Usually, different silane coupling agents are used to do the chemical treatment of the particle's surface. These silane coupling agents can react with the hydroxyl groups of organic and inorganic surfaces through condensation. The change in the surface polarity enables a better dispersion between the modified nanoparticles and polymer matrix [38-40].

2.2.5   Polyurethane

Polyurethane (PU) combines diisocyanates (such as methylene diisocyanates) with polyols through a chemical reaction [41, 42]. This results in a long-chain polymer that contains repeating urethane groups. The reaction can be customised to create different polyurethane materials with unique properties, making them useful across various industries [43, 44].
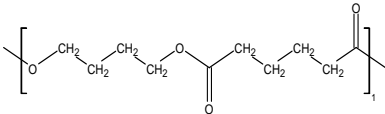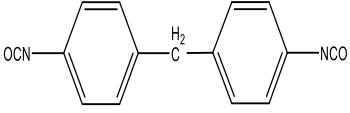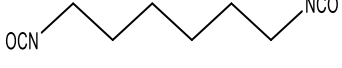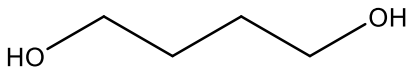
One exciting aspect of PU is its self-healing capability. Self-healing PU is a specific type that can repair minor damage or scratches autonomously. The self-healing of PU follows two different mechanisms, i.e., intrinsic, and extrinsic.

Intrinsic self-healing refers to the material's inherent ability to repair damage autonomously without external intervention or stimulus. This means that the healing process is an intrinsic property of the material itself and is triggered solely by the presence of damage. Intrinsic self-healing PU contains specific chemical or physical structures that facilitate healing.

In case of extrinsic self-healing PU, during fabrication, microcapsules containing a liquid healing agent are dispersed throughout the PU material. These microcapsules are tiny, typically ranging from a few micrometres to a few hundred micrometres in size [45]. When the self-healing PU sustains minor damage, such as small cracks or scratches, the microcapsules near the damaged area rupture due to the stress concentration. The ruptured microcapsules release the healing agent into the damaged region, where it comes into contact with the exposed surfaces. Once the healing agent comes into contact with the damaged surfaces, it reacts with the PU matrix, forming a new chemical bond. This reaction helps to "heal" or bridge the gaps in the material, restoring its integrity. The duration of the extrinsic self-healing process in PU can vary depending on several factors, including the specific formulation of the PU, the extent of damage, environmental conditions, and the presence of any catalysts or activators. In general, extrinsic self-healing mechanisms in PU can occur relatively quickly, often within minutes to hours after damage occurs. However, complete healing or restoration of mechanical properties may take longer, ranging from hours to days, especially for more severe damage.

It is important to note that these timeframes are approximate and can vary based on the specific conditions and materials involved [46, 47].

Table 2.1: Raw materials to synthesise the polyurethane.

Types	Component	Structure
Polyester polyol	Poly (1,4-butylene adipate	
Aromatic diisocyanate	Methylene diphenyl diisocyanate	
Aliphatic diisocyanate	Hexamethylene diisocyanate	
Chain extender	1,4-Butanediol	

The distinction between intrinsic and extrinsic self-healing is crucial because it affects the material's response to damage and the conditions required for healing. Intrinsic self-healing materials can repair themselves without any external intervention and are generally more desirable for applications where immediate or continuous recovery is needed. Extrinsic self-healing, while still beneficial, may require additional steps or equipment to trigger the healing process, making it more suitable for specific cases where such interventions are feasible or necessary.

Self-healing PU has the potential to extend the lifespan and improve the durability of various products, especially those subject to wear and tear or mechanical stresses. It has applications in coatings, adhesives, automotive components, and other areas where maintaining structural integrity is crucial. However, it is essential to note that the self-healing capability of PU might not be

effective for extensive or severe damage, as the healing agent in the microcapsules can only repair minor issues within its limitations. Further, PU, like many other self-healing materials, faces a trade-off between mechanical strength and self-healing capacity, which can result in compromised restoration of mechanical properties after damage occurs [19].

2.3 Response of a polymer dielectric to an electric field

Investigating the dielectric response of an insulator is crucial before utilising it in any application. The dielectric response refers to how the insulator reacts to an applied electric field and defines its electrical properties [48, 49].

The fundamental properties of dielectrics are crucial in understanding how they respond to an applied electric field. These properties include:

- Dielectric constant: It reflects the material's ability to polarise when subjected to an electric field.

- Dielectric breakdown strength indicates the material's capacity to withstand breakdown phenomena when exposed to high electric fields.

- Conductivity: This property signifies the material's ability to conduct electricity, involving the movement of non-localized charges.

- Dielectric loss Tangent: This parameter represents the relaxation phenomenon or energy conversion/loss within the material under an electric field.

Dielectrics find extensive applications in the electrical and electronic industries, performing various functions. For instance, they are used in capacitors for electrical energy storage and cables to insulate electrical components.

2.3.1   Electric conduction in polymeric insulating materials

The primary objective of electrical insulating materials is to prevent electrical conduction under all usage conditions. However, it is challenging to avoid low-level conduction, particularly at high electric fields. Nearly all insulators exhibit some conduction processes due to the presence of charge carriers, even if their quantity is minimal [49]. When subjected to sufficiently high electric fields, insulators may behave like semiconductors, causing conduction species such as electrons, holes, or ions (if present) to drift, resulting in current flow [35].

Insulating materials are wide band-gap materials featuring a substantial energy gap of several electron volts between the valence and conduction bands. Electrons must possess enough energy to overcome this gap to allow electrical conduction. The band theory is used to explain conduction in insulators [35], although applying it to complex insulating polymers often requires making certain assumptions that may not be entirely accurate. Electrical insulating materials must exhibit extremely low conductivity, ideally nearing zero. An ideal dielectric material to be used as an insulator in high voltage applications should have the following qualities:

- Ability to withstand high temperatures during service; Essential for maintaining insulation integrity and performance in high-temperature environments, preventing breakdown or degradation of the insulating material.

- High mechanical strength and stiffness; Crucial for withstanding mechanical stresses and loads experienced during installation, operation, and maintenance, ensuring long-term structural integrity and reliability.

- High resistivity; Important for minimizing leakage currents and preventing electrical breakdown, maintaining insulation effectiveness and safety in high-voltage applications.

- High dielectric strength and minimal dielectric loss; Critical for efficiently storing and transmitting electrical energy without significant loss, ensuring optimal electrical performance and energy efficiency.

- Water-resistant Properties; Vital for protecting the insulating material from moisture ingress, which can compromise dielectric properties, increase leakage currents, and accelerate degradation, particularly in outdoor or humid environments.

- Resistance to thermal and chemical degradation; Essential for maintaining insulation properties and performance over extended periods, even in harsh operating conditions involving exposure to elevated temperatures, chemicals, and environmental contaminants.

Failure to fulfil these requirements could lead to current flow and ageing processes, ultimately compromising the reliability of the insulation.

2.3.2 Aging degradation and breakdown

Ageing in electrical insulation refers to the irreversible changes in material properties caused by various factors in the service environment. These factors include thermal, electrical, environmental, and mechanical influences [50, 51]. Over time, the electrical insulation may no longer endure these ageing factors, leading to failure.

There are different types of ageing in polymers:

- Physical Aging: This occurs over time due to the structural relaxation of the polymer chain through segmental motion in the amorphous region. Variations in the glass transition temperature are critical in determining whether ageing will occur. Physical ageing in amorphous polymers can be associated with the inefficiency in molecular packing, which leaves some lattice sites unoccupied due to chain structure and steric hindrances [52, 53].

- Chemical Aging: Environmental events, such as exposure to UV light, heat, or outdoor weathering, can cause chemical ageing. This leads to chain scission and bond breakage, releasing electrons and ions. The resulting ionic conductivity can cause local joule heating at high electric fields, leading to current flow and thermal runaway. Moreover, other effects can also occur for example a reduction in the mechanical strength of the polymer leading to an increased probability of microcrack formation and the production of voids and other failure mechanisms [54].

- Mechanical: vibrations, tensions, bending stresses, and electrical effects may influence mechanical and thermal ageing. They can lead to physical and chemical changes in the insulation's structure, such as cracks, protrusions, delamination, voids, or poor adhesion to interfaces, particularly in cable construction. Physical ageing may be reversible through re-conditioning which involves applying controlled heat treatments to relax molecular chains and reduce internal stresses, thereby restoring flexibility and mechanical strength, while chemical ageing is irreversible due to morphological changes caused by chemical reactions.

Multiple ageing processes are interconnected, and the breakdown of solid dielectrics is a subject of intense research due to the uncertainties surrounding ageing and degradation [55, 56]. Experimental evidence suggests that the time to break down decreases with increasing electric field [57]. Deviations from Ohm's

law in conduction current and thermoelectrical ageing [58, 59] indicate that thermal and electrical effects can induce ageing, ultimately leading to a breakdown.

2.3.3   Breakdown processes of solid dielectrics

Research into the breakdown of gaseous, liquid, and solid dielectrics has developed several breakdown theories. In 1922, Wagner proposed an idea for solid dielectrics based on local joule heating leading to thermal breakdown. Early theories of solid breakdown [35, 49] include:

- Electronic breakdown: This involves the generation of free electrons by the ionization of gas molecules within the cavity or void inside the solid dielectric due to the application of high electric fields. These free electrons gain sufficient energy, rapidly increasing current flow, and cause breakdown.

- Electromechanical breakdown: In this process, mechanical stresses within the dielectric can initiate breakdown. High electric fields can induce mechanical deformations, causing the dielectric to crack or develop defects that facilitate breakdown.

- Thermal runaway occurs when the applied electric field causes localised heating in the dielectric, leading to a temperature increase. At a critical temperature, the material's properties can change, causing a decrease in its dielectric strength and ultimately resulting in a breakdown.

- Breakdown due to discharges: Discharges, such as PD or corona discharges, can occur within the void or cavity of a dielectric at high electric fields. These discharges can weaken the material and contribute to breakdown.

In practical scenarios, the breakdown processes often occur combined rather than individually upon voltage application. These processes can be classified into

29

short-time breakdowns and long-time breakdowns. These short-term breakdowns and long-term breakdowns of the insulation due to the discharges can be used to classify the insulation characteristics of the material. ASTM D149, IEC 60243 explain the standard procedures involved to characterise the insulation material at laboratory.

The short-time breakdown is used to determine the strength of a material. A continuous rising voltage is applied to the material between two electrodes at a constant rate or in steps within a short period. While long-time breakdown is employed to assess a material's lifetime and resistance to various applied voltages. It involves laboratory treeing tests, which study the formation of tree-like defects within the dielectric under prolonged voltage application.

Understanding these breakdown processes is vital for designing reliable electrical systems and selecting appropriate dielectric materials to ensure safe and efficient operation.

2.3.4 Breakdown due to Discharges

Discharges in insulating materials can occur either externally or internally during short-term or long-term testing. External discharges occur in the medium surrounding the test specimen, potentially leading to failure beyond the electrode edges. In contrast, internal discharges happen within the material, arising from defects such as voids or cavities. These internal discharges result in PDs, leading to the deposition of space charge and localised erosion known as "treeing," eventually leading to complete breakdown [60].

The long-term degradation and breakdown (treeing) in solid dielectrics are associated with PDs and space charge formation within the materials. Therefore, monitoring PDs [61-65] and studying electrical treeing [66] are essential tools for assessing the health of the material.

IEC standard 60270 defines PD as a localised electrical discharge that bridges the insulation. Such discharges may manifest during operation in the presence of voids, cuts, cracks, fillers, contaminants with poor adhesion to the insulation, or delamination at interfaces [61]. The inception of PD indicates ageing and degradation in solid insulating systems, particularly in electrical machines, such as generators. It can be detected in an external circuit as electrical current pulses associated with individual discharges in the material [67].

The occurrence of PD relies on the availability of free electrons in gas-filled cavities, which can originate from cosmic radiation or gas ionization within the voids [68]. Additionally, charge injection from electrodes under high electric fields can contribute to initiating PD [68]. Although these discharges are localised and have small magnitude, their cumulative impact can lead to progressive damage and eventual equipment failure [69].

Understanding and monitoring PD is vital for evaluating the health and reliability of electrical insulation systems. These processes play a significant role in predicting and preventing potential breakdowns and failures in power equipment.

2.4 PD Detection in Cable Insulation

For more than half a century, PD testing has been employed to assess the quality of electrical insulation and, at times, to identify signs of insulation deterioration in HV equipment. Electrical pulse detection from PD events has served as the primary non-destructive electrical test for cable insulation, particularly for extruded plastic cable insulations like PE, XLPE, Epoxy, and Ethylene Propylene Rubber (EPR). Since the late 1950s, extensive global research efforts have been dedicated to developing detectors for PD measurement. Typical instruments include those from Robinson (UK), Haefely and Tettex (Switzerland), Tur Mut (Germany), Hipotronics, and Biddle (USA), [70].

PDs give rise to a variety of physical effects, encompassing transfer of electrical charge, acoustic, optical phenomena, and chemical transformations. Furthermore, the transient alteration in electrical pulses generates electromagnetic waves. Consequently, the methods employed for detecting PDs can be categorized broadly based on electrical, acoustic, optical, and chemical principles.

2.4.1 Chemical Detection Technique

PD activity can cause chemical changes in the dielectric material, and these changes have been exploited for detection purposes. For instance, in Gas-Insulated Switchgear (GIS), PD activity can lead to the decomposition of SF_6 into specific chemical compounds, such as SOF_2 and SO_2F_2. Detecting these gaseous by-products confirms the presence of PD, as previously established by research [71, 72]. Similarly, PD activity in power transformers can be inferred by analysing

changes in the transformer oil through a technique called Dissolved Gas Analysis (DGA) [21, 73, 74].

Moreover, this technique can only be applied offline to detect discharging events inside cable insulation. This is because the method analyses the by-products produced during discharging, which are typically obtained externally. On the other hand, electrical discharges occur within microscopic voids or channels within the cable insulation material. The by-products generated during these discharges remain confined within the voids or cavities, making it difficult to extract the by-products generated by the PD events and analyse them using the chemical detection technique [75, 76]. Therefore, the chemical methods are yet to be widely adopted for precise PD detection despite the progress made thus far.

2.4.2 Thermography Technique

Thermography is a technique that utilises thermal imaging cameras to visualise the temperature distribution of objects or surfaces. In detecting discharging events in power cables, thermography becomes valuable because the temperature of the discharging sites is typically higher than the surrounding areas [77, 78].

For instance, PD in power cables, where localised electrical discharges occur within microscopic voids or channels in the insulation, thermography can identify areas with elevated temperatures due to the discharging activity. However, since the discharges in PD/electrical treeing are enclosed within the cavities, tubules, or channels, high-sensitivity thermal imaging cameras are required to detect and capture these subtle temperature differences [79-81].

Despite its advantages, thermography has limitations for certain types of discharging events. For example, thermography may not be as effective in the case of discharges occurring internally within the cable insulation. Additionally, thermography can be prone to external interference, especially in industrial environments where various heat sources or ambient temperature variations may affect the accuracy of thermal imaging measurements [82].

In short, while thermography is a valuable technique for detecting externally occurring discharging events, such as corona discharges that produce visible temperature differences, it can have limitations when it comes to detecting and analysing discharges that are enclosed or occurring internally within the insulation material.

2.4.3   Electrical Detection Techniques:

PD being a defective site in polymeric insulation, act as an energy source under the influence of electric stress. These discharging sites create electromagnetic pulses which propagate through the insulation matrix associated with electrical pulses on the conductors. PD electrical signals can have a frequency spectrum that extends beyond 1 GHz. However, it is important to note that higher-frequency PD signals experience more significant attenuation [83, 84]. In the manufacturing industry, the conventional electrical detection method is typically used to detect PD signals. This method has been employed for over five decades and operates within the frequency range of tens to hundreds of KHz. It is commonly used in various power apparatus, including power capacitors, transformers, electrical machines, circuit breakers, gas-insulated substations (GIS), cables, and cable accessories [85-88].

There are two main approaches to detect the electrical signal from the discharging sites in the laboratory.

- Current Transformer (CT) on Neutral
- Divider on HV terminal

CT on Neutral Approach: Much research has been done in past to detect the PD using high frequency current transformer (HFCT) in service as well as in laboratory [89-91]. In laboratory while analysing the PD, an artificial protrusion is created inside the polymeric insulation by injecting the needle and connecting this needle with a high-voltage terminal. The other side of the insulation is connected with the ground electrode, a HFCT is clamped to the grounding electrode to monitor the current flow to the ground and the output of HFCT is observed at the oscilloscope. This technique is very cheap, simple, and safe to use. Further, a spectrum analyser can be used, and trends can be established to characterise the discharges [92-94]. Apart from these advantages, the main fundamental challenge that needs to be addressed before using this technique is that it is prone to interference from external sources, and it is difficult to get a pure signal from discharging sites.

Divider on HV Terminal Approach: In this technique, a high voltage discharge free coupling capacitor is attached to the HV terminal while the sample is placed in parallel to this capacitor. Discharge pulses from the protrusion, needle tip, or electrical tree tip travel through the insulation and are detected for analysis. The individual pulse from the electrical tree can be calibrated by injecting a discharge-simulating pulse of known magnitude into the detector circuit. This technique is suitable for online condition monitoring if the sensors are pre-installed. Otherwise,

it requires the de-energization of the system to install the sensors. Further, it is difficult to avoid external interferences entirely; therefore, the received signal is complex and difficult to analyse.

2.4.4 **Electromagnetic Wave Detection:**

When discharge occurs inside the tubules and channels or voids/cavities inside the polymeric insulation, an electromagnetic wave is produced due to the discharging activity and propagate away from the discharging site. These waves can be detected and analysed to conclude events happening inside the polymeric insulation. There are two approaches to detecting the electromagnetic signal emitted by the discharging sites.

- Capacitive Probe
- Antenna Technique

The capacitive probe technique is limited in its applicability and is primarily suitable for detecting PD in metal-clad switchgear. Consequently, it is not well-suited for use in power cable applications. Conversely, the Antenna technique can detect the electromagnetic waves emitted during a PD event. These waves can be captured using various types of antennas, facilitating the characterization and quantification of the noise generated by the discharging sites. Utilizing specially designed antennas connected to a high-bandwidth oscilloscope, it becomes possible to identify the presence of discharges and correlate the shapes of the detected pulses with specific types of discharges.

The technique enables an estimate of the discharge magnitudes in pico coulombs (pC), which is achieved through an indirect laboratory calibration of the antennas.

This method is commonly used for detecting PD in rotating machines and air-cooled transformers. Still, it has also gained attention for detecting discharges in HV insulators to monitor the equipment's condition online.

2.4.5   Optical Methods:

The use of optical methods for partial discharge detection in power apparatus is rare. This is mainly due to their limited detection sensitivity. While there have been occasional attempts to explore this approach, including measuring discharge optical signals in GIS through the use of a photo-multiplier tube and photon-counting technique [95, 96], optical methods have not seen widespread adoption in the realm of partial discharge detection.

2.5 Acoustic Emission Technique:

When a partial discharge event occurs, it is accompanied by a rapid release of energy, with a portion of this energy being emitted as an acoustic pulse. The utilization of acoustic transducers for partial discharge detection offers several advantages. The equipment required is compact, eliminating the need for additional HV capacitors. Furthermore, it does not necessitate the disconnection of the power supply, making it suitable for online monitoring.

Acoustic sensors can be categorized into two types: accelerometers that operate in the audio range (below 20 kHz) and AE sensors that operate in the ultrasonic range (above 20 kHz). Accelerometers have primarily been used for detecting discharges in circuit breakers [97-99]. In contrast, AE sensors have found widespread application in various power apparatus, including power transformers

[100-103], GISs [71, 104], generators [105], capacitors [106], as well as cables and cable accessories.

The AE technique has been well-established for detecting discharges inside liquid insulation systems, such as transformer oil [101, 107]. Additionally, being a non-intrusive and non-destructive technique, making it ideal for predictive or preventive condition-based maintenance of power systems without interrupting power supply continuity. Despite its merits, some fundamental challenges need to be addressed when applying the AE technique to power cables:

a) Different layers of insulation materials in power cables cause the attenuation of acoustic waves, resulting in a smaller magnitude of the received wave. This requires more sensitive and specifically designed sensors for accurate signal detection.

b) In the case of electrical treeing, unlike PD, discharges occur at different locations along the branches of the electrical tree. The acoustic signals from these discharges can superimpose each other during propagation through the insulation, making it difficult to draw definitive conclusions about what is happening inside the cable [108].

c) In long transmission cables, the most viable solution is to mount acoustic sensors at cable joints. However, the distance between the joints leads to damping of the AE signal as it propagates through the insulation matrix, making it challenging to detect the signal using ordinary sensors.

d) Elevated cable temperature may also affect the sensitivity of the AE technique, requiring careful consideration and compensation for temperature effects during analysis.

The research related to the AE technique explores various aspects, such as the generation of acoustic signals from cavity-type defects, phenomena of acoustic wave propagation, factors affecting the propagation of acoustic waves, and detecting sensors, along with their advantages and disadvantages. Researchers continue to explore these factors to enhance the effectiveness of the AE technique for detecting discharging events within power cables [109].

2.5.1   Initiation of Acoustic signal:

The electric stress causes localised discharges inside the void or cavity present in the insulation matrix. These discharging events inside the cavity behave like source of energy. The energy associated with the discharge event is transferred to the gas molecules causing increases in temperature, pressure, and generating short-duration pulses [26, 110, 111]. Furthermore, when a PD event occurs within the insulation material of a high-voltage component, it generates localized heat and pressure within the insulation. This sudden increase in temperature and pressure causes mechanical stress on the surrounding material, particularly on the walls of the cavity or void where the discharge occurs. As the insulation material undergoes mechanical deformation due to this stress, it releases elastic energy in the form of waves propagating through the material. These elastic waves travel through the material at the speed of sound and propagate away from the site of the PD event [111-113].

2.5.2   Propagation of Acoustic Signal:

The elastic waves initiated due to the discharge event travel in both axial and radial directions of the discharge in insulation, as shown in Figure 2.2.
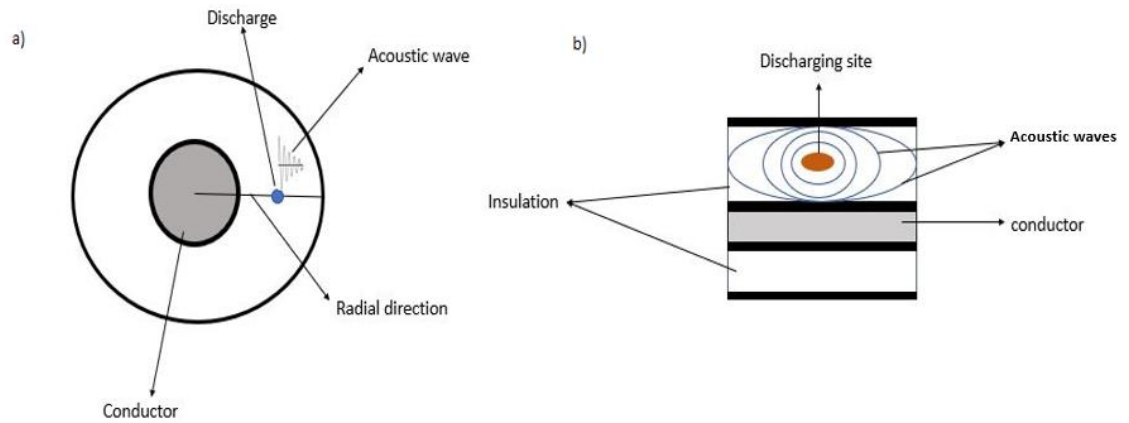
Figure 2.2: propagation of the elastic wave, a) radial direction, b) Axial direction.

In the radial direction, these acoustic waves travel toward the semiconducting layers of the insulation and the conductor. At the interface between the insulation and the semiconducting layer, some of the elastic wave energy is reflected in the insulation. In contrast, the remaining power is transmitted into the semiconducting layer. The specific behaviour of reflection and refraction at the interface depends on the acoustic impedance of the materials involved [114, 115].

The discharges produce sound waves that move within the insulation as longitudinal waves. These sound waves create variations in pressure (P) measured in Pascal and displace the molecules within the insulation. The propagation of these waves can be described using an equation that accounts for spherically symmetric pressure fields [116].

$$\nabla^2 P = \frac{1}{c^2} \frac{\partial^2 P}{\partial t^2} \qquad (2.1)$$

Here P represent the pressure of the propagating sound wave while c represent the speed of sound in air.

2.5.3 Factors Affecting the Propagation of Acoustic Wave:

The pressure pulse and elastic waves originating from the discharging sites propagate in longitudinal and transverse patterns, spanning the cable insulation's radial and axial directions. The complexity arises due to the diverse nature of the medium, involving multiple layers within the cable structure. The insulation matrix acts as a damping agent during wave propagation, contributing to the attenuation of waves [117].

The waves propagating along the axial direction of the discharge need to travel a longer distance before being detected, leading to increased damping. Furthermore, numerous discharging sites in defective zone generate transverse and longitudinal waves with varying magnitudes, depending on the intensity of the discharges. Consequently, the insulation matrix contains multiple waves of different magnitudes and directions, creating a complex model for analysis.

The interaction of acoustic waves emitted during PD events leads to a phenomenon known as superposition. When these waves propagate through the insulation material, they may encounter various interfaces, defects, or heterogeneities within the material. As a result, the waves undergo reflection, refraction, and scattering, which can cause them to interfere with each other.

Superposition occurs when multiple waves overlap in space and time, resulting in the addition or cancellation of wave amplitudes. Constructive interference occurs when waves align in phase, leading to an increase in the overall wave amplitude. In contrast, destructive interference occurs when waves are out of phase, resulting in a reduction or cancellation of the overall wave amplitude. Understanding the complexities of wave propagation and the effects of superposition are crucial for interpreting the signals detected during PD monitoring.

2.5.4   Acoustic Damping in Polymers:

Acoustic waves encompass all types of mechanical waves in polymers. Due to the viscoelastic nature of polymers, they serve as energy-absorption and vibration-damping materials [118]. However, the attenuation of acoustic signals while propagating through cable insulation poses challenges in detecting these signals. A more sophisticated sensor design is necessary to detect low-magnitude signals. However, this may expose the highly sensitive sensor to external noise, making it difficult to extract the specific discharge signal.

Mounting acoustic sensors at the cable joints, which are typically far apart, is the easiest and cheapest approach to detect PD. However, if a discharge event occurs near the midpoint between two joints, the discharge signal has to travel a considerable distance before being detected and analysed. This situation presents a challenge in determining whether the discharge signal is detectable. Finding practical solutions to address these complexities remains an ongoing endeavour. Hence, this research is centred around investigating the propagation characteristics specifically damping of acoustic pulses emitted during a discharge event and

assessing the feasibility of employing AE detection techniques for the detection of PD in cable insulation.

2.5.5   Acoustic Attenuation:

As mentioned earlier, the intensity of acoustic signals decreases as they travel over a distance. This phenomenon is known as acoustic attenuation and occurs due to various mechanisms in polymers, such as scattering, absorption, refraction, reflection at the interface of polymer and semiconducting material, and dispersion.

Reflection and refraction of acoustic waves at the interface between the polymer and semiconducting material cause a reduction in signal magnitude. However, these events alone do not provide conclusive information about the damping capacity of the insulating medium. On the other hand, absorption and scattering phenomena play significant roles in understanding acoustic attenuation and will be further explored in this research.

2.5.6   Energy Absorption

The propagation of acoustic waves within the polymer induces the elastic motion of particles, resulting in energy dissipation in the form of heat. Additionally, various phenomena like relaxation and heat flow, and material properties like viscosity, contribute to energy dissipation in the polymeric medium [119].

Relaxation occurs as polymer chains undergo structural reorganization in response to mechanical or thermal stress. This process involves the movement of polymer segments, such as chain rotation or segmental motion, to achieve a lower-energy state. Different relaxation mechanisms, such as glass transition relaxation

in amorphous polymers or crystalline relaxation in crystalline polymers, contribute to the overall dissipation of mechanical energy.

Viscosity plays a crucial role in determining the material's response to mechanical forces and its ability to dissipate energy. When subjected to shear stress, polymer molecules experience resistance to flow due to internal friction between polymer chains. Higher viscosity results in greater resistance to flow and higher energy dissipation in the form of heat during wave propagation.

Heat flow within the polymer medium refers to the transfer of thermal energy induced by the mechanical motion of polymer particles during acoustic wave propagation. Mechanical energy is converted into thermal energy, leading to an increase in temperature within the polymer. Additionally, external heating or environmental temperature fluctuations can contribute to heat generation and dissipation within the polymer, influencing the overall energy dissipation behaviour of the material. Therefore, energy absorption within the polymer is crucial in determining the degree of acoustic attenuation.

Energy absorption in the polymer is comparable to vibration damping in solid materials. When a discharge occurs within the tubules and channels of an electrical tree, mechanical waves are generated, causing the polymer matrix to experience elastic loading. Subsequent unloading of the polymer from this elastic stress results in energy dissipation, known as energy absorption [120]. Chapter 9 of the study thoroughly analyses the energy dissipation as acoustic pulses from a discharge propagate through the polymer.

2.5.7 Acoustic Scattering:

The presence of inhomogeneities within the polymer matrix, such as voids, inclusions, crystal discontinuities, particles, and grain boundaries, leads to the reflection or refraction of acoustic waves, resulting in the attenuation of the AE signal. Coherent and collimated waves transform into incoherent and divergent waves due to refraction and reflection phenomena. The effects of scattering on the shape and magnitude of the propagating acoustic pulse are modelled in this study using MATLAB. The modelling process is thoroughly described in Chapter 3, where the methodology and techniques employed to simulate acoustic wave propagation are explained. On the other hand, Chapter 4 presents the results and analysis obtained from the MATLAB model, focusing specifically on the effects of reflections on the propagating acoustic impulse.

2.5.8 Detection of Acoustic Signal:

Discharging sites within the tubules and channels of an electrical tree emit sound waves in both ultrasonic and audible frequency ranges. These waves can be detected using various acoustic sensors, selected based on their sensitivity and the intensity of the acoustic signals [121]. The AE detection techniques are non-invasive, with small test equipment suitable for online condition monitoring and free from electrical interference. By using multiple sensors and analysing the detected signals through methods like time of arrival (TOA) or time difference of arrival (TDOA), it becomes possible to estimate the location of the fault.

2.6 Summary

Polymeric insulations offer remarkable properties, which make them highly effective in various HV applications. However, certain surface irregularities or protrusions on the polymer from mechanical stress or manufacturing defects can cause discharge initiation and insulation breakdown. A possible solution to this challenge is incorporating PU in the insulation. PU has a unique ability to self-repair any defective sites in the polymer structure, thus reducing discharge initiation and improving the reliability and performance of electrical systems.

Moreover, this chapter thoroughly explained the various detection techniques to identify discharges at their initial stages, explicitly focusing on acoustic detection. AE technique emerged as a promising method due to its non-invasiveness, suitability for online condition monitoring, and immunity to electrical interference. Further, the phenomena of initiation of sound waves in both ultrasonic and audible frequency ranges from the discharge is also explained.

While AE detection shows great promise, this chapter discussed its associated challenges. One significant challenge is the attenuation of acoustic signals as they propagate through the polymer insulation. Factors like scattering, absorption, and reflection contribute to energy dissipation and, consequently, the reduction in acoustic signal magnitude. Additionally, the complex behaviour of waves inside the insulation poses difficulties in accurately estimating the impact of scattering on AE signals.

Despite these challenges, this chapter also highlights the advantages of AE detection, such as its potential for precise fault location estimation when using

multiple sensors and applying time-based analysis methods. Furthermore, AE detection techniques offer a non-intrusive approach to condition monitoring, making them suitable for online monitoring of electrical systems.

The subsequent chapters will focus on the properties and benefits of using polyurethane as an insulation material and investigate the acoustic detection techniques, addressing the challenges and exploring potential improvements to enhance the effectiveness of acoustic detection in detecting and locating the discharges and ensuring the integrity of electrical systems.

Chapter 3

Analytical Modelling and Simulation of Acoustic Pulse Propagation

3.1 Introduction

A discharge event inside a cavity releases energy, puts mechanical pressure on the cavity walls, and generates an elastic wave surrounding the cavity. The detection and localisation of these PD events through short-duration acoustic pulses have proven to be a powerful technique, particularly in gas-insulated systems (GIS) and transformer oil [111, 122]. Nevertheless, its full potential remains untapped in solid insulation systems.

Numerous models have emerged to detect AE signals from PD events in various media [102, 123]. However, the intricate effects of acoustic scattering and reflections on the propagating acoustic pulse have yet to be adequately addressed. This becomes crucial when applying this technique to transformer oil insulation, characterised by substantial reflections and scattering, or underground power cables with solid polymeric insulation, where the polymer morphology can cause acoustic reflections and scattering.

The consequences of overlooking the impact of acoustic scattering and reflections are profound, potentially leading to misleading interpretations of acoustic signals and inaccurate information about PD events. This chapter presents a modelling technique designed using MATLAB and COMSOL Multiphysics to

bridge this gap and shed light on the underlying complexities. The approach analyses the scattering, reflections, and propagation characteristics of acoustic pulses emitted from discharge events in solid insulating materials. However, the approach can be useful in addressing the effects of reflections and scattering on the propagating acoustic pulse in other media.

This chapter explain the detailed modelling process of acoustic pulse propagation using COMSOL Multiphysics, effects of boundary conditions on the shape, magnitude, and propagation velocity of the propagating acoustic pulse, including quantifying reflections' effects on the propagating acoustic pulse using MATLAB. These modelling techniques will provide an understanding of acoustic pulse behaviour and the significance of boundary conditions, ultimately paving the way for enhanced accuracy and interpretations in acoustic pulse propagation studies.

3.2 Model Development

Initial modelling was performed using a cylindrical geometry in COMSOL. The shape of the pulse was observed to change as it propagated through the cylinder. A simple MATLAB model was then developed to determine if the changes observed were because of reflections at the boundary between the polymer cylinder and the air surrounding the cylinder.

The output of this model was similar to that observed in COMSOL to confirm that the pulse was propagating correctly in the COMSOL simulation. Further, a spherical model was developed which reduced the impact of reflections as the boundary between the polymer and air was always perpendicular to the direction

of wave travel. The spherical geometry also allowed analytical verification of the COMSOL model.

This model confirmed that the simulation was performed correctly and was then used to test the addition of a perfectly matched layer that was intended to be used to eliminate reflections in the cylindrical model. Once the perfectly matched layer had been demonstrated in the spherical model the final design of cylindrical model incorporating a perfectly matched layer was developed.

This chapter provides details of these models. And the results will be discussed in chapter 5.

3.3 Analytical Modelling of Pressure

The electric stress causes localised discharges inside the cavity. These discharge events inside the cavity behave like a source of energy, leading to the excitation of molecules in the cavity. Additionally, this energy emitted from the PD event exerts mechanical stress on the cavity walls, emitting elastic waves across a wide frequency range, spanning kilohertz [124] The electrostatic energy stored in the cavity because of the field distribution prior to breakdown can be determined analytically. If it is assumed that all this energy is converted into a pressure pulse, it is possible to estimate the value of the pressure pulse associated with the PD event. Consequently, this calculation estimates the pressure pulse initiated by the PD event.

A simulation model was developed in the electrostatic module of COMSOL Multiphysics to predict the electric field inside the spherical cavity for a 33kV high

voltage cable topology, as shown in Figure 3.1. The geometric parameters considered in the geometry are shown in Table 3.1.
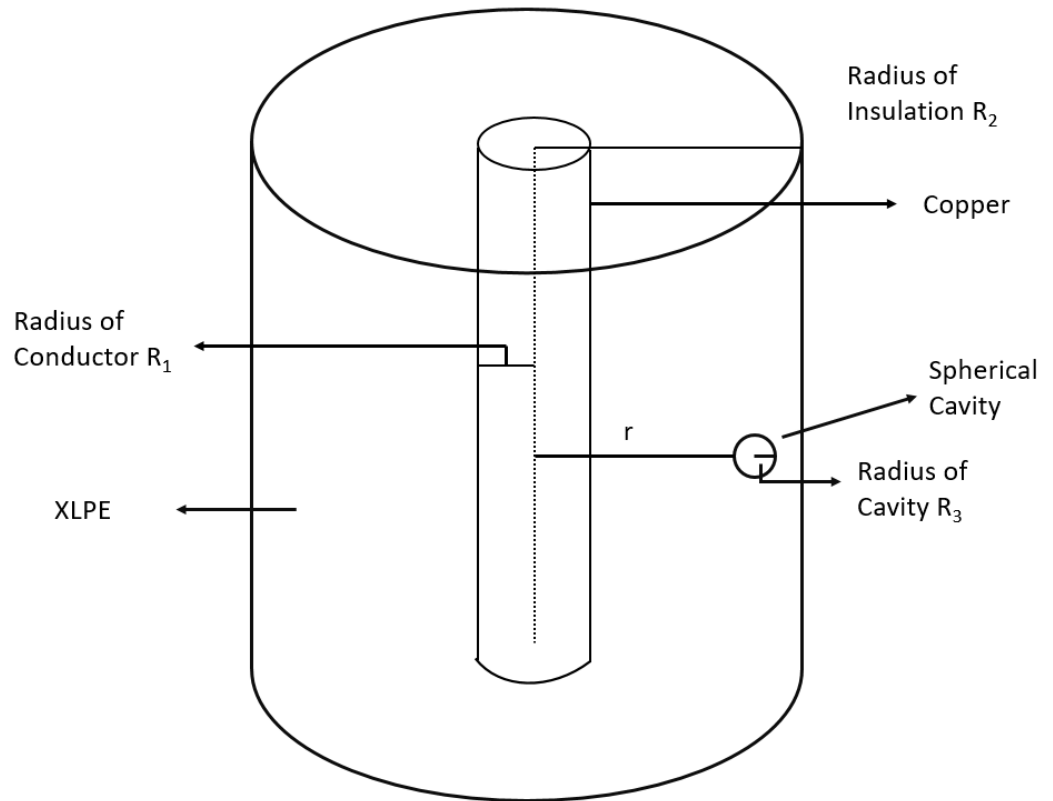
Figure 3.1: Geometric model of coaxial cable.

Table 3.1: Geometric parameters

Parameter	Value	Description
R_1	7.5mm	Radius of conductor
R_2	15mm	Radius of insulation
R_3	1mm	Radius of cavity
r	13mm	Location of the cavity from the central axis

The electric field across the air-filled cavity may not be uniform. It may be higher around the surface facing the conductor and lower at the cavity's surface opposite the conductor. However, the diameter of the cavity is much smaller than

the diameter of the insulation, the percentage change in the electric field across the cavity will be very small. Hence, it was assumed that the electric field across the cavity is uniform. The electric field inside the cavity was obtained from the above described COMSOL Multiphysics model. Further, the electrostatic energy stored in the cavity can be calculated by volume integration of the cavity using the equation,

$$w_e = \frac{1}{2} \int \varepsilon_o E^2 dv \qquad (3.1)$$

Here, ε_o is permittivity of the free space while E represent the electric field. For a cavity of radius R_3, the expression dv can be represented as,

$$dv = 4\pi R_3^2 dr \qquad (3.2)$$

Further, assuming that the electrostatic energy stored in the cavity is converted into a pressure wave and this pressure wave propagate through the insulation material. Additionally, the amount of pressure developed by this electrostatic energy can be calculated using the relation [125];

$$p = \frac{W_e}{Vol} = \frac{\frac{1}{2}\varepsilon_o E^2 \frac{4}{3}\pi R_3^3}{\frac{4}{3}\pi R_3^3} = \frac{1}{2}\varepsilon_o E^2 \qquad (3.3)$$

Here Vol, is the volume of the cavity. The magnitude of the pressure wave initiated as a result of the PD event can be calculated using the equation 3.3. The magnitude of the pressure wave calculated analytically was used to define the peak value of the acoustic pulse at the source to analyse the propagation characteristics of AE in COMSOL Multiphysics.

3.4 Modelling Acoustic Pulse Propagation in COMSOL Multiphysics

3.4.1 Field Model Equations

A three-dimensional (3D) COMSOL Multiphysics model was developed using partial differential equations to analyse the propagation characteristics of the acoustic pulse. Moreover, the mathematical module was chosen from the application mode of COMSOL Multiphysics, as this module provides the flexibility to specify customised mathematical equations, allowing for the precise definition of conditions governing the propagation of the acoustic pulse. The coefficient form of the partial differential equation 3.4 was selected from the mathematical mode of COMSOL Multiphysics to analyse the propagation of the acoustic pulse.

$$\left\{ \begin{array}{c} e_a \frac{\partial^2 P}{\partial t^2} + d_a \frac{\partial P}{\partial t} + \nabla.(-c\nabla P - \alpha P + \gamma) + \beta.\nabla P + \alpha P = f \\ \nabla = \left[\frac{\partial}{\partial x}, \frac{\partial}{\partial y}, \frac{\partial}{\partial z}\right] \end{array} \right\} \quad (3.4)$$

Further, the wave equation governing the propagation characteristics of an acoustic wave can be represented as:

$$\frac{1}{\rho C_s{}^2} \frac{\partial^2 P}{\partial t^2} - \nabla.\left(\frac{1}{\rho} \nabla P\right) = S(x, t) \quad (3.5)$$

Here, ρ is the density of the material in kg/m^3, $P(x, t)$ is the pressure in Pa, the term C_s represents the speed of sound in the medium under consideration, and $S(x, t)$ represents the acoustic source. Equation 3.4 was modified by changing the parameters and variables to get the PDE of acoustic wave propagation.

$$e_a = \frac{1}{\rho C_s{}^2}, \qquad c = \frac{1}{\rho}, \qquad d_a = \alpha = \beta = \gamma = 0, \qquad f = S(x,t)$$

Moreover, the discharge activity was assumed to act as a point source emitting acoustic waves. Considering the discharge activity as a point source implies that the acoustic waves propagate uniformly in all directions from a single localized source. While this assumption facilitates mathematical modelling and simplifies the interpretation of experimental data, it may not accurately reflect the spatial distribution of discharge events within the insulation material. PD events may occur at multiple locations and exhibit spatial variability in intensity, frequency, and waveform characteristics. However, the assumption of a point source remains a commonly used simplification in PD diagnostics due to its computational tractability and practical utility. This point source in the FEA model can be described as:

$$S(x,t) = \frac{dg(t)}{dt} \frac{\partial^2}{\partial x^2} (x - Xo) \qquad (3.6)$$

Here, $g(t)$ is the Gaussian pulse which can be described as:

$$g(t) = \begin{cases} Ae^{\frac{-\pi^2}{\tau^2}(t-\tau)} & for\ 0 < t < 2\tau \\ 0 & otherwise \end{cases} \qquad (3.7)$$

This above equation is obtained from the acoustic model of the Gaussian pulse point source [126]. Here, τ represents the pulse width. The notation A represents the volumetric flow rate away from the acoustic source in m³/s. The volumetric flow rate value defines the peak value of the acoustic pressure.

3.4.2   Model Geometry and Parameters

Two distinct model geometries were developed in COMSOL Multiphysics to analyse acoustic pulse propagation: spherical and cylindrical geometry. The cable's structure closely resembles a cylinder, making the cylindrical model a more suitable representation for studying the acoustic pulse propagation characteristics in underground power cables. However, the cylindrical geometry presented challenges due to its thickness being smaller than its length, resulting in complex reflections from the radial boundary. To tackle this complexity, an initial approach using a spherical model geometry was adopted, with the acoustic source placed at the sphere's centre. This configuration facilitated homogeneous reflections from all boundaries, shedding light on their effects on the propagating acoustic pulse. The sphere having a radius of 50 cm was developed, and the point source was positioned at its centre, as depicted in Figure 3.2.

Similarly, a cylinder measuring 100 cm in length and 10 cm in radius was created, with the point source located 50 cm along the axial direction. The point source simulated the acoustic wave initiated by a partial discharge event, employing the PD acoustic source model developed in Section 3.3. The acoustic pressure was determined at various points within the geometry using a point probe throughout the analysis. Furthermore, Table 3.2 represents the parameters used during the simulation while Table 3.3 outlines the materials considered during the study and their respective characteristics.
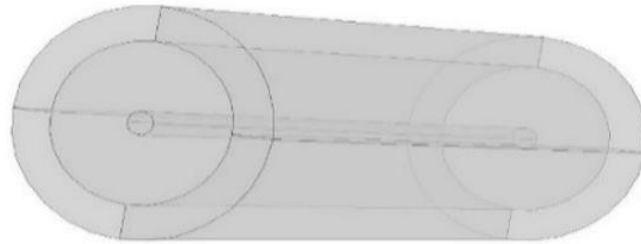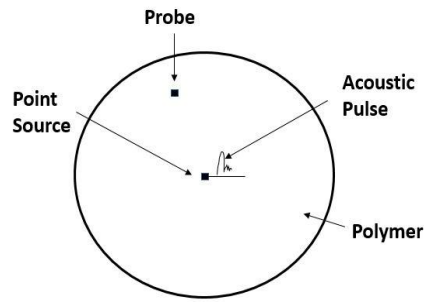
Figure 3.2: Spherical and cylindrical model geometries implemented in COMSOL.

Table 3.2: Materials used in COMSOL modelling to characterise the acoustic pulse propagation.

Material	Speed of sound	Density
Polyethylene	1100[m/s]	940[kg/m^3]
XLPE	1240[m/s]	930[kg/m^3]
Air	343[m/s]	1.225[kg/m^3]

Table 3.3: Parameters associated with COMSOL Modelling

Name	Expression	Description
f	100[kHz]	Pulse bandwidth
λ_o	$v_{polymer} * \tau$	Wavelength, free space
T	1/f	Period
$\rho_{polymer}$	$[kg/m^3]$	The density of the Polymer considered
$v_{polymer}$	[m/s]	The speed of sound in polymer considered
N	6	No elements per wavelength
t	1e-6	time
v_{air}	343[m/s]	Speed of sound in air
τ	1/f	Pulse width
A	135	Rate of mass flow
$D_{polymer}$	$1/(\rho_{polymer} \, v_{air}^2)$	Coefficient of e_a
$v_{polymer}$	$1/\rho_{polymer}$	The coefficient of the Polymer considered
Z	$\rho_{polymer} \cdot v_{polymer}$	Impedance
h_{max}	$v_{polymer}$ /f.N	Maximum element size

3.4.3   Meshing

The polymer domain was meshed using tetrahedral-shaped elements of quadratic Lagrange order divided into three sets. To accurately resolve the propagation of acoustic pulses, a minimum of 5 to 6 mesh elements per wavelength is required when using quadratic Lagrange elements. The maximum mesh size was determined by considering the computational resources available and the necessary level of accuracy, and this was calculated analytically using the below equation [123]:

$$h_{max} = \frac{\lambda_{min}}{N} = \frac{v_{min}}{f * N} \qquad (3.8)$$

Where h_{max} is the maximum mesh element size, λ_{min} is the minimum wavelength calculated at maximum frequency and minimum speed of sound v_{min} in the polymer region, and N is the number of elements per wavelength.

3.4.4   Study and Solver

The model is computed for a time-dependent study of 1000μs using the MUMPS (Multifrontal massively parallel sparse) direct solver [123]. This duration corresponds to the time taken for an acoustic pulse to travel from the source to the geometry's boundary, undergo reflection, and return to the source. Further, to adequately resolve the propagation of acoustic waves in the time, a minimum value of time step $\triangle$t is calculated by:

$$\triangle t = \frac{h_{max} \, CFL}{v_{min}} \qquad (3.9)$$

CFL is a non-dimensional number; it can be interpreted as the fraction of an element the wave travels in a single time step. To minimise the error, the value of the CFL number 0.15 was used for quadratic mesh elements [123].

3.5   Quantifying Effects of Reflection using MATLAB

3.5.1   Initiation of Pulse:

The MATLAB program explained below defines and examines the propagation of an acoustic pulse within the rod. The pulse generation is based on a trapezoidal waveform, with time measured in microseconds. The parameters used in the program are as follows: "start" denotes the point in time when the pulse first

becomes non-zero, "width" specifies the duration during which the pulse remains non-zero, and "ramp" represents the time taken for the pulse to rise to its maximum value and then fall back to zero. Through this MATLAB code, the characteristics of the acoustic pulse can be precisely controlled, allowing for a detailed study of its behaviour as it travels through the rod. The MATLAB code attached in appendix 1 was utilised to start the pulse.

3.4.2   Geometry and Parameters

A MATLAB model was developed to analyse the effects of reflections on the propagating acoustic pulse in a rod. It was assumed that:

- The rod is infinite in length with no reflections occurring at the end of the rod,

- The point of observation is assumed to lie on the axis of the rod,

- The material is linear and lossless,

- The pulses represent pressure,

- The base unit for time is the microsecond,

- The propagation velocity is constant.

Figure 3.3 shows a set of 4 possible paths for pressure pulse to travel between the source 'S' and point of observation 'P'.
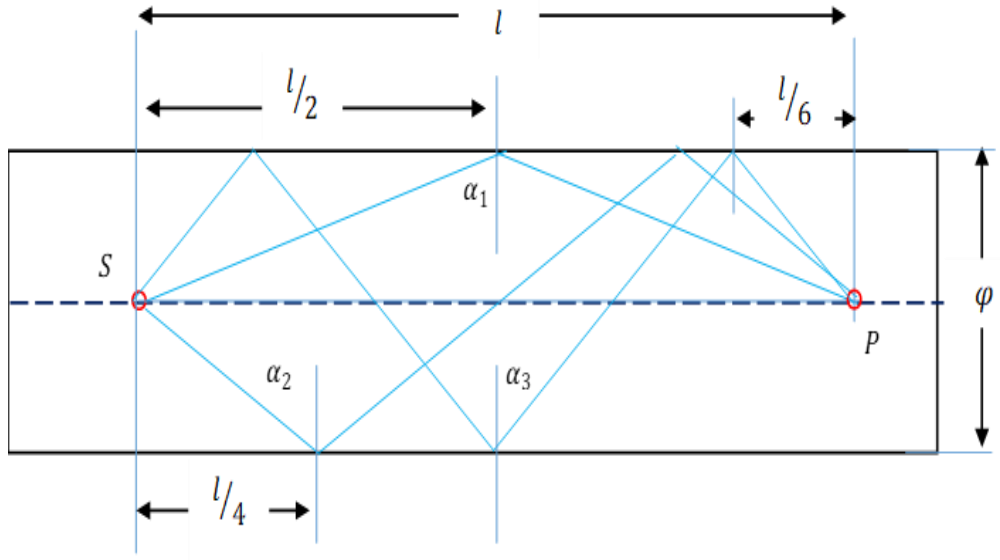
Figure 3.3: Visualization of our Potential Paths for Pressure Pulse Propagation in the Cylinder.

The cumulative effect of reflections from the four possible paths for the pressure pulse propagating through cylinder can be modelled analytically. Assuming that the length of a path with n reflections expressed as:

$$d_n = l\sqrt{1 + n^2 (\tfrac{\varphi}{l})^2} \qquad (3.10)$$

The path length 'l' was defined for no reflection and the remaining path lengths were calculated using the equation 3.10. Further, the sin of the angle α_n associated with the path with n reflections can be represented as:

$$\sin \alpha_n = \frac{d_o}{d_n} = \frac{1}{\sqrt{1 + n^2(\tfrac{\varphi}{l})^2}} \qquad (3.11)$$

To estimate the pressure after 'n' reflections, it was assumed that a pressure wave defined by the function $\zeta(t)$, propagates along each path and the pressure wave normal to the cross-section of the rod associated with a path with n reflections is given by:

61

$$P_n = sin_n\zeta\left(t - \frac{1}{u_p}\sqrt{1 + n^2\left(\tfrac{\varphi}{l}\right)^2}\right) = \frac{d_o}{d_n}\zeta\left(t - \frac{1}{u_p}\sqrt{1 + n^2\left(\tfrac{\varphi}{l}\right)^2}\right) =$$

$$\frac{1}{\sqrt{1+n^2\left(\tfrac{\varphi}{l}\right)^2}}\zeta\left(t - \frac{1}{u_p}\sqrt{1 + n^2\left(\tfrac{\varphi}{l}\right)^2}\right) \qquad (3.12)$$

If a reflection coefficient Γ is considered the expression will become:

$$P_n = \Gamma^n\frac{d_o}{d_n}\zeta\left(t - \frac{1}{u_p}\sqrt{1 + n^2\left(\tfrac{\varphi}{l}\right)^2}\right) = \Gamma^n\frac{1}{\sqrt{1+n^2\left(\tfrac{\varphi}{l}\right)^2}}\zeta\left(t - \frac{1}{u_p}\sqrt{1 + n^2\left(\tfrac{\varphi}{l}\right)^2}\right)$$

$$(3.13)$$

3.5.2 Pulse Set up:

A trapezoidal pulse was considered due to its easily modifiable nature and predictable characteristics. Featuring linear transition regions, well-defined rise and fall times, and simplicity in processing, and it was defined by two parameters.

i)   The pulse is non-zero, and pulse width indicates the time in microseconds,

ii)   The pulse ramp is defined as the time taken for the pulse to transition between zero and one, representing the maximum amplitude of the pulse.

The observation point 'P' away from the source was used to measure the pressure, and the distance was measured in meters. Further, the propagation speed was defined in m/µs, and the diameter of the rod was defined in meters. Moreover, the simulation period was defined in microseconds, and the path index was defined to observe the reflections. Further, an array was initiated to store the temporal behaviour of the pulse on each path. The temporal behaviour for all pulses was calculated at the point of observation. The sum of individual temporal behaviours over all possible paths was analysed, and the output was plotted in MATLAB.

3.5.3   General parameters in the model

The MATLAB model utilised for testing pulse propagation in the geometry illustrated in Figure 3.3 incorporates various general parameters detailed in Table 3.4.

Table 3.4: Parameters associated with pulse setup in MATLAB Model.

Parameters	Values	Units
Propagation velocity	0.001	m/µs
Rod Diameters	0.01	m
Observation point	10	m
Time step	0.05	s
gamma	0.95	

3.5.4   Pathlength calculation

The MATLAB code attached in appendix 1 calculates the path lengths for each propagation path, considering the distance between the source and the observation point along the axis of the rod. It also computes the normalization factors for each path. The propagation time for each path were computed based on the path lengths and pulse propagation velocity.

The time vector used for simulation is generated by starting from a specified start time and extending up to the simulation duration using a given time step. This process ensures that the time vector includes all the necessary time points within the simulation duration, allowing for accurate and precise data collection during the simulation process.

The pulse propagation for each path and time step was calculated. At each time step, it computes the pulse value by applying the pulse function defined in the code. Through an iterative process across each path and time step, the code effectively simulates the pulse's behaviour and changes as it travels through the medium, considering both reflections and attenuation effects.

To obtain the total output representing the cumulative effect of all individual propagation paths, the code sums up the results of each path. The cumulative impact is stored in the variable "output (noPaths + 1, :)," where "noPaths" represents the total number of propagation paths considered in the simulation.

By summing the results of each path at each time step, the code calculates the overall response, considering the combined contributions from all the propagation paths. This final output represents the pulse's behaviour and interaction with the medium, considering all relevant propagation paths and their respective effects.

After calculating the cumulative effect of all individual propagation paths, the code plots this cumulative result against time. The plot visualizes how the pulse evolves, considering the combined contributions from all the propagation paths.

Additionally, the code displays the initial path's maximum value, corresponding to "output (1, :)". This maximum value represents the peak amplitude of the initial pulse at the source location. Displaying this maximum value provides valuable information about the initial pulse's strength and intensity, allowing a better understanding of its behaviour as it propagates through the medium and interacts with various paths.

Overall, this model offers valuable insights into the pulse propagation phenomenon under consideration, showcasing both the cumulative effect and the initial pulse's maximum intensity.

3.6 Perfect Matched Layer

The Perfect Matched Layer (PML) is a common technique for absorbing outgoing waves in numerical wave propagation simulations. In COMSOL, the PML can be built for a spherical geometry by defining an absorbing layer surrounding the spherical region of interest. The layer absorbs the propagating waves before reaching the numerical boundaries of the simulation, reducing the reflections. The absorption properties can be adjusted by specifying the width of the PML [127-129]. Therefore, to mitigate the effects of reflections on the propagating acoustic pulse in the above model, a PML was used in COMSOL Multiphysics. The PML needs an adequate setting of the layers or geometric thickness to work as an absorbing boundary for the propagating acoustic pulse [130].

3.6.1   Model geometry:

Adding the PML is challenging in time domain analysis, especially for small geometries. As PML does not include a real stretching component to eliminate any reflections from the boundary and acoustic scattering, the choice of geometric thickness is critical [131, 132]. For cylindrical geometry where, radial thickness is less compared to the length of the cylinder, setting up the adequate geometric thickness becomes complex. Therefore, primarily the spherical geometric model was used to set up the layered thickness of the PML. Further, the propagation of

acoustic waves and reflections from the sphere's boundary was observed before and after adding the PML domain. Establishing the PML for the cylinder was based on the data gained by implementing the PML in the spherical model.

Sphere: Two 3-dimensional (3-D) layered structured spherical model geometries shown in Figure 3.3, with different radii and having the same centre, were developed in COMSOL Multiphysics. The inner sphere was defined as polymer. The propagation behaviour of the acoustic wave was analysed in this region. To add a PML domain, an outer layered structure sphere around the polymer was taken, having a radius ten times the radius of polymer, and the thickness of the layer has dimensions three times the radius of the polymeric sphere [26].

Cylinder: An inner cylinder with a radius of 20mm and a height of 100cm, shown in Figure 3.4, was considered to analyse acoustic wave propagation. These dimensions were chosen with careful consideration given to computational resources and simulation time constraints. This approach ensured that the simulation process remained manageable and tractable while still capturing the essential aspects of acoustic wave behaviour within the chosen system. The layered structured outer cylinder was considered the PML region. The acoustic point source was placed midway (50cm) along the axial direction. Creating geometry and PML was the same as in the case of sphere.
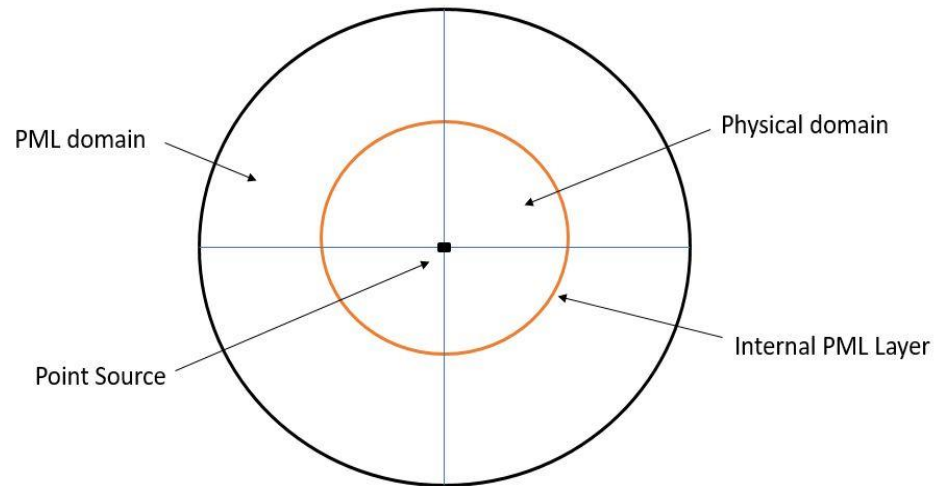
Figure 3.4: XY-view of cylindrical model geometry with PML.

3.6.2   PML setting and Meshing

PML Scaling Factors: PML scaling factor is crucial in adjusting the strength of the absorption within the PML region in numerical simulations. This factor controls the rate at which waves are absorbed as they propagate through the PML. By adjusting the scaling factors, we can control the absorption level and reduce reflections at the PML boundaries. Typically, PML scaling factor values greater than one indicates that the fields are attenuated as they enter the PML. A value of one would imply no attenuation, and a value less than one would imply amplification of the fields within the PML, which is undesirable.

The scaling factors can differ for different components of the wave. They may also be adjusted based on the simulated wave frequency. The region of interest in simulations was confined to the physical domain of the geometry, and there was no specific interest in the PML region if it perfectly absorbed the propagating wave. To explore the impact of the PML scaling factor, multiple simulations were

conducted, each time varying the scaling factor and observing the behaviour of the propagating wave. Interestingly, it was found that when the PML scaling factor was set to 0.5, there was no discernible effect on the propagating wave within the physical domain.

PML Scaling Curvature Parameters: PML scaling curvature parameters influence the behaviour of the PML by controlling the curvature of the stretched coordinates in the PML region. The stretched coordinates are used to transform the physical coordinates in the computational domain to the complex PML coordinates, allowing for the absorption of outgoing waves. The scaling curvature parameters determine the smoothness of the coordinate stretching function within the PML region. They control how quickly the mesh is compressed or stretched along the PML boundaries. Choosing appropriate scaling curvature parameters ensures that the PML effectively absorbs the outgoing waves without introducing numerical instabilities. The choice of scaling curvature parameters in the PML formulation depends on the specific characteristics of the simulated problem and the PML implementation used. A PML scaling curvature parameter of 1 was selected [26, 133].

Meshing: The swept mesh is commonly used in the PML region to ensure that the PML has a smooth and regular mesh. A structured mesh in the PML region helps to maintain numerical stability and accuracy while effectively absorbing outgoing waves. A smoothly varying mesh is essential to create an efficient and effective PML. Using a swept mesh in the PML region, the mesh elements are aligned along the direction of wave propagation, allowing for a better representation of the wave fronts. Therefore, six number of elements were selected in swept mesh to mesh the PML domain [123].

3.7 Summary

This chapter explained the modelling techniques employed to investigate the behaviour of AE signals propagating through polymeric insulation. Below are the critical points of the modelling techniques.

Modelling acoustic pulse propagation in COMSOL Multiphysics: this chapter explained the FEA based modelling technique used to simulate the acoustic pulse propagation in polymeric insulations using COMSOL Multiphysics. Further, it highlighted the essential aspects of the model, including the geometry, partial differential equations (PDEs) utilized for simulating the propagation of the acoustic pulse, parameters considered, boundary conditions, and initial assumptions. Furthermore, the utilization of the coordinate stretching technique has been proven to be highly effective in adapting the mesh to concentrate computational resources on significant areas of interest. This approach guarantees the accuracy and efficiency of the simulations, as it ensures that the important regions are given the necessary attention and resources.

MATLAB Model to Quantify Effects of Reflections and Scattering: A specialized MATLAB model was created to gain a better understanding of the effects of reflections and scattering on the propagation of acoustic pulses. This model was developed with the aim of analysing and comprehending the impact of these factors on the behaviour of the acoustic waves, and the results obtained from this research could be used to inform future studies in the field. Overall, the creation of this specialized model was an important step forward in advancing the knowledge of acoustic wave propagation and its related phenomena. This complementary model allowed to quantify these phenomena' effects on the

69

acoustic signal accurately. By systematically adjusting various parameters and conditions in the MATLAB model, the behaviour of the acoustic pulse in complex scenarios, such as the presence of different layers of insulation materials and varying discharging locations on branches of electrical trees can also be investigated.

Implementation of PML: To conduct a thorough analysis of the propagation characteristics of the acoustic pulse, a highly effective approach known as the PML was implemented in the COMSOL Multiphysics. The PML technique was chosen due to its ability to accurately absorb outgoing waves and prevent any unwanted reflections, thereby ensuring that the acoustic pulse terminates within the computational domain as intended. To further optimize the PML's absorbing capabilities and maintain numerical stability, the scaling factors and scaling curvature parameters were carefully tuned. This approach ultimately proved to be highly successful in achieving the desired results and gaining valuable insights into the behaviour of the acoustic pulse.

Overall, this chapter provides a comprehensive and integrated analysis of acoustic pulse propagation modelling techniques in polymeric insulations. The combined use of COMSOL Multiphysics and MATLAB modelling can investigate the complexities of the acoustic signal's behaviour, considering the effects of reflections, scattering, and PML implementation. These insights contribute to developing a robust and accurate AE detection technique, offering potential applications in monitoring discharging events and predicting insulation breakdowns in power cables.

Chapter 4

Results from Finite Element Analysis Modelling

4.1 Introduction

This chapter presents an analysis of acoustic pulse propagation with and without reflections and scattering in solid insulating medium using finite element analysis (FEA) based modelling in COMSOL Multiphysics and MATLAB. However, the approach can be useful to address the effects of reflections and scattering on propagating acoustic pulse in other media as well.

4.2 Acoustic Source

The electrostatic energy stored in the cavity present in the insulation of a 33-kV underground cable was estimated by using the approach described in chapter 3 and the resulting value was found to be $5.6*10^{-7}$J. It was further assumed that the energy stored in the cavity is converted into a pressure wave which propagates through the insulation material. Further, the amount of pressure developed by this energy was found to be $P = 135\ Pa$. This was used to define the peak value of acoustic pulse to analyse the propagation characteristics AE in COMSOL Multiphysics.
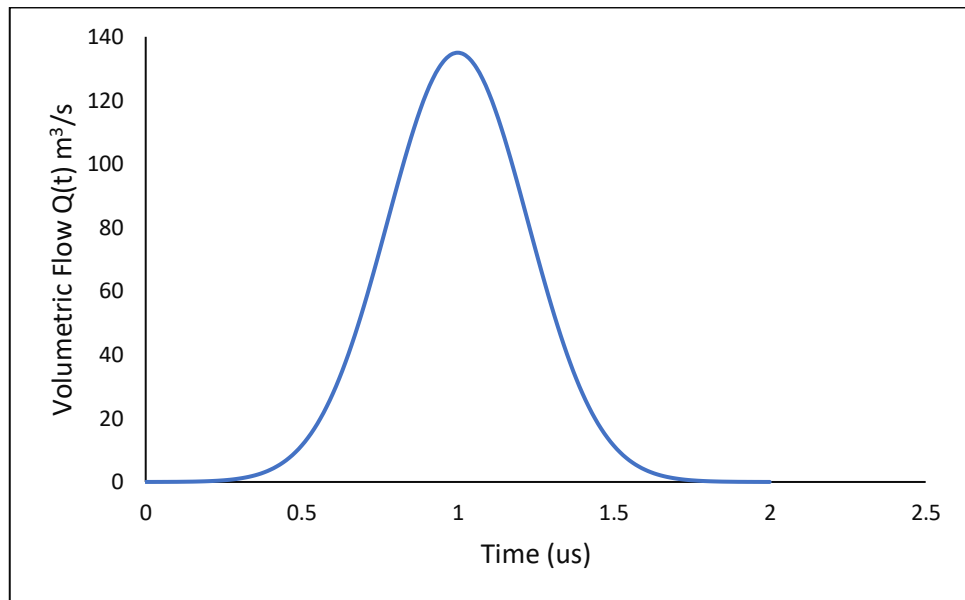
Figure 4.1: The gaussian point source excitation function at S(0, t). Q(t) correspond to the pressure related to the discharge event.

4.3 Results and Discussion

4.3.1 COMSOL Multiphysics:

The propagation of acoustic pressure pulse generated by the point source in a cylindrical geometry was analysed at different points along the axial direction of the cylinder. It was observed that the propagating acoustic pulse is spherical in shape and once the wave front reaches the radial boundary of the cylinder, it is reflected due to the mismatch in acoustic impedance between the polymer material and the surrounding air.

The complexity introduced by reflections from the radial boundary of the cylinder posed challenges in analysing the pulse shape and peak magnitude. To address this issue, an initial strategy was employed by transitioning to a spherical model geometry. A point source was placed at the centre of this spherical model,

as detailed in Chapter 3. It was observed that spherical models exhibited reflections from the respective boundaries. These reflections caused a shift in the shape and magnitude of the acoustic pulse, and the extent of the shift in pulse shape and magnitude depended on the number of reflections.

The data collected from the spherical model geometry was used to implement the cylindrical geometry and the propagating pulse was observed at different locations of the cylinder.

Figure 4.2: Detection of propagating acoustic pulse at 40cm along the axial direction of a cylindrical model with boundary reflections causing pulse shape distortion.

Figure 4.2 depicts the propagation of pressure pulse within a cylindrical model, in polyethylene and XLPE materials. Notably, the shape of the detected acoustic

pulse deviated from the initial Gaussian pulse shape in both polymeric materials, exhibiting distortion. This distortion was attributed to reflections occurring from the radial boundary of the cylinder. These reflections, resulting from the interaction of the acoustic pulse with the boundaries of the cylindrical structure, caused alterations in the pulse shape, leading to the observed deviations from the original Gaussian profile.

4.3.2   MATLAB Model:

During the investigation of the effects of reflections on the propagating acoustic pulse, a MATLAB pulse propagation model was utilized to conduct additional analysis to gain deeper insights. This computational approach enabled an exploration of the impacts and behaviour of the pulse in the presence of reflections. The initial simulation of the pulse propagation involved configuring the model to account for a single propagation path. Upon plotting the resulting pulse, it was observed that there were no discernible effects on the shape of the pulse. However, to accurately simulate the real-world scenario, the model was subsequently modified to simulate the pulse propagation through multiple paths, and the output was plotted again. The results are illustrated in figure 4.3.

The MATLAB model showed that the shape, peak magnitude, and the arrival time of an acoustic pulse are significantly influenced by the number of propagation paths considered. This implies that detecting and locating PD in high voltage insulation materials using acoustic detection techniques, regardless of the material's state (solid, liquid, or gas), is challenging without considering the effects of multiple propagation paths or reflection phenomena. Furthermore, the characteristics of acoustic pulse propagation cannot be accurately analysed solely

based on the results obtained from the COMSOL modelling. This is because the effects of the multiple path lengths and reflections must be eliminated to obtain a clear understanding of the true nature of acoustic pulse propagation. Therefore, the MATLAB pulse propagation model serves as a useful tool for gaining a more accurate understanding of the behaviour of acoustic pulses in the presence of multiple propagation paths and reflections. The results can be used to quantify the effects of reflections on the shape, peak magnitude, and the arrival time of the pulse. Figure 4.3 depicts the effects of 10 and 100 reflections on the propagating pulse in MATLAB. More number of reflections can be considered using this model however, that will require more computational resources and time.
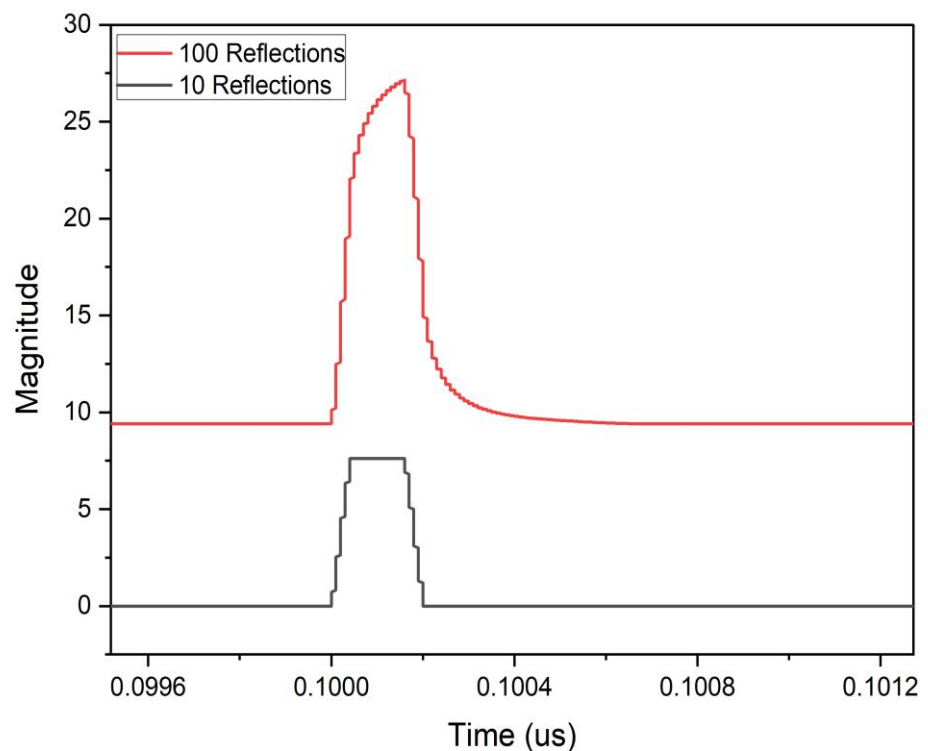
Figure 4.3: Effects of reflections on the propagating acoustic pulse from MATLAB model with magnitude in arbitrary units (a.u.) along y-axis.

4.3.3   Perfect Matched Layer (PML):

The perfect Matched Layer (PML) is a common technique used to absorb outgoing waves in numerical simulations of wave propagation. The absorption properties can be adjusted by specifying the width of the PML. Therefore, to mitigate the effects of reflections on the propagating acoustic pulse in the above model, a perfect matched layer (PML) was implemented in COMSOL Multiphysics. The detailed procedure for this implementation is explained in chapter 3.

4.3.4   Model geometry:

As discussed in chapter 3, implementing the PML for a cylindrical geometry with radial thickness much smaller than the length of the cylinder is a challenging task. Therefore, to simplify the model, spherical geometry was used to analyse the performance of the PML, and data was then used to implement the PML on cylindrical geometry. The propagation of acoustic wave in a sphere at different time is shown in figure 4.4.
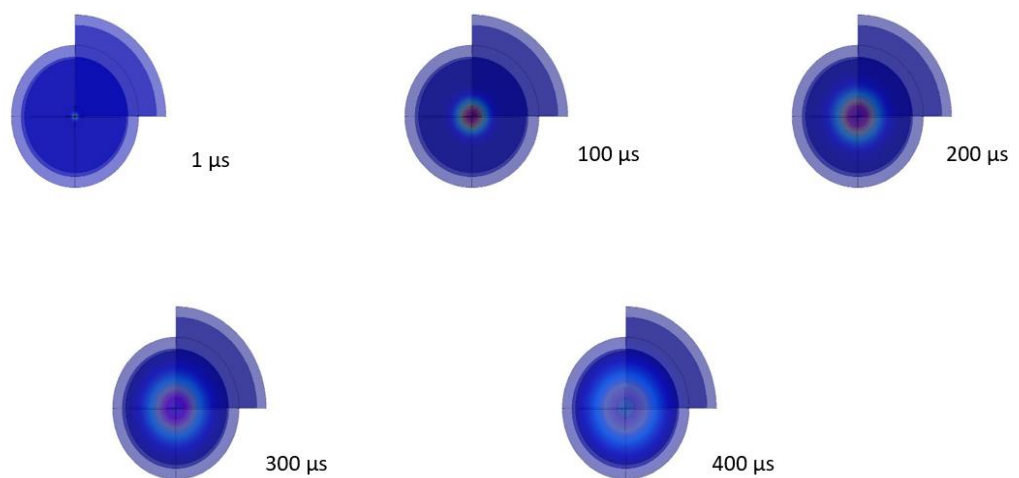
Figure 4.4: Acoustic pulse propagation in spherical model geometry.

76

Figure 4.4 shows that the acoustic wave propagates with a spherical wave front. The amplitude of the spherical wave is inverse square of the radius of the wave front. This was confirmed in spherical model of the geometry. Moreover, no reflections were observed from the boundary of the sphere and the propagating pressure pulse was absorbed by the PML.

The data obtained from the spherical model was used to implement the PML in cylindrical geometry.
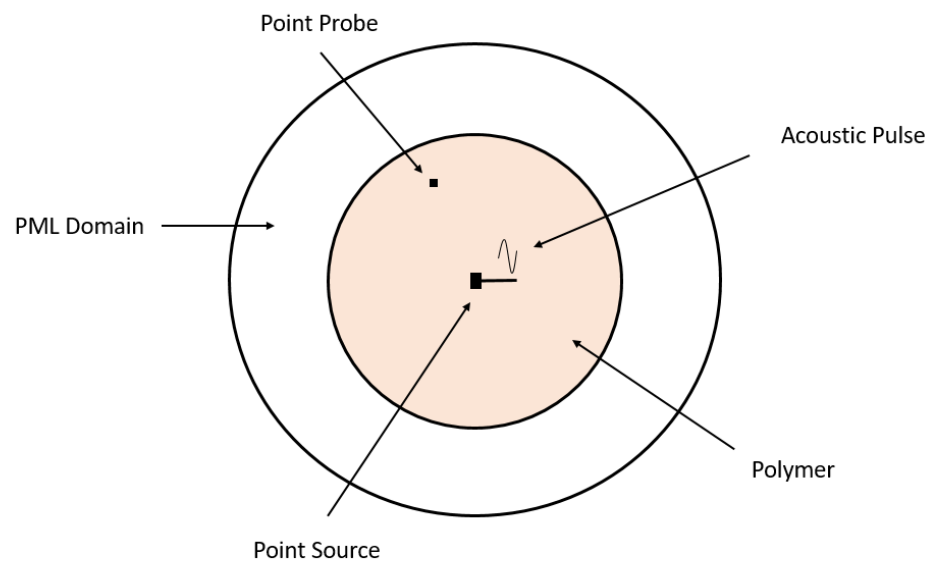
Figure 4.5: XY cylindrical model geometry with PML implemented in COMSOL.

The COMSOL model was run to observe the propagation of acoustic pulse after the implementation of PML. With the implementation of PML in the COMSOL simulation model, the distortion caused by reflections during the propagation of acoustic pulse was mitigated. This resulted in an undistorted shape of the propagating pulse, as compared with the model without PML. Figure 4.6 shows

the acoustic pulse detected at 40 cm away from the source in cylindrical model geometry using polyethylene and XLPE.
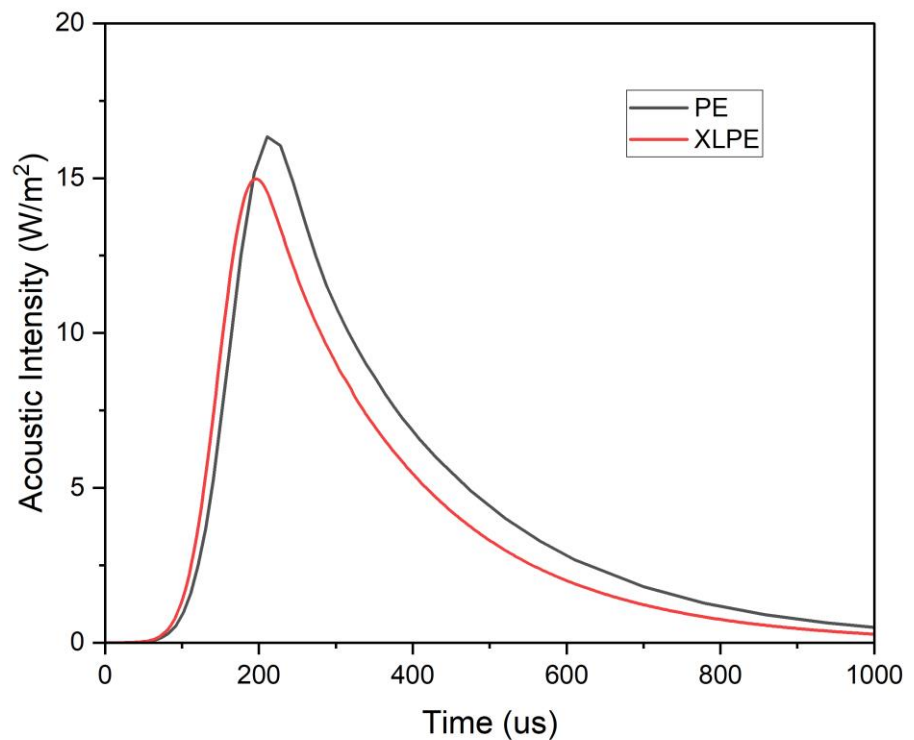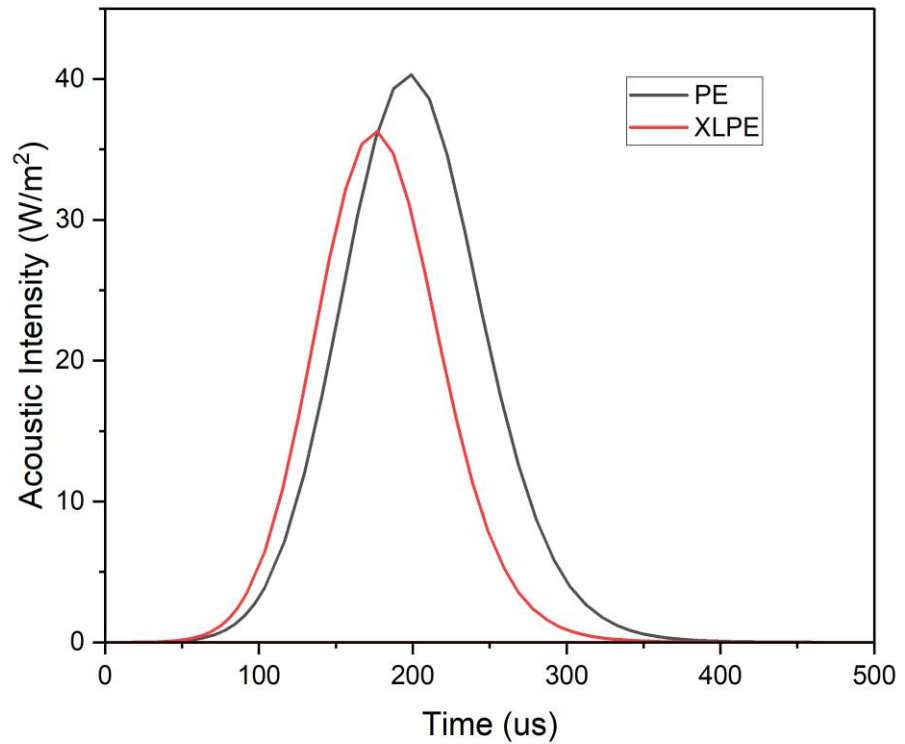

Figure 4.6: Detection of propagating acoustic pulse at 40cm along the axial direction of a cylindrical model after implementing PML.

Further, the propagating acoustic pulse was analysed at different locations away from the source after the implementation of the PML to observe the decay peak magnitude of the propagating acoustic pulse. It was observed that the peak magnitude of the propagating acoustic pulse decreases with distance as shown in figure 4.7. This decay in peak magnitude can be described by the inverse square law, where the decay is proportional to the square of the distance from the source. This significant decay in magnitude restricts the use of acoustic emission technique to detect the PD event in solid insulating materials for longer distances but, has the

potential of being usable for joints; bushings, etc where long distances are not required.
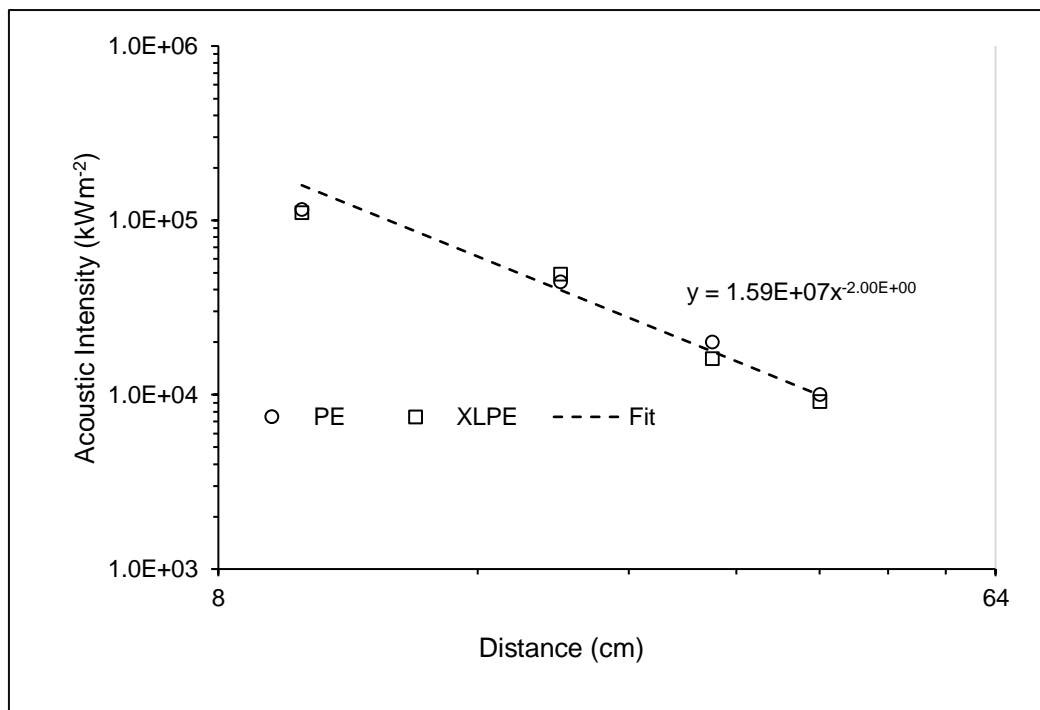
Figure 4.7: Drop in magnitude of acoustic pulse intensity with distance in PE and XLPE.

4.4 Discussion:

The MATLAB and COMSOL simulation models provide valuable insights into the propagation of acoustic pulse in polymeric insulating materials. The MATLAB model demonstrate that multiple paths of a propagating acoustic pulse can alter not only its shape and magnitude but also the arrival time of the pulse. The same behaviour was observed during the COMSOL simulation prior to applying the PML. From figure 4.2, the distortion in the shape and magnitude of the propagating acoustic pulse analysed from the COMSOL Multiphysics model without implementing the PML can be correlated to the results from the MATLAB model

in terms of a shift in the shape and magnitude of the propagating acoustic pulse. However, the distortion in pulse magnitude and shape in COMSOL model is greater than in the MATLAB model which can be observed from figure 4.2 and 4.3. This could be due to the fact that the MATLAB model is limited to simple geometry and idealized conditions, while the COMSOL simulation allows for more realistic modelling of geometry and physical conditions.

The MATLAB simulation model revealed that multiple paths can impact the arrival time of the acoustic pulse, higher number of paths can not only shift the shape and magnitude of the pulse but also cause a delay in the arrival time of the pulse as shown in figure 4.3. This finding is significant in practical applications, particularly in locating the source of PD in transformer oil where the reflections and scattering can be high. In such scenarios, reflections or multiple paths can affect the arrival time of the pulse, which is used to estimate the location of PD source. The quantified relationship between the number of paths and delayed arrival time of the pulse can help improve the accuracy of locating the source of PD.

The propagation characteristics of the acoustic pulse was further analysed by the implementation of PML in acoustic pulse propagation model in COMSOL, which revealed that the PML is effective in reducing reflections and preserving the amplitude of the propagating pulse. This is particularly crucial in scenarios with complex boundaries and geometries, which can cause significant interference and distortion without PML. The results revealed that the decay in magnitude of the propagating pulse was high for both PE and XLPE as shown in Figure 4.7. The significant decay in magnitude is attributed to the interaction between the emitted spherical wave front from the source and the geometry of the system. As the wave

front originates from the source along the axial direction, the radial boundary of the thin cylinder serves as an absorbing boundary, causing a rapid decrease in observed intensity with distance. The increasing radius of the spherical wave front leads to a reduction in the effective portion of the wave front observed within the cylinder, while a substantial portion is absorbed by the radial boundary as shown in Figure 4.8.
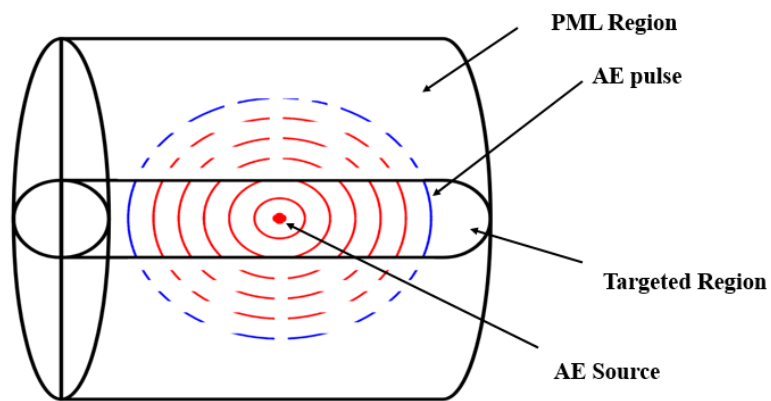
Figure 4.8: Propagation of spherical AE pulse in cylindrical geometry.

Overall, the simulation models revealed that by accounting the effects of multiple paths, more accurate detection techniques can be developed, leading to a better maintenance and safety practice in various industries. The study`s approach of using a spherical model and later designing a cylindrical model can also be applied to more complex geometries in practical settings.

Chapter 5

Experimental Techniques

5.1 Introduction

This chapter explains the experimental techniques employed to investigate the behaviour of acoustic pulses in polymeric insulations. The experimental techniques used to analyse the chemical and dielectric characteristics are also explained. The chapter is divided into two parts, each addressing different aspects of the research.

- Acoustic Pulse Initiation and Propagation Analysis: This part of the chapter focuses on the experimental techniques used to study the initiation and detection of acoustic pulses. In addition, preparation of sample rods of the polymeric insulation materials to analyse the propagation characteristics of the acoustic pulse in these materials are discussed. The primary objective was to explore the feasibility of using AE as a reliable technique for early detection of discharging events within power cable insulations.

- Chemical and Electrical Characterization of Polymeric Materials: The latter part of this chapter explains the experimental setup to analyse the physical and chemical characteristics of the polymeric materials used in this study.

To gain a better understanding of the properties of the materials, various characterization techniques were employed. Differential Scanning Calorimetry (DSC) analysis was utilized to investigate the thermal behaviour of the polymeric materials used in this study, this includes thermal transitions and phase changes. Additionally, Fourier Transform Infrared Spectroscopy (FTIR) was utilized to analyse the materials' structure and chemical bonds.

Moreover, dielectric spectroscopy was applied for analysing the electrical behaviour of materials by examining their dielectric response and relaxation processes. Additionally, direct current (DC) conductivity measurements were used to explore the electrical conduction mechanisms of the materials, providing further clarity on their electrical properties.

5.2 Acoustic Pulse Initiation and Propagation

This section delves into the experimental techniques employed to gain an understanding of acoustic pulse initiation and propagation in polymeric insulations. To achieve this objective, a carefully designed experimental setup was employed to generate acoustic pulses and study their propagation through various polymeric materials. The primary aim was to analyse the interaction between the pulses and the material matrix to gain insights into the acoustic pulse's propagation characteristics in different polymeric materials. This involved investigating the acoustic pulse's propagation speed, attenuation in the peak magnitude of the propagating acoustic pulse, attenuation in energy of the propagating acoustic pulse, and the effect of material on the frequency spectrum of the pulse as it propagated

through the material. Understanding these interactions is vital for the development of acoustic detection methods for insulation fault diagnosis.

5.2.1 Materials and Sample Preparation

For this study, one-meter-long rods of PU were obtained from PAR Group Ltd while, PP, and Nylon were obtained from Stockline Plastic Limited. The PU rods were further classified into three distinct categories based on their hardness levels using the Shore scale ranging from 40° A to 90° A. The categories included soft (40°A), medium (70°A), and hard (90°A). Shore hardness is a measure of the resistance of a material to indentation or penetration by a harder object. It is commonly used to assess the hardness of polymers, elastomers, and other materials. Table 5.1 obtained from the PAR group along with the PU rods illustrates how the properties of PU are correlated with Shore hardness values.

Table 5.1: Properties of PU samples on Shore Scale hardness [126].

Properties	Test Method	Unit	Value				
Hardness	DIN 2240-91	Shore A	55	60	65	70	75
100% Modulus	BS 903 Pt A2 - ISO 37	lb/in² (Mpa)	200 (1.4)	230 (1.6)	260 (1.8)	360 (2.5)	530 (3.7)
300% Modulus	BS 903 Pt A2 - ISO 37	lb/in² (Mpa)	330 (2.3)	440 (3.0)	440 (3.0)	980 (6.8)	1140 (7.9)
Tensile Strength	BS 903 Pt A2 - ISO 37	lb/in² (Mpa)	1800 (12.4)	2990 (20.6)	3660 (25.3)	5730 (39.5)	6500 (44.9)
Elongation @ Break	BS 903 Pt A2 - ISO 37	%	800	790	680	640	630
Tear Strength	BS 903 Pt A3 - ISO 34-1	lb/in (KN/m)	195 (34.1)	185 (32.4)	215 (37.6)	350 (61.3)	385 (67.4)
Compression Set	BS 903 Pt A6 - ISO 815	%	20	23	24	24	26
Abrasion Loss	DIN 53516	mm³	39	40	36	30	23
Resilience	ASTM D 2632-92	%	65	60	45	44	44
Specific Gravity	-	g/cm³	1.21	1.21	1.21	1.21	1.21

Properties	Test Method	Unit	Value			
Hardness	DIN 2240-91	Shore A	80	85	90	95
100% Modulus	BS 903 Pt A2 - ISO 37	lb/in² (Mpa)	740 (5.1)	890 (6.1)	1240 (8.6)	1580 (10.9)
300% Modulus	BS 903 Pt A2 - ISO 37	lb/in² (Mpa)	1420 (9.8)	1570 (10.8)	2420 (16.7)	2600 (17.9)
Tensile Strength	BS 903 Pt A2 - ISO 37	lb/in² (Mpa)	6230 (43.0)	5840 (40.3)	5060 (34.9)	4430 (30.6)
Elongation @ Break	BS 903 Pt A2 - ISO 37	%	610	630	610	560
Tear Strength	BS 903 Pt A3 - ISO 34-1	lb/in (KN/m)	460 (80.5)	490 (85.8)	580 (101.5)	660 (115.5)
Compression Set	BS 903 Pt A6 - ISO 815	%	26	24	22	22
Abrasion Loss	DIN 53516	mm³	25	30	36	39
Resilience	ASTM D 2632-92	%	42	40	37	35
Specific Gravity	-	g/cm³	1.22	1.22	1.23	1.24

The rationale behind selecting three types of PU materials with different hardness levels was to observe the impact of hardness on the propagation characteristics of acoustic pulse as PU has a correlation between hardness and its self-healing capabilities. These characteristics included the speed of propagation, attenuation in acoustic magnitude, and attenuation in the frequency of the propagating acoustic impulse with distance.

Furthermore, to enhance our understanding of the impact of polymeric structure on the propagation characteristics of the acoustic pulse, additional polymeric families, namely Nylon and PP, were included and investigated in this study. These additional materials were helpful in conducting a comparative study of different polymer families. The inclusion of Nylon and PP in the study allowed an investigation to better understand PU's behaviour in comparison to other polymer

types. This investigation helped to establish a solid foundation for interpreting and understanding the experimental results before drawing any conclusions about PU's behaviour.

To observe the propagation characteristics of acoustic pulse, different rod lengths were cut for each material. The selection of rod length for each material was based on experimental observations, specifically focusing on the detectability of the acoustic signal. To make the study easier to understand, specific terms will be used to refer to the different samples of PU based on their Shore scale hardness ratings. PU with a rating of 40°A as PU40, PU with a rating of 70°A as PU70, and PU with a rating of 90°A as PU90. Additionally, the abbreviations PP for polypropylene and Nylon for Nylon 6.6 will be used to maintain consistency in referring to the materials. The choice of the length of the cylinder for each polymer was made by the propagation capability of the acoustic signal in these materials observed during the experiments in laboratory.

Table 5.2: The length of samples for various PU specimens

Material	Length of the rod (cm)
PU40	10, 20, 30, 40, 50, 60, 70
PU70	10, 20, 30, 40, 50
PU90	10,20,30,40
Nylon	10, 20, 30, 40, 50, 80
PP	5, 10, 15, 20, 25

5.3   Experimental Setup

5.3.1   Initiation of Acoustic Pulse

Using a needle-needle electrode topology (stainless steel gramophone needles of 1mm diameter and tip radius of 5 ± 1 µm) with a 2mm separation, a discharge was created in air 30mm away from the surface of the rod to initiate the AE signal as shown in Figure 5.1. A 3.5 kV (adjustable) DC high voltage source was used to charge a 100-pF capacitor. A 34 MΩ resistor was used to increase the time constant for charging. Once the capacitor was charged it was isolated from the supply and a second switch was closed to connect the capacitor to the electrodes causing a discharge event. A Tektronix High voltage probe P6015A, which has a bandwidth of 75MHz was used to monitor the voltage across the gap and a high frequency current transformer HFCT100, (4.7V/A sensitivity, 100 kHz – 20 MHz -3dB frequency response, 22 ns risetime response) was used to monitor the current in the gap during the discharge event. The signals from these probes were recorded using a Tektronix oscilloscope (TDS2024, 200MHz, 2GS/s), referred to as Scope 1.
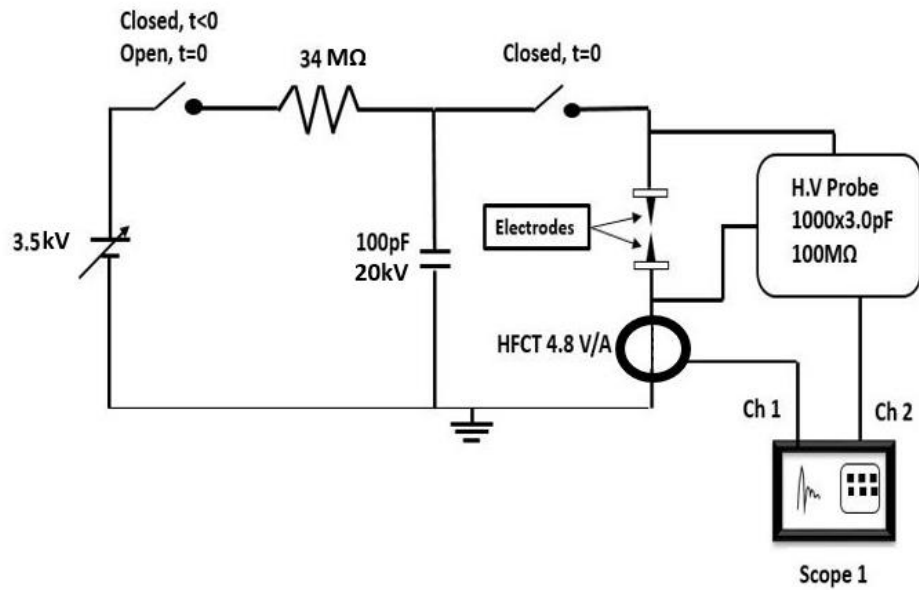
Figure 5.1 Experimental set up to charge the capacitor and subsequently creation of electrical discharge to initiate the acoustic signal.

5.3.2   Detection of acoustic Signal

Figure 5.2. shows the acoustic measurement arrangements. A R15I-AST 150 kHz, AE acoustic sensor with integral preamplifier (Physical Acoustics, MISTRAS Inc) was used to detect the AE signal. This sensor has a nominal frequency operating range of 50-400 kHz and a resonant frequency of 150 kHz (ref V/μbar) [126]. Figure 5.2 shows the setup to record the AE signal initiated by a discharge across the electrodes and propagating through the PU rods. The AE signal from the acoustic transducer was fed to Scope 2, (Tektronix oscilloscope (TDS2024, 200MHz, 2GS/s) where it was recorded for further analysis. The signal from the HFCT was also fed to this scope to allow the triggering of the two scopes to be synchronised. This allowed different timebases to be used on the two scopes:

which enabled the capture of the fast transients associated with the electrical signals, which were of the order of 100 ns, while also allowing the propagation time of the acoustic pulse to be considered which was of the order of 500 μs.

The AE signals from the discharge were analysed for each polymeric rod of different lengths. The rod's maximum length was chosen according to the propagation capability of the acoustic pulse in each type of polymer. The 10 cm long rod was used as a starting point and then the longer rods were used until the AE signal could not be detected.
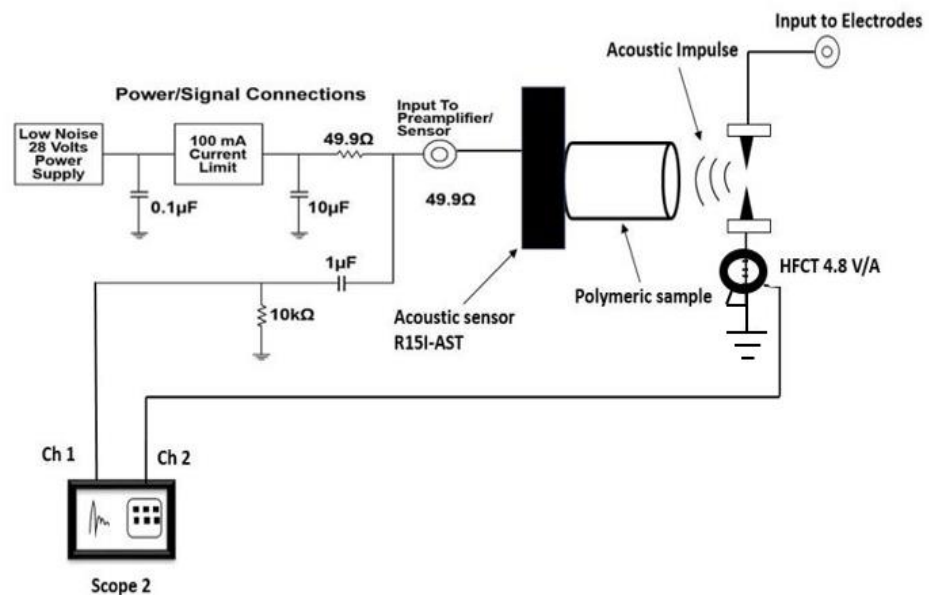
Figure 5.2: Experimental set up to record the propagating acoustic pulses.

5.3.3   Signal Processing

The illustration presented in Figure 5.3 shows a representative example of the response of the sensor. The output of the acoustic transducer attached to the rod is a voltage. To convert these voltage signals into pressure signals in Pascals the calibrated response of the sensor was utilized to establish a transfer function. This

transfer function allowed the conversion of the recorded data from the sensor into the corresponding pressure values.

The analysis of the frequency spectrum of the acoustic signal propagating through various polymeric rods was conducted through the utilization of the Fast Fourier Transform (FFT). To ensure the precise signal's frequency content, a sampling frequency of 25 MHz was chosen based on the time interval between recorded data points which was 40 ns.
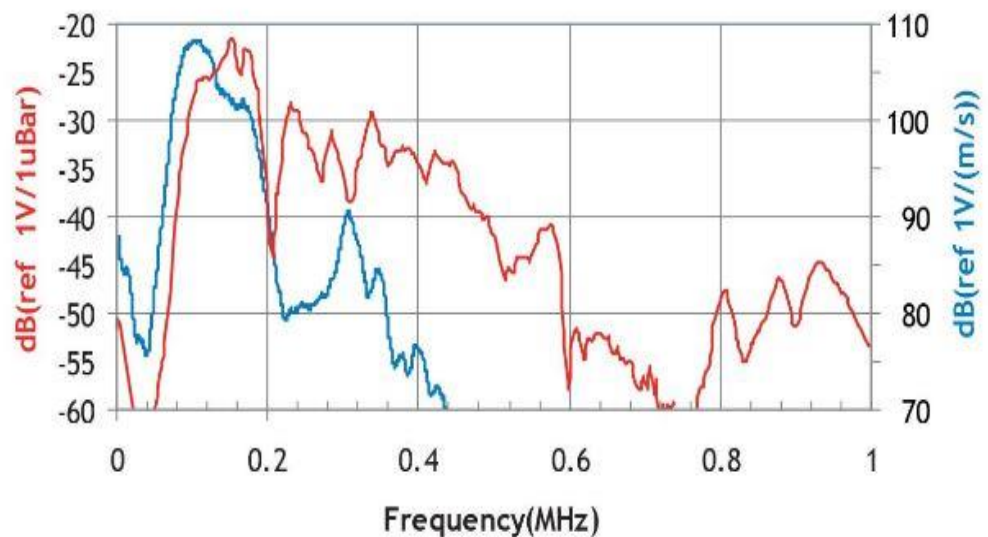
Figure 5.3: The standard response of the R15I-AST acoustic sensor [126].

Figure 5.3 illustrates the standard response of the R15I-AST sensor. In the graph, the blue function represents the standard response in decibels (dB) with reference to 1 volt per meter per second (1 V/(m/s)), providing a measure of the sensor's sensitivity and output in relation to velocity. Concurrently, the red function in the figure represents the dB reference with 1 volt per microbar (1 V/1µBar), indicating another perspective of the sensor's response in terms of pressure. These representations highlight its sensitivity under different reference conditions, aiding

in the interpretation and utilization of the sensor's output. Through the utilization of the standard response of the R15I-AST sensor, a series of manual calculations were conducted to ascertain the transfer function of the sensor. The primary aim of these calculations was to establish a direct correlation between the output voltage of the sensor and the corresponding pressure measurement in Pascal.

To acquire a larger-sized image of the standard response, a physical copy of the image was printed onto an A3 page. From there, the data extraction was initiated manually on both the x and y axes to ensure maximum accuracy and precision in the resulting data.

In total, 500 data points were recorded on the x-axis, each accompanied by its corresponding y-axis value. These recorded values were then plotted using the MATLAB.

To refine the representation of the data, linear interpolation was applied. This method was chosen to increase the number of data points in the original signal, thereby enhancing the resolution of the dataset. By interpolating additional data points, the signal could be analyzed with greater detail and granularity. However, it was ensured that the interpolated data points did not exceed the values of the corresponding original signal to avoid introducing inaccuracies.

The purpose of employing linear interpolation was to achieve a smoother representation of the data. Despite its effectiveness in enhancing the resolution and smoothing the signal, it is important to acknowledge the limitations of this interpolation method. Linear interpolation may not fully capture all the subtleties in the sensor's response, particularly in cases of rapid or non-linear changes in the signal. Therefore, while the interpolated data provided a more refined

representation for further analysis, it's essential to consider its potential limitations and exercise caution in interpreting the results.

The transfer function that was derived from this calibration process allowed to convert the recorded data from the sensor into meaningful pressure values and was useful in analysing the frequency spectrum of the detected acoustic signal. This conversion facilitated a more accurate analysis and interpretation of the acoustic signal.

5.4 Chemical and Electrical Characterization

5.4.1 Differential Scanning Calorimetry (DSC)

The thermal properties of the polymers were analysed using DSC. The measurement was carried out using a TA Q1000 DSC instrument. Prior to measurement, the instrument was stabilized at a temperature of -40°C to ensure an accurate and consistent baseline while also eliminating any possible thermal effects in the system. This initial step is crucial in establishing a reliable starting point for the DSC measurement.

Once the equilibration process was complete, the temperature was increased at a steady pace of 10°C per minute until it reaches a maximum of 300°C, while N_2 was used as purge gas with a flow rate of 40 mL min^{-1}. In the controlled heating process, the instrument facilitates the measurement of changes in heat capacity as a function of temperature. This enables the determination of thermal transitions associated with the material's morphology, such as crystallization, melting, phase transitions, or decomposition.

5.4.2 Fourier Transform Infrared Spectroscopy Fourier transform infrared (FTIR)

In material science, one of the most important techniques used for analysing chemical composition is Fourier Transform Infrared (FTIR) spectroscopy. This method involves the measurement of the interaction between a material and infrared light, which provides valuable information on its chemical structure and composition.

To investigate the dielectric characteristics of the polymeric materials used in the study such as DC conductivity, dielectric response, and dielectric breakdown strength, small pieces of each material were cut from the respective rods and melted under hot press to form thin sheets. However, melting process can have a significant impact on the chemical composition of the material. To understand the chemical structure of the polymers used in this study and the effects of the melting process on the physical and chemical composition of the polymers, each polymer piece was subjected to FTIR analysis before and after undergoing the melting process.

To carry out the FTIR analysis, the small pieces weighing 300mg and the thin sheets of thickness 260 µm obtained by melting the small pieces of each material were evaluated with a Nicolet iS5 FTIR spectrometer with Specac GoldenGate ATR accessory, to obtain the FTIR spectra. Data was collected by averaging 64 scans from 500 to 4000 cm^{-1} at a resolution of 4 cm^{-1}. The resulting FTIR data for small pieces and thin sheets of each material was recorded to explore the chemical structure of the polymers. Moreover, the obtained spectra for each small piece were

compared to the respective thin sheet to record any physical or chemical change in material structure due to the melting process.

5.4.3 Preparation of Thin Film Samples

To investigate the dielectric characteristics of the polymeric materials, small pieces weighing 300 mg were cut from each type of polymeric rod and were melted to make thin films. The melting process was conducted using a 15-ton manual hydraulic press machine from Graseby Specac, employing a temperature according to the melting temperature of each material which was 200 °C for each type of PU, 175°C for PP, and 275°C for Nylon. A thin sheet of aluminum with a thickness of 300 µm with a circular hole of diameter 45 mm was used to act as a mold. A small piece of polytetrafluoroethylene (PTFE) film, measuring 50 µm in thickness and 70 mm in diameter, was placed on the lower plate of the hot press. The mold was then carefully positioned on top of the PTFE film, ensuring that the hole of the mold was covered by the PTFE film.

The small pieces of polymeric rods weighing 300mg were placed at the center of the hole on top of the PTFE film and an additional piece of PTFE film was added on top of the mold to cover the polymeric pieces, preventing direct contact with the hot plates and allowing for uniform heating from both the top and bottom plates of the hydraulic press. The use of PTFE film was advantageous due to its higher melting point and its ability to enable the melted polymer to cool and form a thin sheet on its surface. This thin polymeric film deposited on the PTFE film could be easily isolated as it did not stick to the film after cooling, making it a highly efficient and successful method for the preparation of thin films for further analysis.

The samples were carefully positioned between the hot plates for 15 minutes while a 5-ton load was applied. The load was released and reapplied five times to eliminate trapped air within the samples. Afterwards, the melted PU was allowed to cool under the hydraulic press until the temperature dropped to 75 °C. Following this, the samples were gently removed from the hydraulic press alongside the hot plates and allowed to cool at room temperature for 5 minutes. Subsequently, the thickness of these thin samples was measured using a micrometre (Mitutoyo, 0-25mm, 0.01mm), resulting in thin films with an average thickness of $260 \pm 10 \mu m$.

5.4.4   Dielectric Spectroscopy

Dielectric spectroscopy is a highly effective and widely adopted technique that is utilized to investigate the dielectric properties of insulating materials in relation to frequency. It involves the study of the interaction between an external electric field and the electric dipoles that exist within the material, which are commonly expressed as complex permittivity.

To evaluate the dielectric response of the prepared samples at various frequencies, dielectric spectroscopy was conducted. The samples were positioned between parallel plate electrodes made of stainless steel, each with a diameter of 35 mm and a guard ring electrode is placed around the measurement electrode to create a shielding effect as shown in Figure 5.4. To measure the capacitance and dielectric loss tangent of the samples, an LCR meter (ET4510, East Tester) was utilized in AC mode, covering a frequency range from 100 Hz to 100 kHz, with a signal amplitude of 1 V. The capacitance values obtained from the LCR meter were used to compute the relative permittivity of the samples through analytical calculations.

The measured capacitance of the thin samples, obtained from the LCR meter, can be represented using equation 5.1.

$$C_m = C_{st} + \varepsilon_0 \varepsilon_r \frac{A}{d} \qquad (5.1)$$

Where, C_m is the capacitance of the sample measured by the instrument, while C_{st} is the stray capacitance. To mitigate the effects of the stray capacitance, the experiment was repeated without the polymeric sample and the air capacitance was measured using the same electrode setup and same electrode separation distance as in case of thin polymeric film. The measured air capacitance can be represented as:

$$C_{mair} = C_{st} + \varepsilon_0 \frac{A}{d} \qquad (5.2)$$

The actual capacitance of the sample can be calculated analytically by using the relation:

$$C_{act} = C_m - C_{mair} \qquad (5.3)$$

$$C_{act} = \varepsilon_0 \frac{A}{d} [\varepsilon_r - 1] \qquad (5.4)$$

So, the relative permittivity can be represented as.

$$\varepsilon_r = 1 + \left(\frac{C_{act}}{\varepsilon_0 \frac{A}{d}} \right) \qquad (5.5)$$

The real relative permittivity and dielectric loss tangent of each type of polymeric sample were calculated; ten samples were tested to ensure reproducibility of the test data and an overall accuracy of ± 5 % is estimated using

the standard deviations in the measured results based upon repeated measurements from a similar set of test samples.
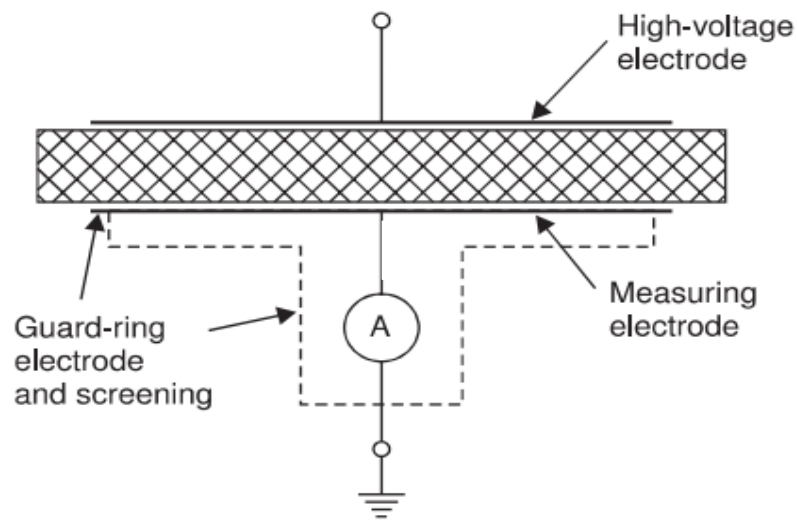
Figure 5.4: Experimental arrangement for conducting dielectric spectroscopy on the samples.

5.4.5   DC conductivity measurement

The dielectric response of the prepared samples was evaluated using dielectric spectroscopy across a range of frequencies. The samples, with a diameter of 40 mm and an average thickness of 260 ± 10 μm, were positioned between stainless steel parallel plate electrodes, each with a diameter of 35 mm. An LCR meter (ET4510, East Tester) operating in AC mode was employed for the measurements, covering a frequency range of 100 Hz to 100 kHz with a signal amplitude of 1 V.

In addition to the dielectric response, the DC conductivity of each PU variant was assessed using the same samples and electrode setup. A Keithley 617 programmable electrometer was utilised to apply a range of DC voltages from 10 V to 100 V, simultaneously recording the corresponding output current. Due to the

presence of charging transients when the voltage was applied, it was necessary to allow a period for the current to stabilize to its DC value for each voltage input. To ensure that the obtained values for the output DC current were reliable and accurate, a time delay of 10 minutes was used before recording the value of the current. After this time, the output current approached a steady state, and these isochronal measurements were regarded as representing the DC current.

In addition, ten samples of each material were tested to analyse the DC conductivity. The mean and standard deviations of each set of 10 measurements were calculated to obtain understanding of the DC conductivity of the thin polymer sheets.

5.5 Electrical Breakdown Test

Precision is crucial when conducting laboratory-scale analyses. This necessitates the use of specific testing methods and electrode geometries. There are two commonly used methods to test the dielectric breakdown strength, i.e., the constant-stress test determines the time-to-breakdown at a consistent electric field, while the progressive-stress test measures the electrical field magnitude at breakdown over time. Interestingly, the progressive-stress test is preferred due to its superior consistency compared to the equivalent constant-stress test [134]. However, the choice of testing method depends on the critical control of the electric field, as even slight variations can significantly impact the time-to-breakdown.

Furthermore, the electrode geometry is of utmost importance, with the needle-plate arrangement being popular due to its simplicity. Nevertheless, concerns

regarding the localized stress concentrations leading to premature failure require careful consideration. Alternative geometries, such as the plate-plate setup or configurations similar to it, aim to overcome these challenges while maintaining uniform stress gradients [135].

5.5.1 AC Breakdown Test

The samples used for AC breakdown testing were prepared following the same procedure as described for dielectric spectroscopy. Thin polymeric sheets with 40 mm diameter and thickness of $260 \pm 10\,\mu$m were utilized to assess the breakdown strength of the polymers. The AC breakdown testing was conducted in accordance with the guidelines specified in ASTM Standard D149-87 [136, 137]. Figure 4.5 illustrates the main components used in the test equipment, with components subjected to high voltage enclosed within an interlocked safety cage for safety purposes. The test cell featured a spherical-plane electrode system, wherein a 3mm diameter copper ball bearing served as the high-voltage electrode, and a circular plane electrode of diameter 30mm acted as the grounding electrode.
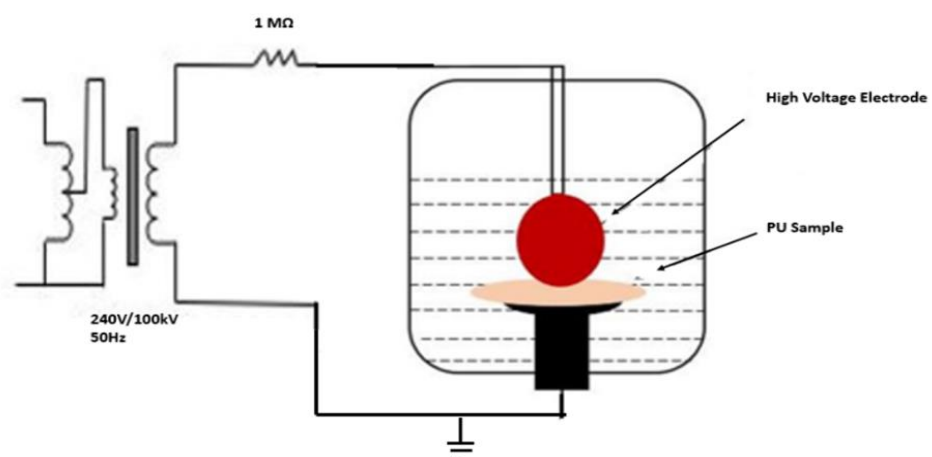
Figure 5.5: AC breakdown test setup.

To prevent surface flashover, the electrodes and the samples were immersed in dielectric liquid (Synthetic Ester MIDEL 7131). The plain electrode was fixed a little above the bottom of the test cell in dielectric liquid and the sample was placed on the plane electrode. The spherical electrode was mounted on the end of a rod which passed through a mounting in the lid of the test cell. The position of the spherical electrode was then adjusted to ensure that it was in contact with the sample without subjecting it to pressure and the mounting was used to lock the position of the rod. After every breakdown test, the lid of the test cell was removed and then placed again as shown in Figure 5.5. This ensured consistent pressure on all samples under the test. The tests followed the ASTM D149 and IEC 60234 standards, employing a short-time test technique. An AC voltage with a step voltage of 1 kV every 20 s was applied until the sample punctured. Each type of material underwent fifteen breakdown tests, while each sample underwent only three tests at different positions to prevent any potential flashover at the punctured sites. The breakdown voltage was then divided by the thickness of the thin film to determine the breakdown field. The resulting breakdown data was analyzed using the two-parameter Weibull distribution.

5.5.2   DC Breakdown Test

The testing procedure for DC breakdown was executed in a manner akin to that of AC breakdown testing following the same standards as explained in section 5.5.1. To evaluate the breakdown strength of the materials, thin polymeric sheets having an average thickness of $260 \pm 10 \, \mu m$ were employed. The process involved the application of a DC voltage, with a step voltage of 2 kV being administered every 20 seconds, until the sample failed. Each sample was subjected to three breakdown tests, and in total, 15 tests were conducted on each material type.

5.6 Summary

In summary, this chapter describes the experimental techniques employed to initiate and observe the acoustic propagation characteristics in different polymers. Further, it also provides insights into the procedures and techniques adopted in physical, chemical, and electrical characterizations of these materials.

Chapter 6

Chemical and Thermal Characterization

6.1 Introduction

To investigate the electrical properties of the polymeric rods used in this study, thin polymeric sheets were prepared for each material, following the procedure outlined in chapter 5. The preparation of these thin polymeric films presented two main challenges:

- Due to the lack of information from the supplier regarding the melting temperature of the PU rods, it was necessary to conduct thermal characterization on the PU rods with varying levels of hardness to explore their thermal behaviour. This characterization was carried out to avoid any potential issues that may arise from the rods melting under high temperatures during the preparation of thin films for the dielectric testing of these materials. In contrast, PP and Nylon were obtained from a different supplier and the supplier readily provided the thermal information for Nylon and PP, which allowed for a more straightforward assessment of their thermal characteristics.

- The inner chemical structure of a material plays an important role in determining its suitability for various applications. The chemical structure of the materials significantly influences the dielectric properties of the material and its response towards the pressure acoustic pulse. Therefore, Fourier Transform Infrared (FTIR) analysis was

employed to explore the chemical composition of the materials used in this study.

- Moreover, the process of melting small pieces of polymeric rods under the hydraulic press had the potential to bring about changes in the chemical and physical structure of these materials. It was of utmost importance to ensure that the melting process did not adversely affect the chemical and physical properties of the polymeric materials. To address this concern, FTIR spectroscopy was employed for verification purposes as well. This technique allowed for a detailed characterization of the molecular structure of the polymeric materials, thereby enabling the verification of any changes that may have occurred during the melting process.

Consequently, two characterization techniques were utilized to address these concerns. Firstly, to investigate the thermal behaviour of the PU rods with different levels of hardness, DSC was performed. Secondly, to ensure that the chemical and physical compositions of the materials remained unchanged after the melting process, the FTIR was conducted before and after the melting of the materials.

Therefore, this chapter present the results and discussion of the characterizations; FTIR spectroscopy on PP, Nylon, and PU with varying level of hardness and the DSC measurements for the PU variants are also presented in this chapter.

6.2 Results and Discussion

6.2.1   Differential Scanning Calorimetry (DSC)

DSC is a thermal analysis technique used to measure differences in heat flow between a specimen and reference material while the specimen undergoes controlled heating. The calorimeter measures the heat content entering or leaving the sample, and both the sample and reference are maintained at a common temperature during the experiment. DSC analysis typically employs a linear temperature program for the sample holder, and only a small amount of material (few mg) is required. Due to its speed and simplicity, DSC is the most commonly used thermal technique. It provides both quantitative and qualitative information about physical and chemical changes, including endothermic and exothermic processes and variations in sample heat capacity [138].

While performing the DSC, to maintain equal temperatures between the sample and reference during physical transformations (e.g., phase transitions), different amounts of heat may be required compared to an empty sample pan or the reference sample. The heat needed depends on the nature of the transformation process, whether it is exothermic or endothermic. For example, when a solid sample changes to a liquid state, more heat is required to increase its temperature due to the absorption of heat during the phase transition. Conversely, during exothermic processes like crystallization, less heat is needed to raise the sample's temperature. By analysing the heat flow differences between the reference and sample, DSC can accurately determine the amount of heat released or absorbed during these transition processes [139].

Therefore, the materials were subjected to DSC measurement to explore the thermal characteristics of the PU with varying levels of hardness. The DSC results are shown below in Figure 6.1. In PU40, two distinct glass transition temperatures were observed at 55.10°C and 127.46°C. The first temperature signifies the transition of the soft segment of PU40, while the latter represents the transition of the hard segment within PU40. This behaviour was also noticed in PU70.A distinct process is observed in PU90 at 178°C which is associated with the melting of hard segment. A similar behaviour in the process was also observed in PU40 and PU70 at 178°C but the change was very small as compared to PU90. This phenomenon can be explained by the relatively lower proportion of hard segments present in PU40 and PU70.
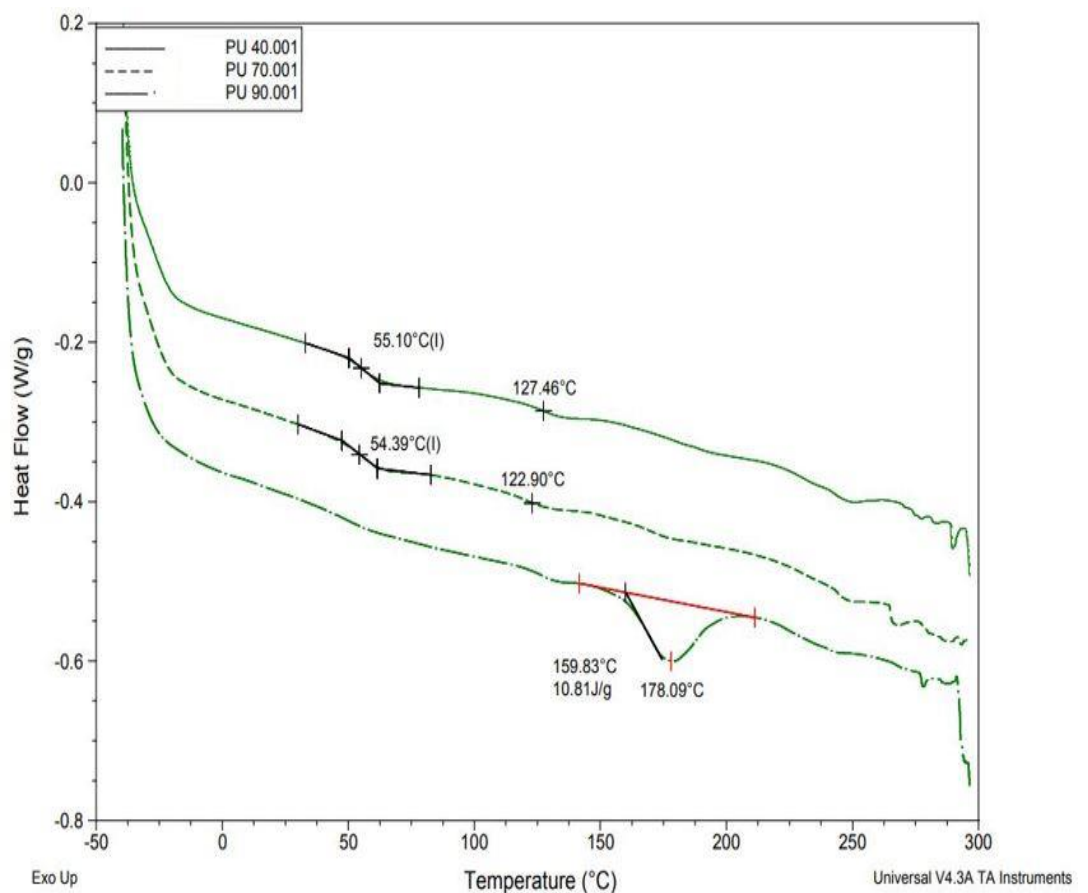
Figure 6.1: DSC measurement of PU40, PU70, and PU90.

6.2.2 Fourier Transform Infrared Spectroscopy (FTIR)

FTIR spectroscopy is a technique that allows us to obtain an infrared spectrum of various types of materials, including solids, liquids, and gases. FTIR is particularly valuable for identifying specific types of chemical bonds, which are known as functional groups. When using FTIR, data about a material's interaction with infrared light are simultaneously collected across a broad range of wavelengths. Since the absorption of light at particular wavelengths corresponds to specific chemical bonds, it becomes possible to determine the types of chemical bonds present in a sample by analysing the infrared absorption spectrum. This means that by interpreting the pattern of absorption in the spectrum, we can identify the functional groups and chemical bonds within a specimen. In practical applications, when dealing with commonly encountered substances, an unknown sample's spectrum can be matched against libraries of spectra from known compounds to identify and characterize the material.

Furthermore, when dealing with the process of melting polymeric materials under the hydraulic press, it is important to note that this method not only supplies heat for melting but also exerts substantial pressure on the material. Consequently, the procedure for creating thin films from polymeric materials through hot pressing carries the potential to induce changes in the chemical and physical characteristics of the material. To ensure that this hot-pressing procedure, aimed at melting and forming thin sheets of the polymer, does not negatively impact the material's chemical and physical characteristics, FTIR spectroscopy was employed. Initially, FTIR analysis was conducted on small pieces of the polymeric materials prior to their exposure to the hydraulic press. Additionally, FTIR spectroscopy was applied to the resulting thin polymer sheets.

The FTIR spectra of all three types of PU before and after the melting process is shown in Figures from 6.2 to 6.5. The spectral peak at 3336 cm^{-1} corresponds to NH stretching, while the peak at 2959 cm^{-1} is associated with -CH2 stretching. Further, hydrogen bonding between the secondary amine group (–NH) and the carbonyl group (C = O) is the intrinsic driving force for the phase separation of PUs, which is important for the self-healing performance [140]. The hydrogen bonding interaction makes the carbonyl bond length elongated and results in the reduction of the stretching vibration frequency [141]. Hence, mathematical deconvolution of the carbonyl stretch peaks around 1729 cm^{-1} and 1704 cm^{-1} can be used to divide the free and hydrogen carbonyl [142]. The higher intensities between the wavenumber 1729 cm^{-1} to 1704 cm^{-1} associated with the carbonyl stretch and H-bonded carbonyl in PU70 and PU90 samples indicate a higher concentration or abundance of hard segments in those samples. Conversely, the absence of these peaks in PU40 suggest a lower concentration of hard segments. Further, the peak at 1417 cm^{-1} is associated with -CH2 vibration [21, 22]. The attribution of FTIR spectral peaks are tabulated in Table 6.1. Further, the peaks at 1232 cm^{-1}, 1092 cm^{-1}, and 929 cm^{-1} can be attributed to the presence of the aliphatic ether [23].
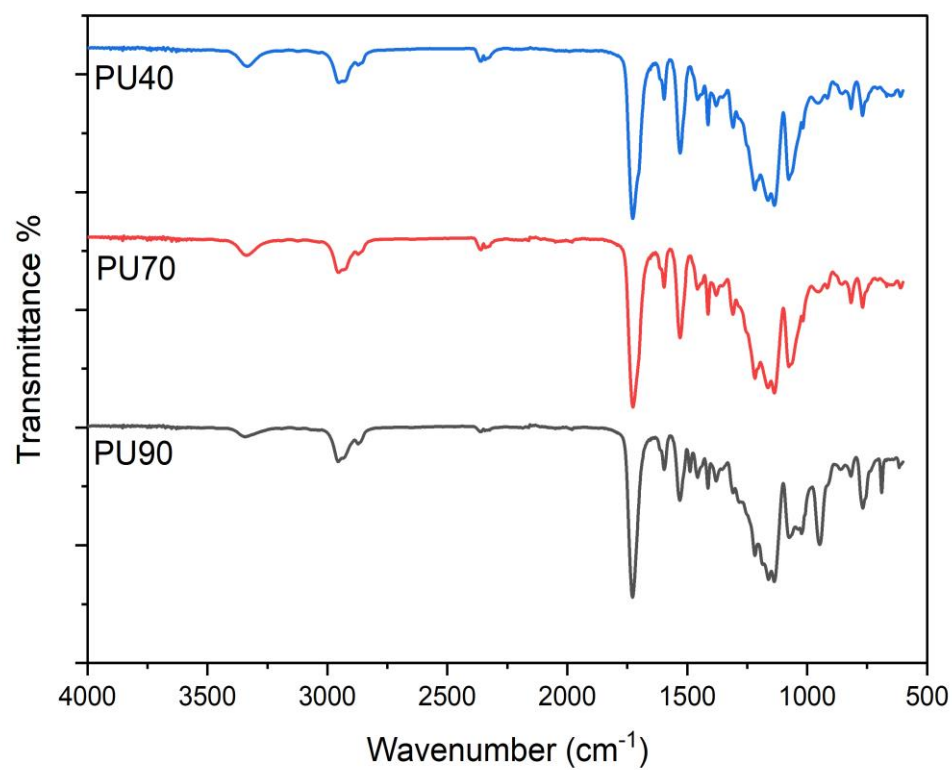
Figure 6.2: FTIR Spectra of the PU variants before melting.
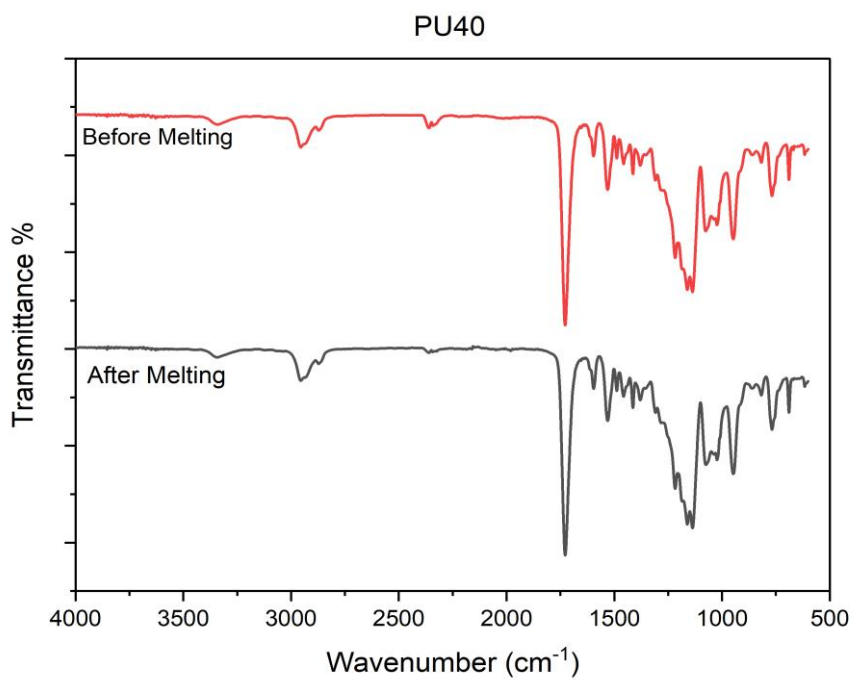
Figure 6.3: FTIR Spectra of the PU40 before and after melting.
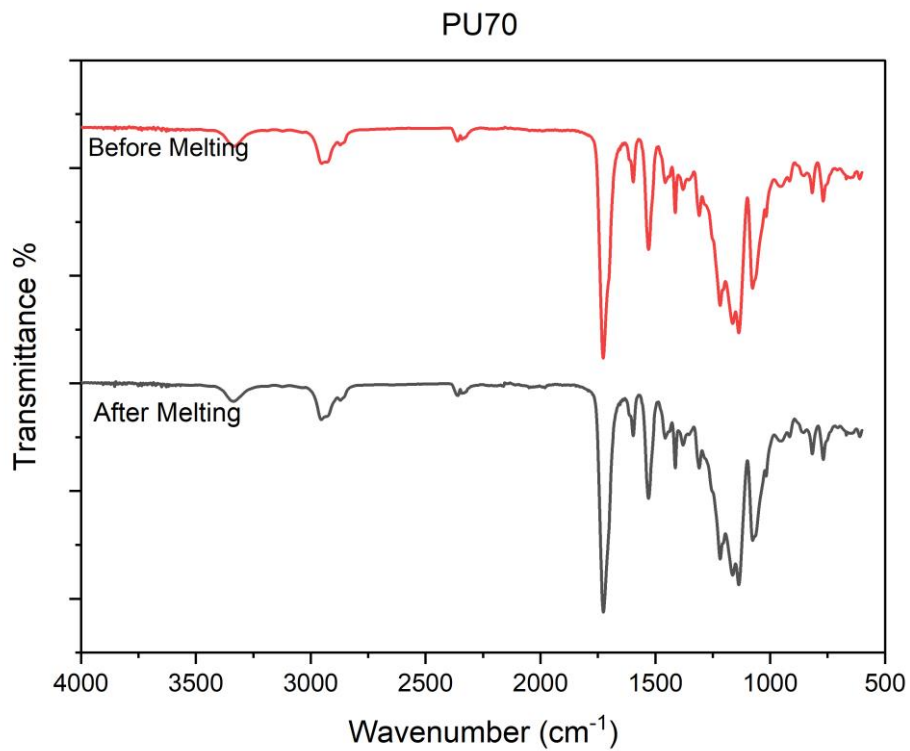
PU70

Figure 6.4: FTIR Spectra of the PU70 before and after melting.
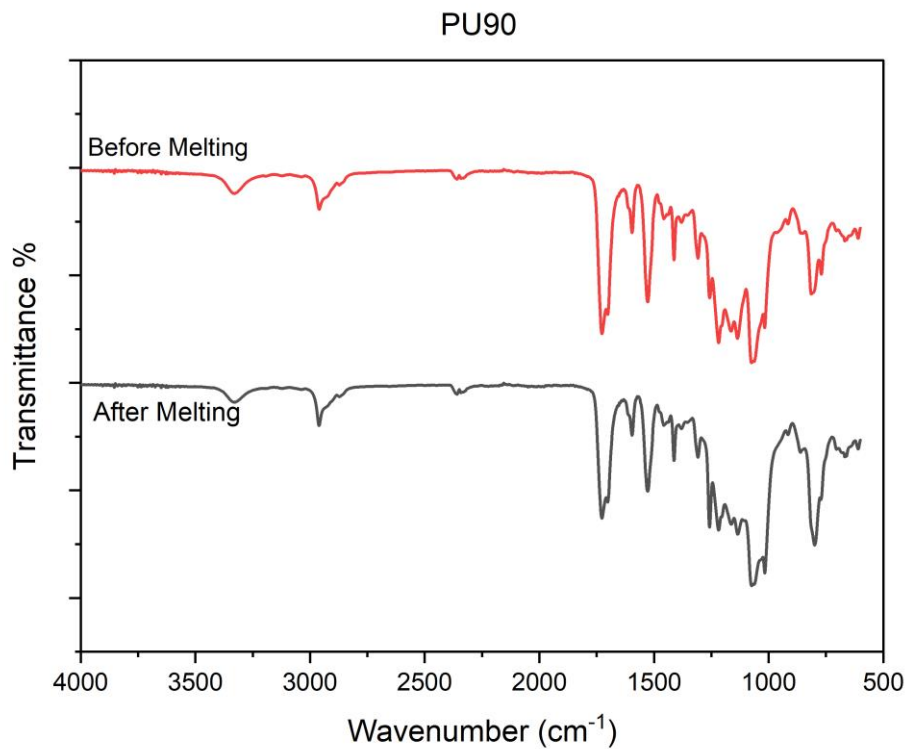
PU90

Figure 6.5: FTIR Spectra of the PU90 before and after melting.

Table 6.1: Peaks attributions of FTIR spectra of PU

Wavenumber (cm⁻¹)	Vibration
3336	N-H Stretching H-bonded
2959	C-H Stretching
1729	O = C Free Carbonyl
1704	HN-O = C H-bonded Carbonyl
1525	C-H Stretch, N-H bend
1417	-CH₂ Vibration
1307	C-N Urethane
1232	Asymmetric N-CO-O, C-H aliphatic Skeleton
1092	C-O-C Aliphatic ether
1017	Symmetric N-CO-O
929	C-O-C Stretch aliphatic ether
866	C-C Skelton vibration
775	C-C Skeleton rocking
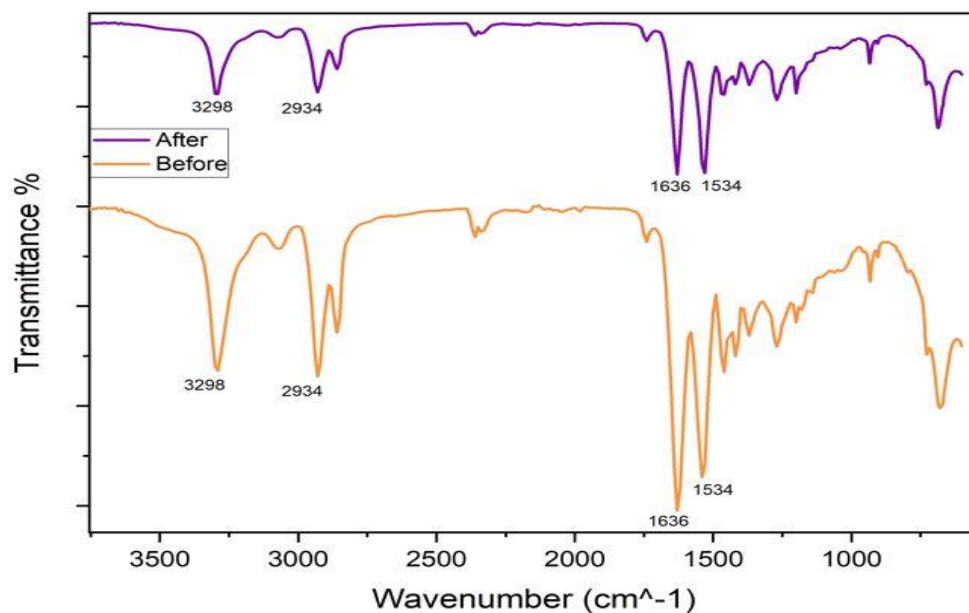
Figure 6.6: FTIR Spectra of Nylon, before and after melting process

Figure 6.6. shows the FTIR spectra of the Nylon, both before and after the melting process. The peak at 3298 cm^{-1} is associate with N-H Stretch H-bonded while 2934 cm^{-1} peak attributed to asymmetric CH_2 stretch. Further, the peak at 1636 cm^{-1} represents C=O stretch and the peak at 1534 cm^{-1} is associated with N-H bend [143]. Moreover, the damping in intensity of the spectral peaks of the Nylon samples was observed after melting similar behaviour which was observed in PU90. This indicates that the melting process affected the physical structure of the material.
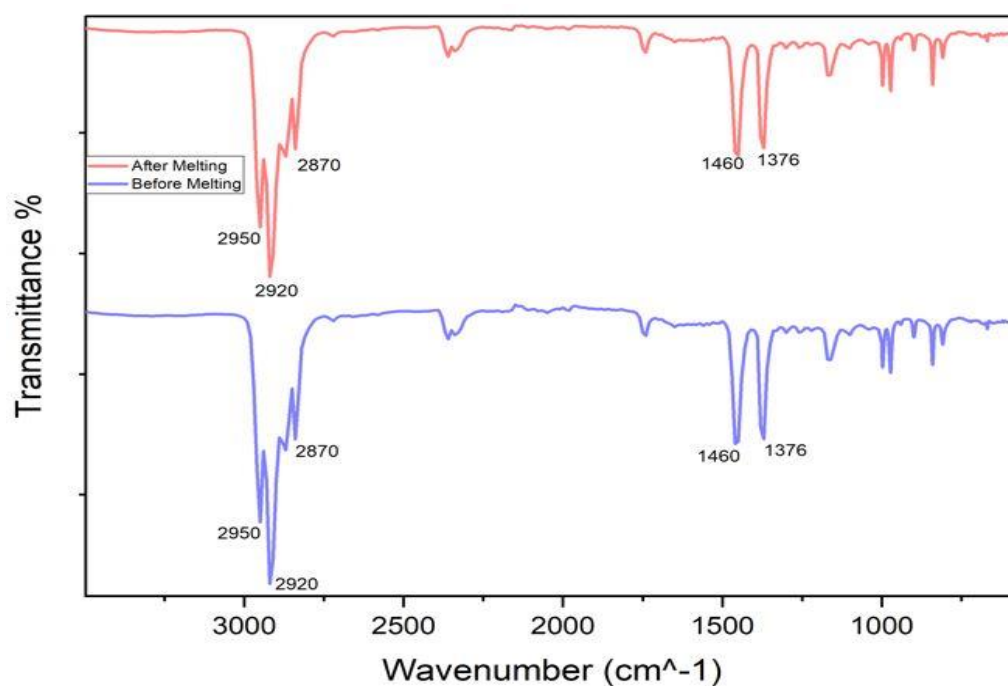
Figure 6.7: FTIR spectra of PP before and after heating.

Similarly, Figure 6.7. Shows the FTIR spectra of PP, both before and after the melting process. Here the spectral peaks at 2950 cm^{-1} and 2920 cm^{-1} represents the asymmetric stretching of CH_3 and CH_2 respectively. While the peak 2870 cm^{-1} is associated with stretching of CH_3 and the peaks 1460 and 1376 cm^{-1} attributed to CH_3 [144].

Moreover, based on the FTIR spectral analysis of all the materials, there was no shift in spectral peaks for all materials before and after melting which implies that melting process didn`t induce any chemical change in the material. Further, a shift in the magnitude of the spectral peaks of the PU90 and Nylon was observed after the melting process. The decrease in magnitude of the spectral peaks in PU90 and Nylon after melting indicates the changes in physical properties of the material due to the melting process which can be either structural or morphological or both [145].

Summary

This chapter focuses on the results of characterizing the materials used in the study. The two main techniques used in the characterization process were FTIR and DSC. DSC, measurement resulted in valuable insights into the thermal properties of the polymeric materials. DSC analysis provided crucial information, such as the melting temperature and glass transition temperature, which helped better understand the materials' behaviour during phase transitions. This deepened understanding of their structural properties, thermal characteristics of each type of PU variant. Further, this information was helpful in selecting the suitable temperature while melting the material under the hydraulic press.

Insights into the chemical composition and physical structure of each material were obtained through FTIR analysis. It was important to conduct the analysis both before and after melting the polymers to determine whether the melting process had any effect on the material's chemical or physical composition. This is crucial to ensure that the material composition and physical composition remains unchanged, which allows for the dielectric characteristics of the material and

acoustic propagation characteristics to be correlated to the material physical and chemical structure.

The FTIR spectra taken both before and after the melting process showed a high level of consistency. The peaks in the spectra remained almost identical, which suggests that the melting process did not cause any significant changes to the chemical composition of the materials. Further, a shift in the intensity of the spectral peaks of the PU90 and Nylon was observed after the melting process. The decrease in intensity of the spectral peaks in PU90 and Nylon after melting indicates the changes in physical properties of the material due to the melting process which can be either structural or morphological or both [145].

Chapter 7

Dielectric Response and DC Conductivity

7.1 Introduction

When a dielectric material is subjected to an external electric field, an internal rearrangement called dielectric displacement occurs within the material. This leads to the material becoming polarized, which can be caused by various mechanisms such as electronic polarization, atomic polarization, and orientational polarization.

- Electronic Polarisation: In every atom or molecule, there is a mechanism that operates universally. When an electric field is applied, the electrons that surround the positively charged atomic nuclei move, creating a dipole moment. This is caused by the displacement of the centre of charge within the atom or molecule.

- Atomic Polarisation: When an electric field is applied, the positioning of atomic nuclei in a molecule or lattice becomes distorted, resulting in polarisation. This type of polarisation occurs at a lower frequency than electronic polarisation, mainly due to the relatively larger mass of atoms as compared to electrons.

- Orientational Polarisation: Also referred to as dipolar polarisation, this occurs in materials containing molecules with inherent dipole moments, such as water molecules. Under the influence of an electric field, these dipole moments align to a certain extent, thus inducing polarisation in the material.

Out of the various mechanisms of polarization, the orientation of molecular dipoles happens at a reduced rate compared to electronic and atomic polarisation [49]. The measurement of orientational polarization immediately after applying an electric field shows a low observed instantaneous relative permittivity. This is due to the lack of time for dipole alignment. However, with enough time after the application of the electric field, maximum orientational polarization can happen. This state represents the highest achievable relative permittivity and is called the static relative permittivity.

For instance, an AC electric field E, with angular frequency ω, and having magnitude, E_o, is applied on a dielectric material:

$$E = E_o \cos(\omega t) \qquad (7.1)$$

This electric field has the potential to induce polarization in the dielectric material. Furthermore, when operating at higher frequencies, the electric field initiates the dielectric displacement, denoted as D which lag the applied field and results in a phase difference δ:

$$D = D_o \cos(\omega t - \delta) \qquad (7.2)$$

Where, D_o is the corresponding displacement. The dielectric displacement can also be written as:

$$D = D_1 \cos(\omega t) + D_2 \sin(\omega t) \qquad (7.3)$$

Where,

$$D_1 = D_o \cos(\delta) \qquad (7.4)$$

$$D_2 = D_o \sin(\delta) \qquad (7.5)$$

As D_o is proportional to E_o and D_o/E_o is a function of angular frequency w, two terms of relative permittivity, i.e., $\varepsilon_r'(\omega)$ and $\varepsilon_r''(\omega)$ can be introduced:

$$\varepsilon_r'(\omega) = \frac{D_1}{\varepsilon_o E_o} \qquad (7.6)$$

$$\varepsilon_r''(\omega) = \frac{D_2}{\varepsilon_o E_o} \qquad (7.7)$$

Where, ε_o is the permittivity of the vacuum. The complex relative permittivity can be written as:

$$\varepsilon_r^*(\omega) = \varepsilon_r'(\omega) - j\varepsilon_r''(\omega) \qquad (7.8)$$

where $\varepsilon_r'(\omega)$ and $\varepsilon_r''(\omega)$ represents real and imaginary parts of the complex relative permittivity. The real part of complex permittivity is also known as lossless permittivity, while the imaginary part of the complex permittivity is associated with dipole relaxation.

The dielectric loss tangent, $\tan \delta$ can be represented as:

$$\tan \delta = \frac{\varepsilon_r''(\omega)}{\varepsilon_r'(\omega)} \qquad (7.9)$$

It is crucial to note that when an electric field is suddenly applied, the polarization process needs a certain amount of time to reach its static relative permittivity from the initial instantaneous state. This occurrence is commonly referred to as dielectric relaxation.

7.2 Results and Discussion

7.2.1   Real Relative Permittivity

In analysing the real relative permittivity ε_r results as a function of frequency, different trends emerged for each material that shed light on the intricate electrical properties of the materials under study. The real relative permittivity, as previously defined, is a fundamental factor characterizing the material's response to electric fields. In this context, examining its variation with frequency provides an understanding of how the materials interact with alternating electric fields across different spectral ranges. Figures 7.1 depict the frequency-dependent behaviour of each PU variant's real relative permittivity while figure 7.2 shows the frequency dependent behaviour of Nylon and PP.
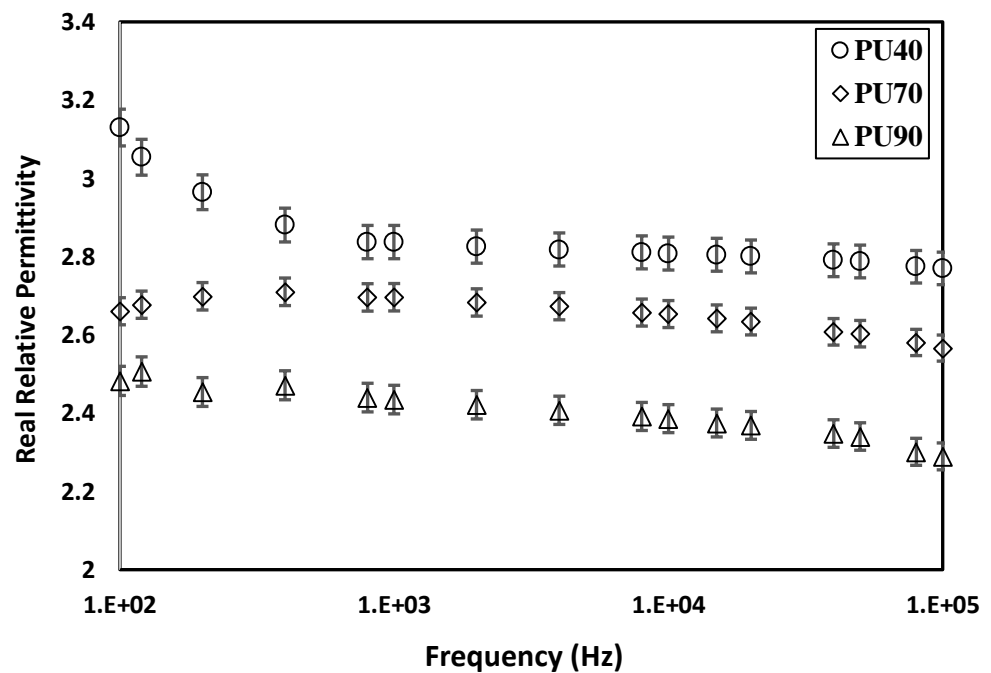
Figure 7.1: Real relative Permittivity of PU variants at different frequencies. The error bars represent the percentage variation 1.5% in minima and maxima of the measured values.

The dielectric response of PU40 initially exhibits a higher real relative permittivity, which subsequently decreases with increasing frequency, eventually stabilizing at higher frequencies. This behaviour suggests that dipole polarization is more pronounced at lower frequencies due to the extended time available for dipoles to polarize. Conversely, at higher frequencies, the limited time available for polarization leads to a reduction in real relative permittivity. In contrast, PU70 and PU90 start with lower initial relative permittivity compared to PU40. Initially, their relative permittivity increases before declining again at higher frequencies, resulting in a flat response. This different behaviour of PU70 and PU90 as compared to PU40 can be attributed to the higher crystallinity of the PU70 and PU90, which impedes polarization initially.
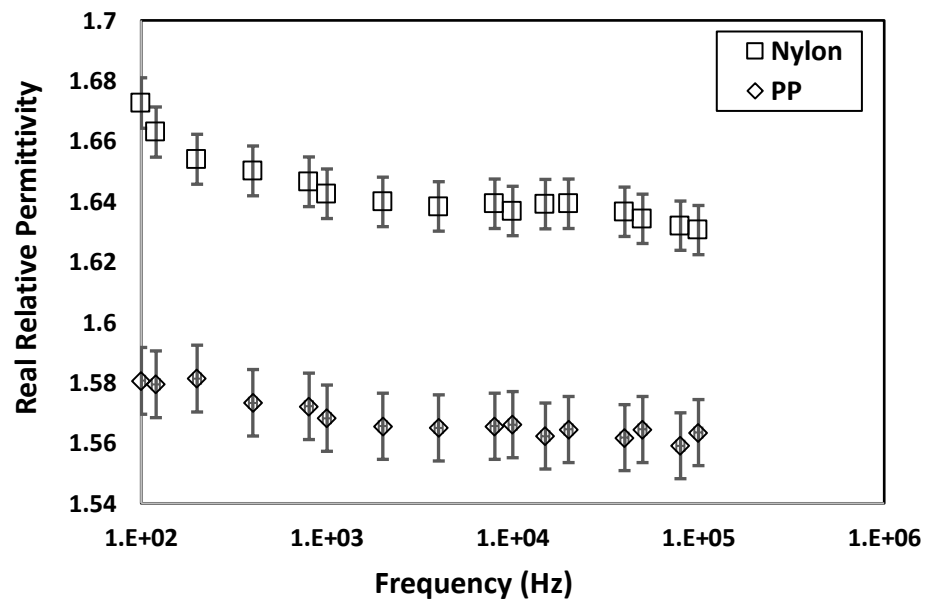
Figure 7.2: Real relative Permittivity of Nylon and PP at different frequencies. The error bars represent the percentage variation in minima and maxima of the measured values.

Moreover, the real relative permittivity behaviour of Nylon was similar to what was observed in PU40 while PP deviates from that of the PU variants. In the case of Nylon, real relative permittivity values are high at lower frequency and decrease with increase in frequency and stabilize at higher frequencies similar to PU40. Conversely, the real relative permittivity of PP portrays a variation in behaviour as compared to the rest of the polymers under observation at all frequencies similar to the behaviour observed in PU70 and PU90 at lower frequencies where a fluctuation was observed in real relative permittivity at lower frequency. like in PU70 and PU0, this fluctuation in the real relative permittivity of the PP can be attributed to the crystallinity of the material.

7.2.2   Dielectric Loss Tangent

Figures 7.3 and 7.4 depict the dielectric loss tangent results for the PU variants, Nylon, and PP. These observations provide the insights into the electrical behaviour of these materials.

Furthermore, it is important to note the trend of the dielectric loss tangent with frequency. Initially, at lower frequencies, PU70 exhibits the highest dielectric loss tangent values, while PU90 demonstrates the lowest. However, as frequency increases, the trend becomes more variable. Notably, the dielectric loss tangent values for PU90 surpass those of PU40. Moreover, with further increases in frequency, all PU variants display higher dielectric loss tangent values compared to their lower frequency counterparts and PU90 shows the highest loss tangent while PU40 shows the lowest values among the PU variants. This means that more energy is being lost at higher frequencies, possibly due to factors like molecular motion, interfacial polarization, or other dynamic processes within the materials.
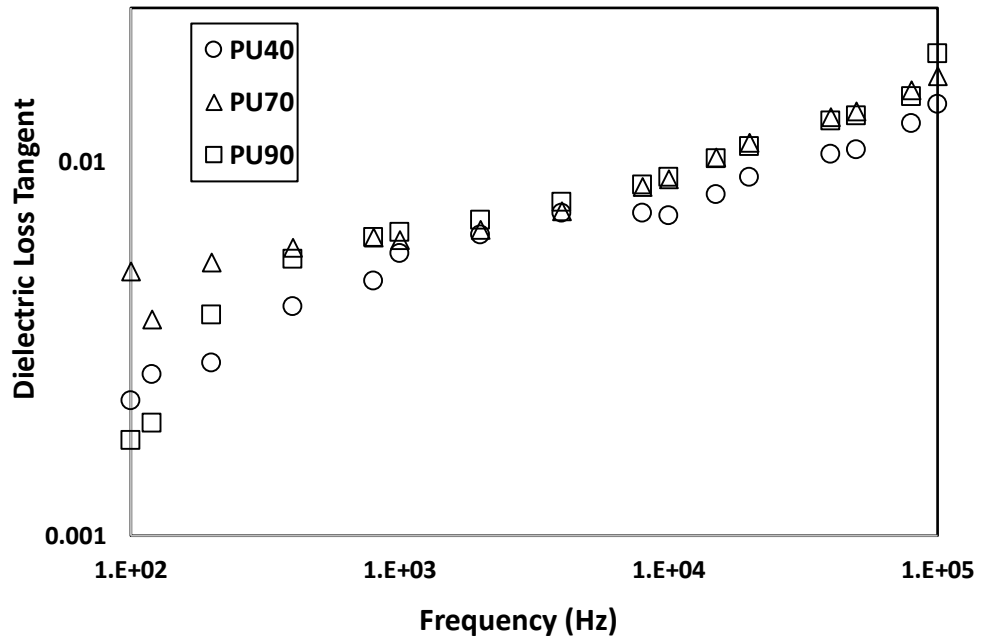
Figure 7.3:Dielectric Loss Tangent of PU variants at different frequencies.

One important feature worth noting is the consistently low dielectric loss tangent values displayed by all materials. This indicates that the energy dissipation in the PU samples is minimal, meaning these materials have excellent dielectric properties with very little energy loss, resulting in efficient electrical performance.
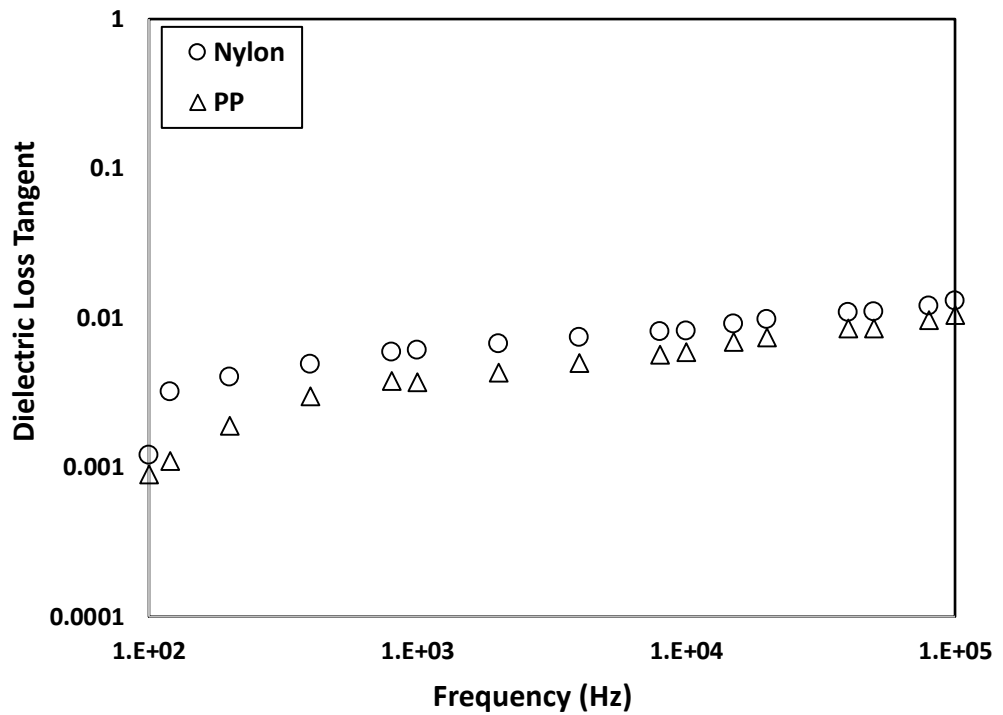
Figure 7.4: Dielectric Loss Tangent of Nylon and PP at different frequencies.

When it comes to "Nylon and PP," there's a clear pattern that emerges. The dielectric loss tangent values for these materials start off low, but gradually increase as the frequency increases. This pattern is like what was seen in the PU variants. The increase in dielectric loss tangent with frequency of the applied electric field indicates the energy loss during the relaxation process.

7.2.3   DC Conductivity

DC conductivity is a fundamental electrical property that measures a material's ability to conduct electric current when subjected to a constant electric field. It provides insights into how effectively charges (usually electrons) can move through a material in response to an applied voltage. When an electric field is applied to a material, free charges within the material experience a force and begin to move. These charges can be electrons (in conductive materials) or charge

123

carriers created by defects or impurities (in semiconductors or insulators). The movement of charges constitutes an electric current. Measurement of DC conductivity is essential for assessing the electrical performance of any polymeric materials. DC conductivity is influenced by several material properties:

- Carrier Mobility: The ability of charges to move through the material is determined by their mobility. Materials with high carrier mobility generally exhibit higher conductivity.

- Carrier Density: The concentration of charge carriers affects conductivity. More charge carriers lead to higher conductivity.

- Temperature: Temperature impacts the thermal energy of carriers, influencing their mobility. Conductivity often increases with temperature due to enhanced carrier mobility.

- Microstructure and Defects: Crystal defects, impurities, and grain boundaries can influence charge carrier movement and, consequently, conductivity.

Ten samples of each material were tested to analyse the DC conductivity. Figure 7.5 provides the individual DC conductivity values of ten samples of all the PU variants at various voltage levels. Further, Table 7.1 shows the average DC conductivity of each material with standard deviation in the measured DC conductivity in each PU variant.
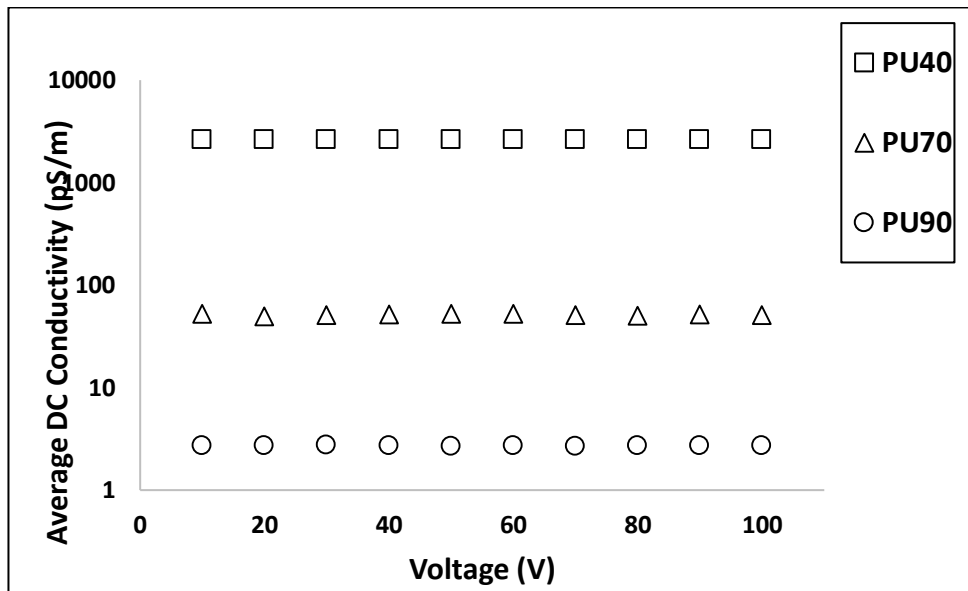
Figure 7.5: DC conductivity of PU variants at different voltages.

Table 7.1: Average DC conductivity of ten samples of the PU variants

Material	Average DC Conductivity	Standard Deviation
PU40	2.6 nS/m	0.001 nS/m
PU70	51.4 pS/m	0.097 pS/m
PU90	2.7 pS/m	0.002 pS/m
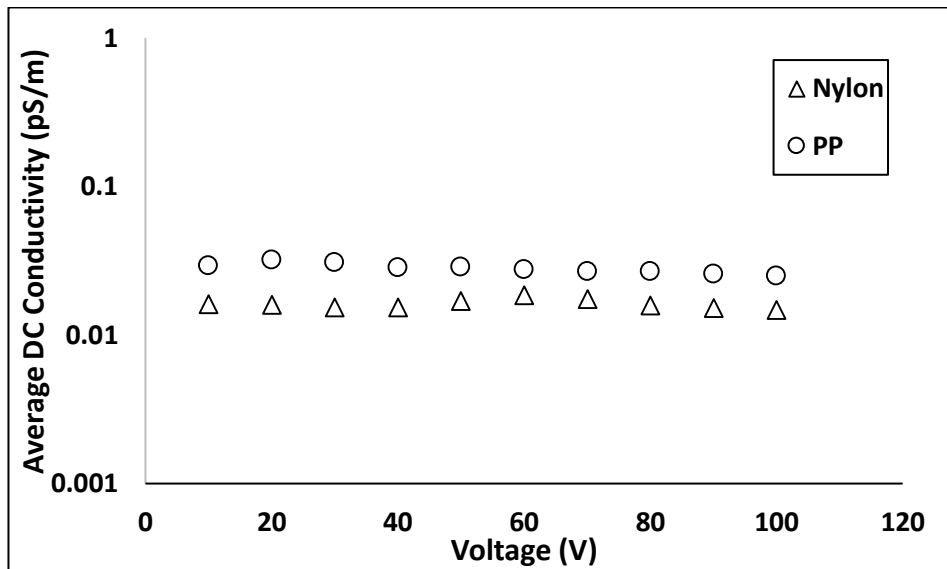
Figure 7.6: DC conductivity of Nylon and PP at different voltages.

Table 7.2: Average DC conductivity of ten samples PP and Nylon

Material	Average DC Conductivity	Standard Deviation
Nylon	0.04 pS/m	0.0012 pS/m
PP	0.03 pS/m	0.0022 pS/m

Moreover, Figure 7.6 and Table 7.2, depicts the DC conductivity patterns exhibited by Nylon and PP. A notable revelation is that Nylon and PP stand out with the lowest conductivity values among all the polymeric materials used in this study. This disparity highlights the diverse electrical behaviour exhibited by different polymers, with Nylon demonstrating notably constrained charge transport capabilities compared to other materials.

7.3 Discussion

The observed trend in the real relative permittivity ε_r results, where values are higher at lower frequencies and decrease with increasing frequency before

126

stabilising into a flat line at higher frequencies, can be explained by considering the mechanisms of polarisation and the material's response to electric fields. At lower frequencies, the time available for polarization processes to occur is relatively longer. As a result, the material's internal dipoles have sufficient time to orient themselves in response to the applied electric field. This increased alignment of dipoles leads to higher polarization and, consequently higher values of real relative permittivity. The polarisation effect dominates the material's response at these lower frequencies. As the frequency of the applied electric field increases, the time available for polarization decreases. This can hinder the full alignment of dipoles within the material, leading to a reduction in polarization and a subsequent decrease in the real relative permittivity values. Moreover, higher frequencies limit the extent to which dipoles can reorient. This restriction results in a saturation of the polarization response. Dipoles are not able to align significantly within the short time frame of the rapidly changing electric field. Consequently, the material's polarization and its corresponding impact on the real relative permittivity reach a minimum, causing the permittivity values to stabilize and follow a flat line.

DC conductivity analysis showcases the behaviour of PU across different voltage levels. A noticeable trend emerges where the DC conductivity of the PU decreases as the hardness of the PU increases. Further, the DC conductivity of PU40 is 50 times greater than that of PU70 and the conductivity of the PU70 is 25 times greater than the conductivity of PU90 as shown in Table 1. The decrease in DC conductivity of PU with the increase in hardness of the PU is attributed to the internal structure of the PU. As the hardness of PU is regulated by adjusting the proportion of hard segments therefore, the increase in hardness of PU indicates the presence of the more hard segments and significant interactions between them. These effectively act as

crosslinks and reduce the mobility of the polymer chains, therefore, reduce the mobility of charge carriers ultimately resulting in lower DC conductivity. The observed relationship between material hardness and DC conductivity highlights the importance of material selection and understanding the electrical behaviour of PU variants in high voltage applications.

Further, the graph in Figure 7.1 depicts the relationship between frequency and real relative permittivity for all PU variants. Analysing the dielectric spectra, a common trend emerges among the PU variants, the change in real relative permittivity of the PU variants is high at lower frequencies especially for PU40. The Increase in the measured real relative permittivity at low frequencies have been attributed to electrode polarization effects associated with conductivity. In liquid systems an expression in the form of:

$$\varepsilon'_{meas} = \varepsilon' + \frac{\sigma^2 C_0}{\omega^2 \varepsilon_0^2 C_E}$$

has been used to relate the measured real relative permittivity (ε'_{meas}) to the physical permittivity ε', where σ is the conductivity, while C_0 is the geometrical capacitance and C_E is the capacitance associated with the interface between the electrode and the liquid [146]. The similar behaviours are observed with increase in the measured real relative permittivity occurring at low frequencies when conductivity allows the movement of ionic charge within the polymers [147].

7.4 Summary

- The real relative permittivity of the PU variants is high at lower frequencies and decreases as the frequency increases. Moreover, a

noticeable correlation between material hardness and real relative permittivity indicates that harder PU materials exhibit lower real relative permittivity values.

- The dielectric loss tangent is low at lower frequencies and increases as the frequency is increased. This low dielectric loss tangent implies minimal energy loss within the materials when subjected to the electric field, indicating their potential for efficient electrical insulation applications.

- The DC conductivity of the PU decreases as the hardness of the PU increases. This suggests that the hardness of PU influences the electrical conduction characteristics. The observed relationship between material hardness and DC conductivity highlights the importance of material selection and understanding the electrical behaviour of different PU variants in high voltage applications.

The DC conductivity results of PU variants hold significance for industries and engineers, particularly in evaluating PU's suitability as an insulating material. Materials with lower DC conductivity are favourable for applications in high-voltage cables. The findings provide valuable insights for engineers seeking a balance between PU hardness and its self-healing capability, aiding in optimal material selection for specific requirements.

Chapter 8

Investigation of Electrical Breakdown Strength

8.1 Introduction

The breakdown strength of electrical insulation is an important topic in dielectric studies, both in academia and practical applications. This metric refers to the ability of insulation materials to withstand voltage stresses before breaking down, indicating the point at which their integrity is compromised. In simpler terms, electrical breakdown strength refers to the measure of an insulating material's capacity to resist voltage-induced stress without deterioration. This means that once the resistance of the material is overpowered by an applied voltage, it will result in the material's degradation and ultimately lead to its rupture due to an electric discharge passing through the insulation. Therefore, the higher the electrical breakdown strength of an insulating material, the more capable it is in withstanding voltage-induced stress without decomposing.

The breakdown strength of electrical materials is commonly expressed in terms of voltage per unit thickness, denoted as kV mm^{-1}. This is significantly influenced by various external factors, such as thermal, electrical, mechanical, and chemical parameters [148, 149]. The intrinsic strength of a material, which is theoretically pure and free from defects, cannot be practically achieved due to the presence of defects. However, thin samples exhibit a lower likelihood of defects. Despite numerous theoretical proposals on breakdown mechanisms, identifying the precise breakdown mechanism still poses a challenge.

8.2 Statistical Approach

Generally, the dielectric breakdown properties of a solid insulation system can be analysed using the two-parameter Weibull distribution. This probability distribution, also known as the extreme-value distribution, was introduced by Weibull in 1951 [150] and is commonly used to study data obtained from time-to-breakdown tests or voltage endurance tests on solid electrical insulation systems undergoing constant stress or progressive stress. The two-parameter Weibull cumulative function for the failure distribution can be represented as.

$$P(E_i) = 1 - \exp[-\left(\frac{E_i}{\alpha}\right)^{\beta}] \qquad (8.1)$$

Here, $P(E_i)$ is the cumulative probability of failure at a certain experimental breakdown strength. While (E_i), is the experimental breakdown strength. While α and β are the scale and shape parameters respectively. The probability of failure $P(E_i)$ is zero at $E_i = 0$. The probability of failure increases continuously as E increases, and finally approaches certainty, that is, $P(E_i) = 1$. The scale parameter, α represents the breakdown strength at the cumulative failure probability of 63.2 %. The units of α are the same as E_i. The shape parameter, β represents a measure of the spread of the breakdown data. The larger the β, the smaller is the range of the experimental breakdown strength values [151].

When plotting the Weibull distribution on probability graph paper, it's important to use a non-linear cumulative probability of failure scale on one axis and indicate the breakdown strength on the other axis. This allows data from the two-parameter Weibull distribution to follow a straight line. To plot the data, it should be ordered from smallest to largest and a cumulative probability of failure, $P(E_i)$ needs to be

assigned to each point. The Maximum Likelihood Estimation (MLE) technique is used to fit a best straight line through the points, providing better estimates for alpha and beta. In this study, SigmaXL was used for analysis and the breakdown data were plotted between two-sided 90% confidence bounds, graphically representing the spread in the data.

The median rank method was used to estimate the cumulative failure probability $P(E_i)$

$$P(E_i) = \frac{i - 0.3}{m + 0.4} \qquad (8.2)$$

Where the variable m represent the total number of tests conducted on the group of samples while i is the progressive order of failure tests. The aforementioned methodology has been proven to be effective in accurately determining the likelihood of cumulative failure. Furthermore, it aligns with the commonly used MLE approach for computing purposes [152]. Moreover, the symmetrical cumulative distribution function method, where:

$$P(E_i) = \frac{i - 0.5}{m} \qquad (8.3)$$

and the mean rank method, where:

$$P(E_i) = \frac{i}{m + 1} \qquad (8.4)$$

8.3 Results and Discussion

The thin samples of each type of polymer were subjected to dielectric breakdown strength analysis. The samples were placed between the spherical plane electrode system. The electrodes were placed in a container filled with the

transformer oil while thin samples were placed between the electrodes. The use of transformer oil helped to mitigate the electric field enhancement. The electrical breakdown testing setup is already explained in chapter 5. The resultant breakdown data was statically analysed to calculate the breakdown strength of the materials. The two parameters Weibull distribution was used to analyse and plot the breakdown data of the samples of each material. The median rank method was used to estimate the cumulative failure probability.

8.3.1 AC breakdown testing

The variation in AC breakdown performance among the different polymers used in this study were analysed using the approach discussed above. Figure 8.1 compares the AC breakdown strength among the PU variants: PU40, PU70, and PU90, while the figure 8.2 compares the AC breakdown strength of Nylon and PP. The AC breakdown strength of PU40 is measured as 19 kV/mm, indicating a lowest breakdown strength among all the polymers tested in this study. Moreover, the value of beta for the PU40 is also the smallest indicating a wider distribution in the data for this polymer. In contrast, the AC breakdown strengths of PU70 and PU90 are found to be relatively close to each other. The difference in hardness between PU70 and PU90 are small as compared to PU40 and PU70. Therefore, a much greater change in the AC dielectric strength occurred in Between PU40 and PU70. Moreover, the AC breakdown strength of the nylon was like that for the PU70 and PU90. Similarly, the AC breakdown strength of PP was highest among all the polymers used in the study which was recorded as 62 kV/mm. In addition, the Shore scale hardness of Nylon lies between 76° to 88° while it is 95° for PP. This suggests that the AC breakdown strength of the materials increases with the

shore hardness of the materials, PP having the highest level of shore hardness resulted the highest AC dielectric breakdown strength among all the polymers used in this study. Meanwhile, the Shore scale hardness of Nylon was close enough to PU70 and PU90, therefore, the AC breakdown strength of Nylon is close to PU70 and PU90. The corresponding Weibull data, detailed in Table 8.1 and Table 8.2, provides additional statistical analysis of the breakdown strength distribution for each PU variants, Nylon and PP respectively.

Table 8.1: Weibull parameters compare the AC breakdown strength of PU40, PU70, and PU90.

Material	α (kV/mm)	β
PU40	19 ± 3	3 ± 1
PU70	36 ± 1	14 ± 6
PU90	39 ± 1	8 ± 3
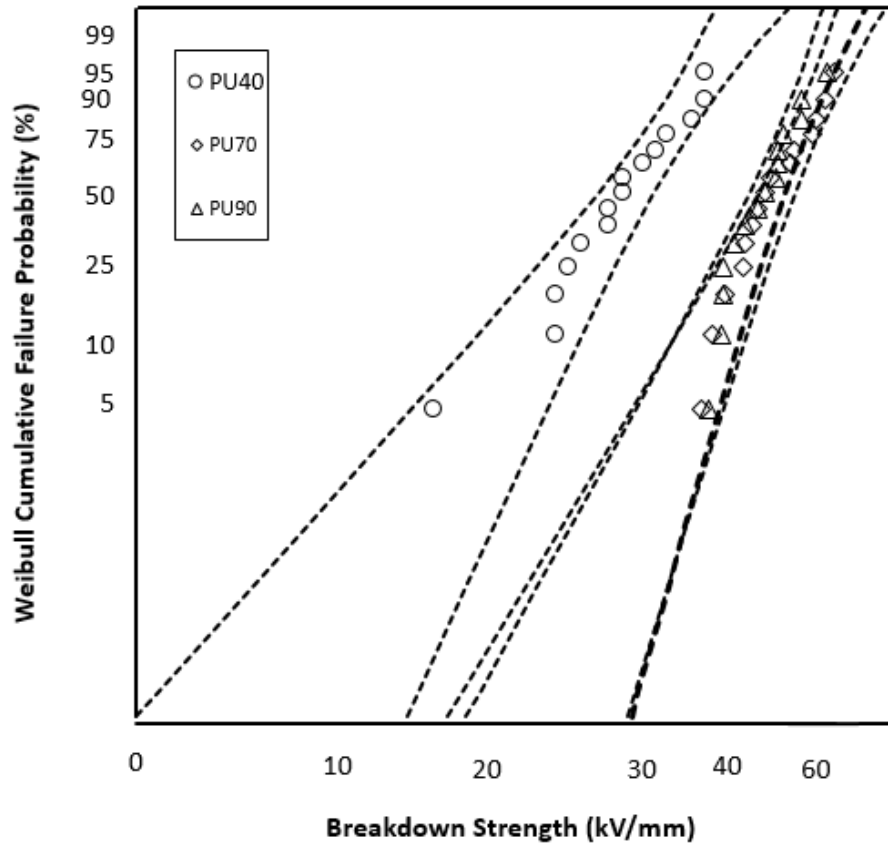
Figure 8.1: Weibull plots comparing the AC breakdown strength of PU40, PU70, and PU90.

Table 8.2: Weibull parameters compare the AC breakdown strength of Nylon and PP

Material	α (kV/mm)	β
Nylon	41 ± 2	10 ± 4
PP	62 ± 7	4 ± 2
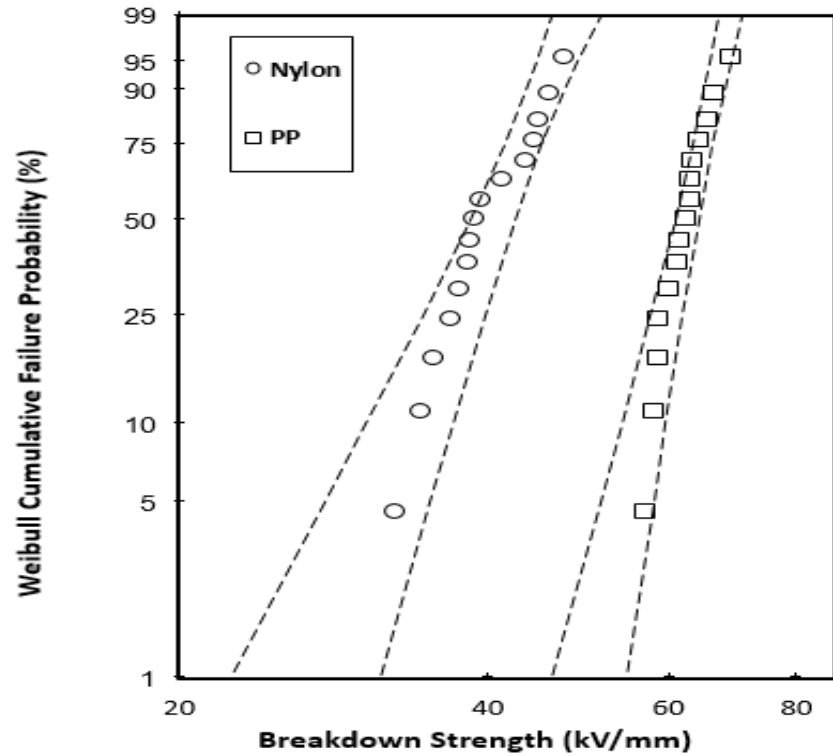
Figure 8.2: Weibull plots comparing the AC breakdown strength of Nylon and

PP.

8.3.2 DC Breakdown Strength

Figure 8.3 represents a comparison of the DC breakdown strength of PU variants: PU40, PU70, and PU90. The measured DC breakdown strength values for these variants were determined as 24 kV/mm, 41 kV/mm, and 56 kV/mm, respectively. Notably, a discernible pattern emerges wherein an increase in the hardness of the PU material correlates with an observable elevation in the DC breakdown strength. This trend establishes a clear relationship between material hardness and DC breakdown strength, underscoring the pivotal role of material characteristics in influencing electrical insulation properties.

The Weibull data is further shown in Table 8.3. The table's statistical analysis of the breakdown strength distribution for each PU variant reinforces the salient connection between hardness and DC breakdown strength.

Table 8.3: Weibull parameters comparing the DC breakdown strength of PU 40, PU 70, and PU90.

Material	α (kV/mm)	β
PU40	24 ± 3	5 ± 2
PU70	41 ± 3	7 ± 3
PU90	56 ± 2	18 ± 7
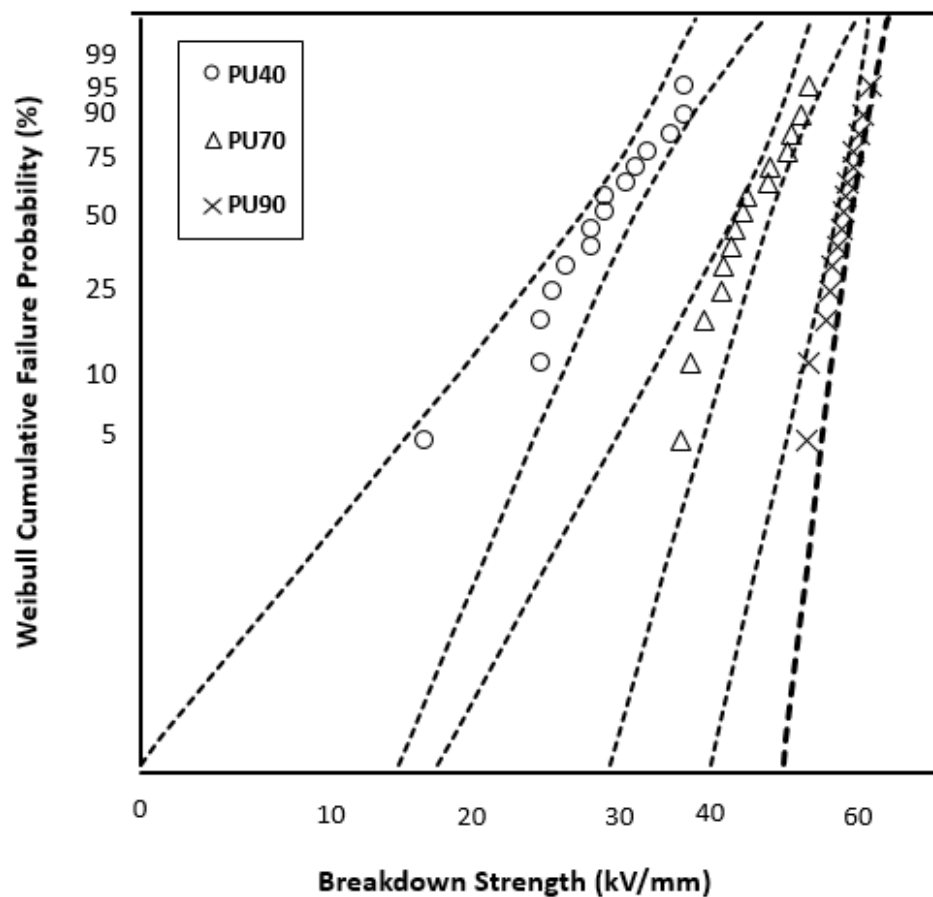
Figure 8.3: Weibull plots comparing the DC breakdown strength of PU40, PU70, and PU90.

138

Furthermore, Figure 8.4 illustrates the Weibull distributed DC breakdown strength of Nylon and PP. The corresponding DC breakdown strength values for Nylon and PP are presented in Table 8.4, with the table offering additional layers of statistical analysis of the DC breakdown strength data.

Table 8.4: Weibull parameters comparing the DC breakdown strength of Nylon and PP

Material	α (kV/mm)	β
Nylon	57 ± 2	13 ± 4
PP	105 ± 5	11 ± 4
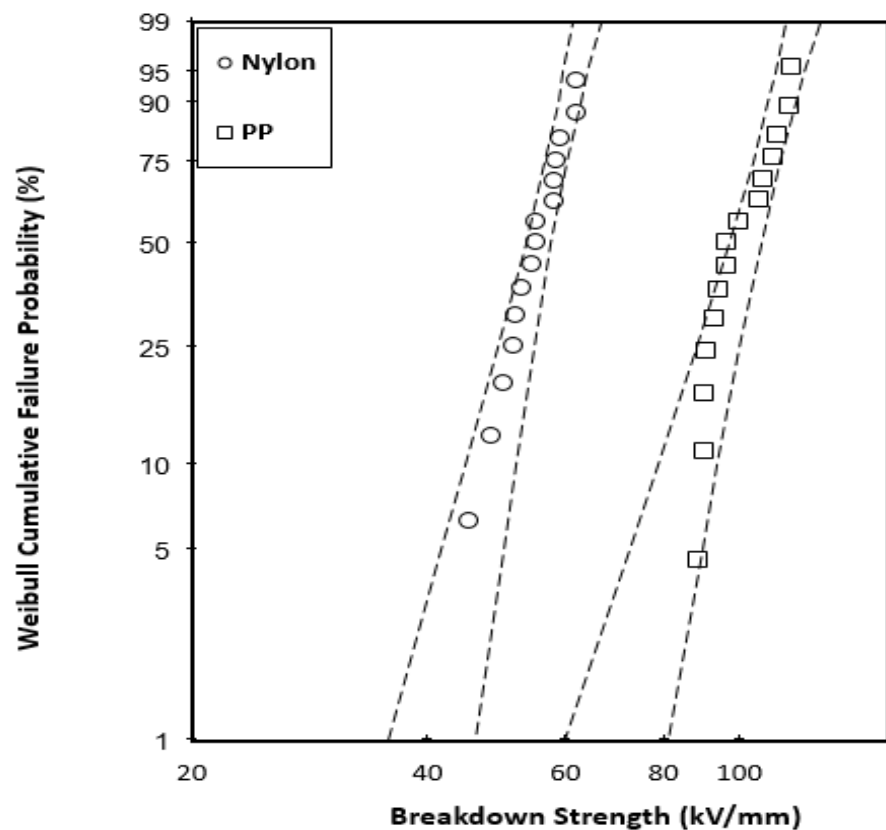
Figure 8.4: Weibull plots comparing the DC breakdown strength of Nylon and PP.

8.4 Discussion

The study investigated on the dielectric breakdown characteristics of polymeric materials used in the research. It was discovered that the breakdown strength of the material increases with its shore hardness. This trend is particularly noticeable in PU variants, indicating that PUs with higher hardness levels can withstand electrical breakdown and display higher strength. During the FTIR analysis of the PU variants in Figure 6.2, a shift in the magnitude of the spectral peaks of the PU90 was observed after the melting process. The decrease in magnitude of the spectral peaks in PU90 after melting indicates the changes in physical properties of the material due to the melting process which can be either structural or morphological or both [145]. These changes in physical properties may disrupt the arrangement of polymer chains, alter the crystallinity of the material, or induce other structural rearrangements. As a result, the dielectric breakdown characteristics of PU90, which depend on factors such as material structure, morphology, and homogeneity, can be affected.
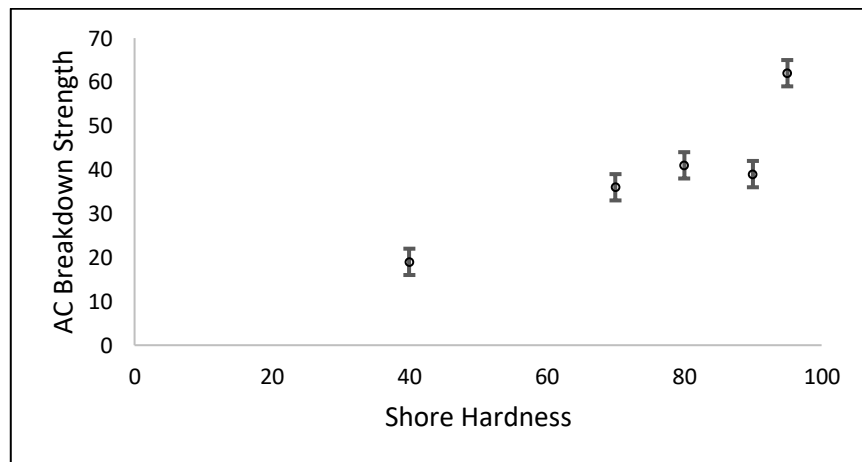
Figure 8.5: Correlation between AC breakdown strength VS Shore hardness of polymeric materials

The underlying reasons behind this correlation between hardness and breakdown strength can be attributed to several factors. PUs with higher hardness levels possesses more hard segments in their composition. This higher concentration of hard segments reduces the mobility of charge carriers and results in higher dielectric breakdown strength. Similarly, Table 4.1, in chapter 4 corelates the shore hardness and tensile strength of the PU. It revealed that the tensile strength of the PU increases with the increase in shore hardness. Moreover, the higher dielectric breakdown strength with increased hard segment hydroxyl-terminated butadiene-acrylonitrile copolymer-based polyurethane elastomers and in other materials has already been reported [153, 154].

The trend becomes even more pronounced when examining the DC breakdown strength as shown in figure 8.6 and 8.7. Interestingly, the DC dielectric breakdown strength data for PU70 and PU90 exhibit distinct spacing, unlike the overlapping Weibull plots observed in the AC breakdown. The following assumptions were made to explain this behaviour. The difference in DC and AC breakdown strength of PU90 as compared to PU70, with higher values observed under positive DC compared to lower values under AC for PU90, can be attributed to the unidirectional nature of the DC stress. Under positive DC conditions, the electrical stress is consistently applied in one direction, leading to specific charge accumulation and polarization effects within the material. This unidirectional stress can result in a higher breakdown strength as compared to the alternating nature of AC, where the reversal of the electric field can influence charge distribution differently. Additionally, the frequency dependence of AC breakdown, coupled with the potential for dielectric loss and heating effects, can contribute to the observed lower breakdown strength under AC conditions. Similar observations

regarding the AC and DC breakdown strength of thin polymeric films has already been observed and reported [16, 155]. Overall, the breakdown strength of PU variants was low as compared to polyethylene and XLPE [16, 156] but, it showed that increased hardness corresponds to higher dielectric strength. This observation prompts further investigation into the synthesis process, specifically focusing on the ratio of hard and soft segments in the material.
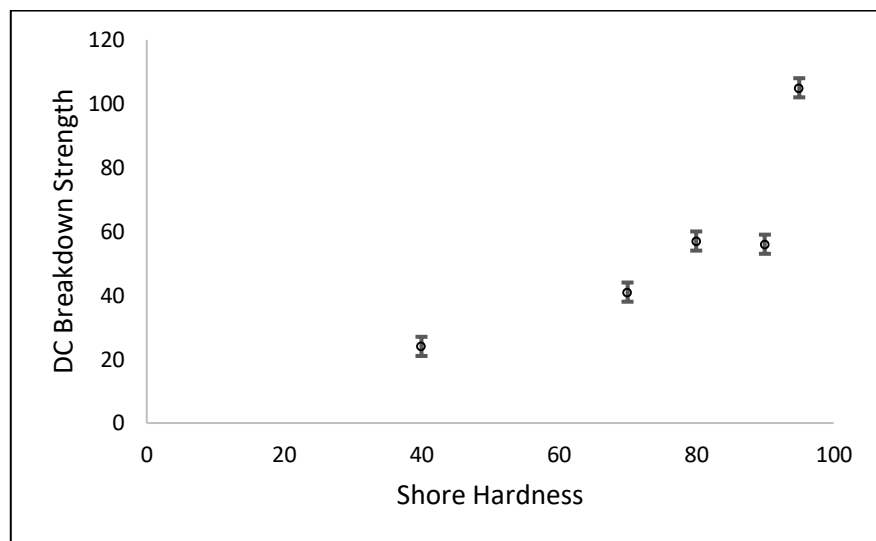
Figure 8.6: Correlation between DC breakdown strength VS Shore hardness of polymeric materials

Moreover, the DC and AC dielectric breakdown strength of Nylon was like the PU90 while the PP had the highest AC and DC breakdown strength among the tested materials as shown in Table 8.2 and Table 8.4. Moreover, the Figure 8.6 shows that the shore hardness of the PP is the highest among all the polymers considered in this study. Therefore, it can be concluded from the above findings that the dielectric breakdown strength of the polymers increases with the hardness of the material which has already been reported as well [154]. These findings are important in selecting the suitable material for the cable insulation.

8.5 Summary

In this chapter, a comprehensive AC and DC breakdown strength analysis was conducted using the Weibull distribution based on experimental data obtained from laboratory experiments. The study encompassed a range of materials including PU40, PU70, PU90, Nylon, and PP.

The findings underscored the distinct electrical performance of the polymers. Notably, PP exhibited the highest AC and DC breakdown strength among all the materials examined. Within the PU variants, a trend emerged where AC breakdown strength tended to be lower while DC breakdown strength exhibited higher values. This distinction became more pronounced with variations in material hardness. Higher material hardness is correlated with enhanced breakdown strength for the PU variants.

Specifically, AC breakdown strength for PU70 and PU90 demonstrated resemblance to that of Nylon. On the other hand, the DC breakdown strength of PU90 surpassed that of PU70, aligning more closely with Nylon's performance.

The DC and AC breakdown results of PU variants indicate that breakdown strength tends to increase with PU hardness, albeit potentially at the expense of self-healing capability. Therefore, the results can help the engineers to optimal material selection for the insulation.

Chapter 9

Propagation of Acoustic Pulse

9.1 Introduction

In on-line partial discharge monitoring, some of the prominent techniques are acoustic detection, detection of current pulses in the system, and ultra-high frequency (UHF) sensing. These methodologies provide insights into the condition of electrical insulation, playing a crucial role in preventing potential failures within power networks. PD events within power cables can indicate insulating material degradation, requiring identification and mitigation to maintain system integrity. Acoustic detection is a non-invasive method that can pinpoint PD sources with accuracy [26, 157].

The effectiveness of detecting acoustic signals depends on transmitting pressure waves triggered by PD incidents in electrical apparatus. Placing sensors on equipment surfaces captures these signals and estimates PD source locations based on the time difference of arrival at multiple sensors. However, this estimation process faces challenges such as noise interference, acoustic scattering, reflections, and computational complexity, as explained in Chapter 5.

This chapter explores how acoustic pulses propagate in polymeric materials initiated from electrical discharge events. It also examines how a material's physical attribute influences these acoustic pulses' propagation. Electrical discharges are initiated through needle-needle electrodes positioned near one end of the rod of each type of polymer used in this study as shown in Figure 5.1 and

Figure 5.2. An acoustic transducer is attached to the opposite end of the rod to monitor the acoustic pulse's propagation through the polymeric materials. The study aimed to uncover how a material's physical properties, exemplified by its hardness, influence the trajectory of acoustic signals. Additionally, the research aimed to discover the potential for utilising this newfound knowledge in detecting and monitoring PD within solid-insulating materials.

9.2 Results and Discussion

The polymeric materials considered for the study were cut into different lengths and subjected to analyse the propagation characteristics of the acoustic pulse. Starting at 10 cm, longer rod lengths were used until the sensor could no longer detect the acoustic signal. The size of each rod used in this study is shown in Table 4.2. An electrical discharge was used to initiate the acoustic signals with needle-needle electrodes. The experimental setup and the procedure to initiate and detect the acoustic signal is explained in chapter 4.

9.2.1 Voltage and Current

To initiate an acoustic signal, a discharge event was created. The 100-pF capacitor was charged, creating a voltage difference between the needle-needle electrodes. Once the capacitor was fully charged, the switch was closed to connect the charged capacitor with the electrode system. The air gap between the electrodes breaks down, resulting in an electrical discharge. These electrical phenomena were monitored and recorded using an oscilloscope, visualising the voltage and current dynamics during the breakdown process.

The recordings captured by the oscilloscope provide insights into the temporal evolution of the discharge event. They reveal the electrostatic energy supplied in the system that leads to the breakdown of the air gap. Figure 9.1 illustrate the voltage and current pulse at the time when the discharge event occurred between the needle-needle electrode topology. In the displayed voltage waveform, the persistence of non-zero voltage following the discharge event can be attributed to the residual charge remaining in the capacitor at the time of waveform recording. Similarly, when the discharge event occurs, there is a surge of current as charge flows between the electrodes which causes the current waveform to rise sharply. The current waveform decreases as the discharge event progresses and eventually become negative. These negative current values represent transient responses within the circuit due to the discharge event.
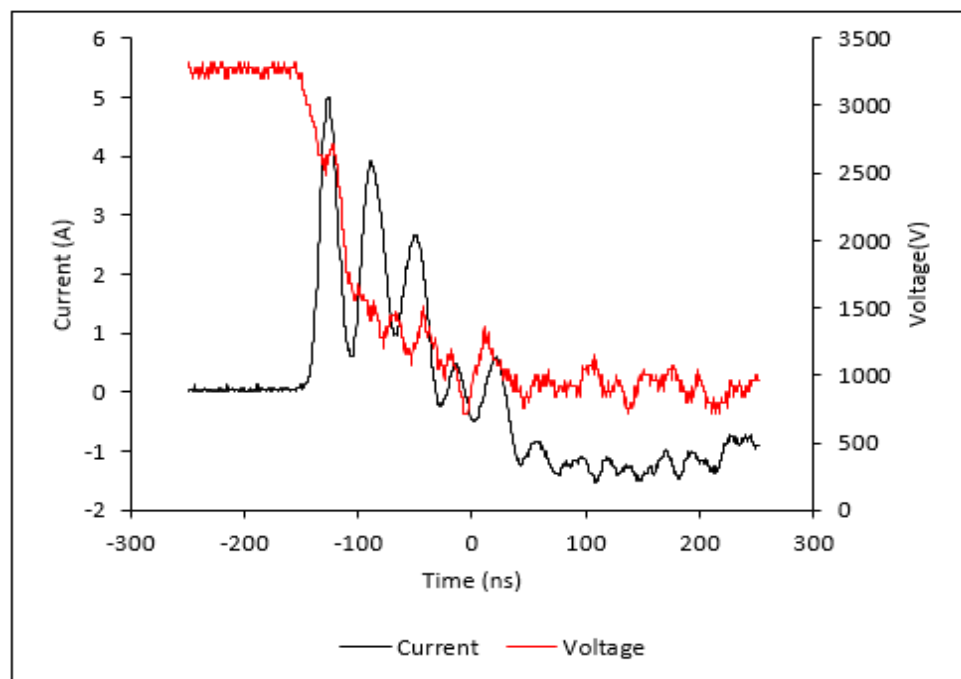
Figure 9.1: Voltage impulse across the needle gap and Current Impulse after gap breakdown

147

Moreover, the consistency of acoustic pulse initiation from electrical discharge events was analysed recording both current and voltage impulses during the discharge events, the energy and power supplied for multiple occurrences were analytically calculated. Figures 9.2 and 9.3 present the resultant data for ten discharge events, revealing consistent levels of power and energy across various discharge events. This consistency reflects the reliability of acoustic pulse initiation from electrical discharges, a critical factor for accurately studying the propagation characteristics of these pulses within polymers. Further, Figure 9.2 and Figure 9.3 show that two of the events were initiated at an earlier time. This is because the capacitor was not fully discharged before reapplied to initiate another breakdown event. That residual voltage in the capacitor helped the capacitor to reach the certain level of voltage which is enough to break the air gap between the electrodes prompting earlier breakdown. These findings not only enhance the credibility of the study's outcomes but also contribute significantly to the understanding of polymer properties and applications.
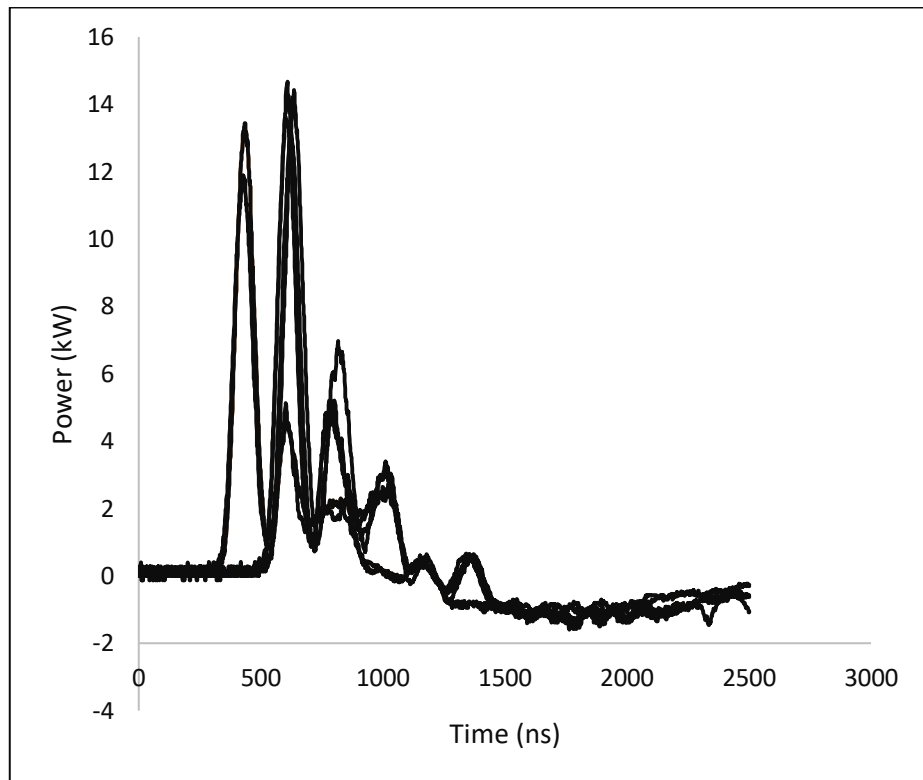
Figure 9.2: Power supplied by multiple the discharge events to initiate the
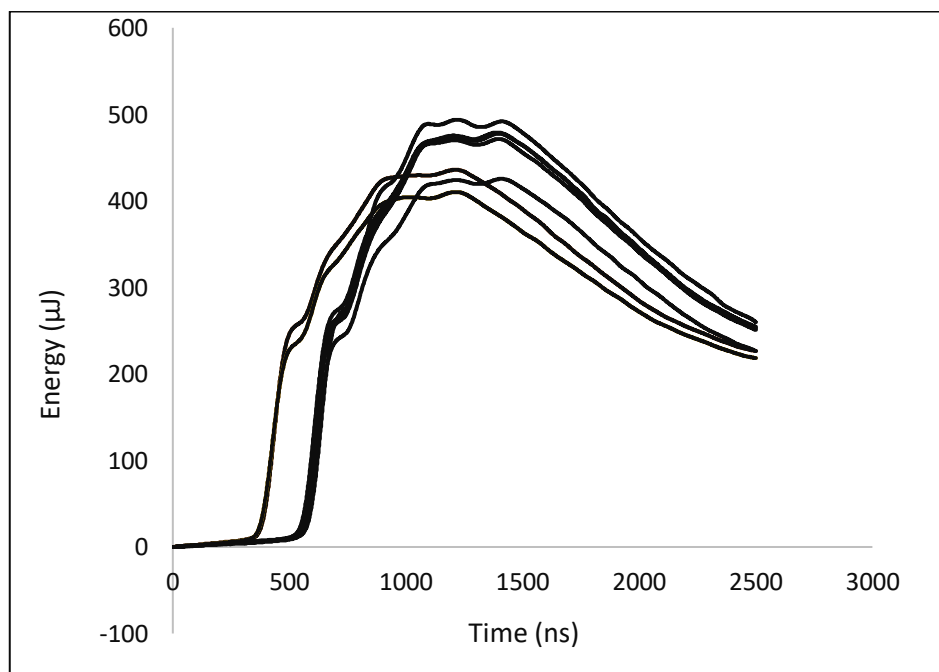
acoustic pulse.

Figure 9.3: Energy supplied by the multiple discharge events to initiate the

acoustic pulse.

9.2.2 Acoustic Signals

The propagating acoustic signals were observed and recorded using an oscilloscope. After recording the propagating acoustic signal from a discharge event, the sensor was intentionally physically disconnected and reconnected before each subsequent discharge event. This was repeated ten times at each rod length. To analyse the consistency and any variation in measurement, the minimum and maximum values obtained from each of the 10 recorded signals at every data point were considered and plotted to evaluate the data's variability. The figure 9.4 shows the plots for the minimum and maximum values of the recorded signals in PU40 at 60cm. Furthermore, the standard deviation of the recorded signals is plotted in Figure 9.5, reinforcing the consistency observed in the recording of the acoustic signal, offering assurance regarding the reliability of the data collected. Overall, this approach helped to ensure the robustness and validity of the experimental findings.
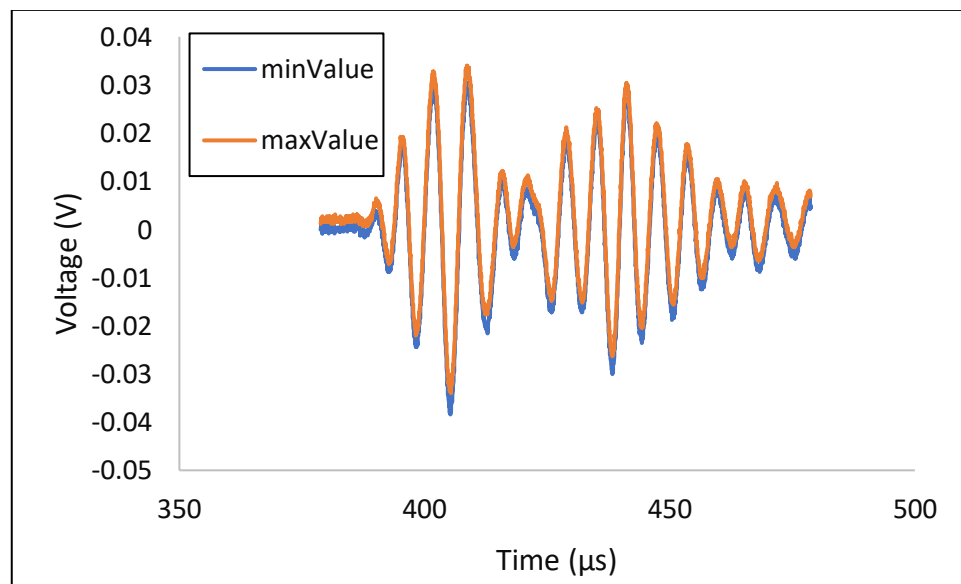
Figure 9.4: Voltage waveforms with the lowest and highest peak values of the recorded signals for PU40 at 60cm.
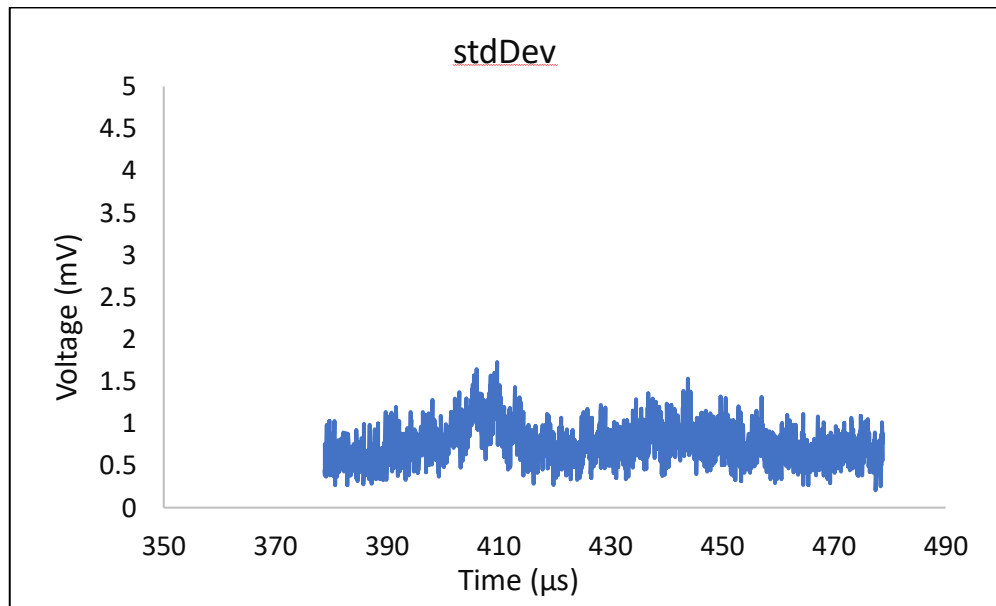
Figure 9.5: Standard deviation in ten signals recorded for PU40 at 60cm.

In Figure 4.3 (Chapter 4), a graphical representation of the R15I-AST sensor's standard response is presented, illustrating how the sensor's output signal behaves in response to varying acoustic signals. The calibration of the sensor to allow meaningful pressure signals to be calculated has been described in chapter 4. Therefore, these recorded signals were converted into pressure units for further analysis.

9.2.2.1   Acoustic signal propagation in PU40

The acoustic signal emitted from an electrical discharge propagate through air before striking the surface of the polymeric rods. After striking the surface of the polymeric rods, it propagates through the polymer. The R15I-AST sensor was used to detect the acoustic signal and then recorded on the oscilloscope as discussed in chapter 4. Figure 9.6 shows propagating acoustic signal detected for various lengths of PU40 rods. Initially, the acoustic signal initiate from the discharge event and travels towards the polymeric rod, where it encounters the surface of the

polymeric rod. Here, due to impedance mismatching, a portion of the signal undergoes reflection, subsequently striking the electrode setup from where it is again being reflected and strike with the polymeric rod and propagate through the rod. This reflected signal is detected along with the primary signal by the sensor and can be observed as a delayed peak in the figures below.
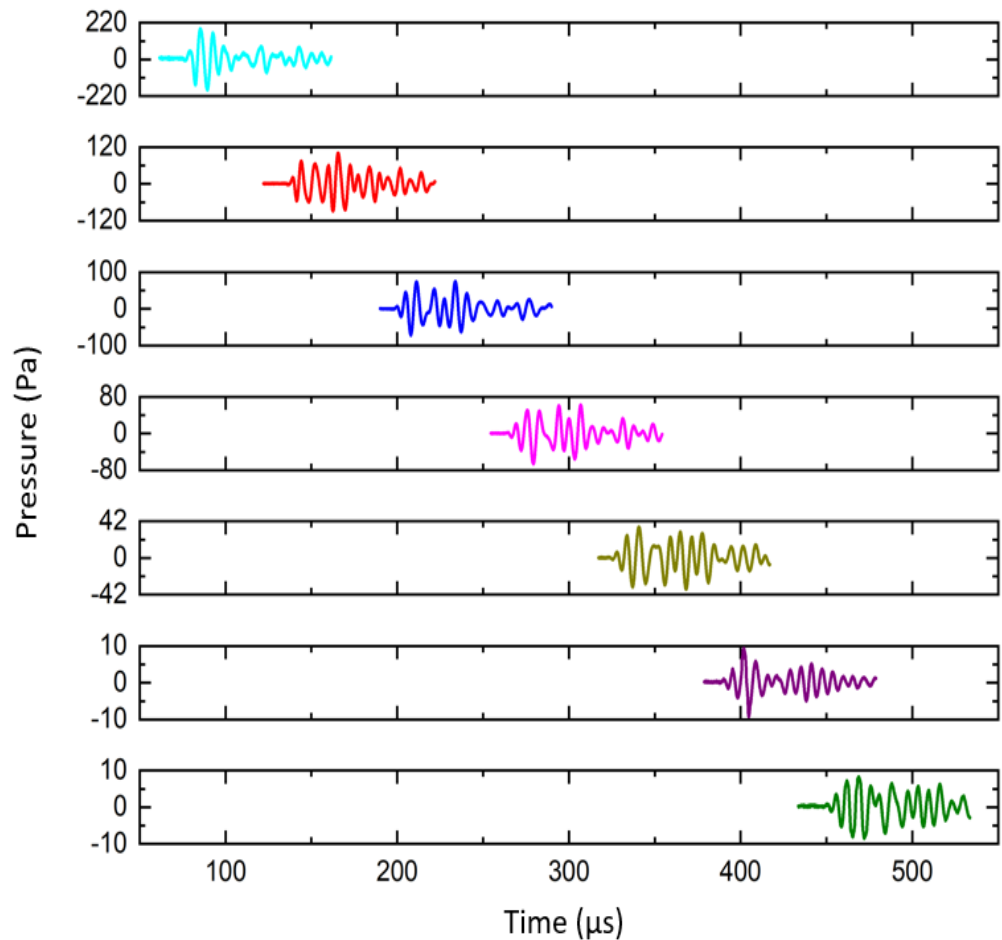
Figure 9.6: Propagation of acoustic signals in PU40 from top 10 cm to bottom 70 cm with an increment of 10 cm.

9.2.2.2 Acoustic signal propagation in PU70

The propagation of acoustic signal in PU70 was observed at different lengths. Figure 9.7 shows the acoustic signals propagating through the PU70 rods. The

acoustic signal in PU70 was detectable for rod lengths up to 50cm unlike PU40 which showed a higher propagation capability. Additionally, a wider time window was employed to observe both the primary signal and its reflections. Notably, at 20cm or higher lengths of the rod, Figure 9.7 displays two distinct peaks, with the second peak corresponding to the first set of reflected signals. Furthermore, the elongated tail end of the signals in Figure 9.7 indicates that while the initial reflected pulses possess discernible magnitudes, subsequent reflections exhibit significantly reduced magnitudes, ultimately resulting in a flattened signal profile.
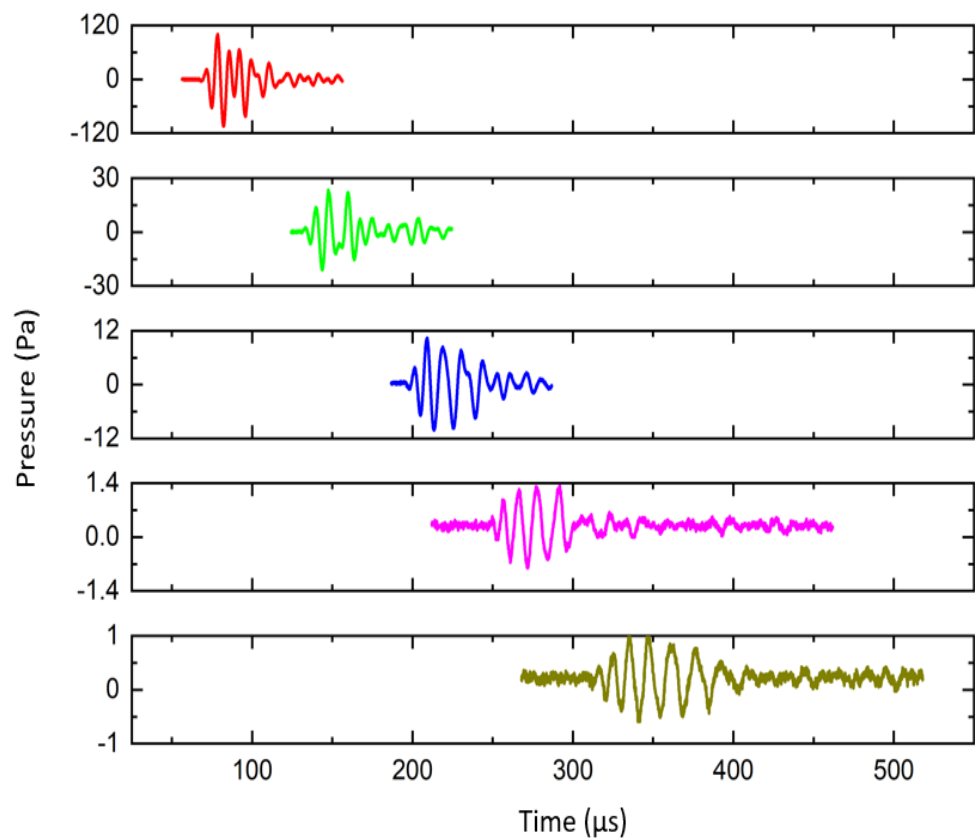
Figure 9.7: Propagation of acoustic signal in PU70 from top 10 cm to bottom 50 cm with an increment of 10 cm.

9.2.2.3   Acoustic signal propagation in PU90

The visual representation presented in Figure 9.8 provides insight into the propagation of acoustic signals within different lengths of PU90 rods. At 10cm, a shorter time window was selected on the scope to observe the acoustic signal which resulted in a signal with a single distinct peak along with oscillations of lower magnitude. However, when the time window was increased multiple peaks of the acoustic signal which represent the reflected signals were recorded on the scope which can be seen in the Figure 9.8. Moreover, the propagation capability of acoustic signal further reduced as the hardness of the PU increased.
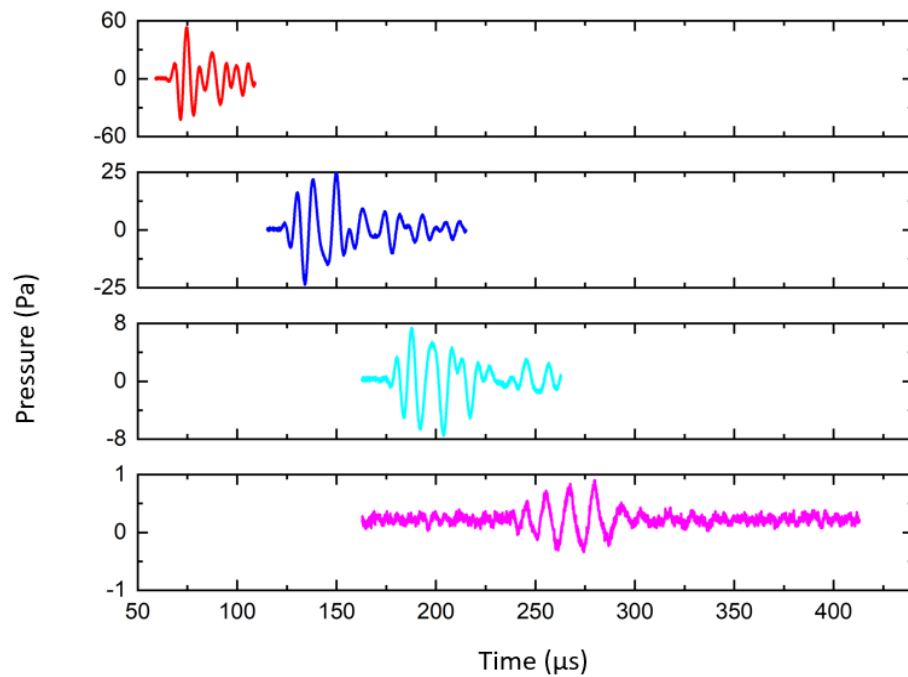
Figure 9.8: Propagation of acoustic signal in PU90 from top 10 cm to bottom 40 cm with an increment of 10 cm.

154

9.2.2.4 Acoustic signal propagation in Nylon

Apart from the PU family, the propagation characteristics of the acoustic signal were observed in other polymeric materials. Acoustic signals propagated in Nylon for a longer distance than the PU materials. It was observed that the acoustic signal was detectable up to 80cm in Nylon. The acoustic signals propagating through the Nylon detected at different lengths are shown in Figure 9.9. Moreover, the multiple peaks of the acoustic signal detected in Nylon, correspond to the subsequently reflected acoustic signal.
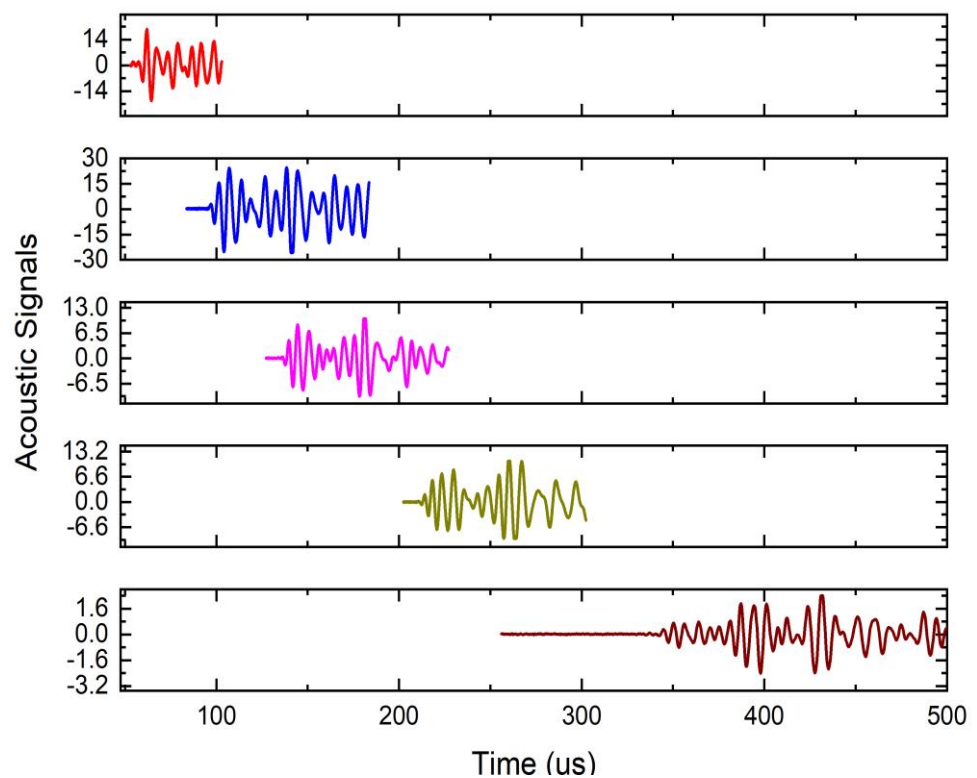
Figure 9.9: Propagation of acoustic signals in Nylon from top 10cm, 20cm, 30cm, 50cm, and 80cm.

9.2.2.5   Acoustic signal propagation in PP

The propagation of acoustic signal in PP was observed and is displayed in figure 9.10. The acoustic signal in PP was only detectable in rod lengths up to 30 cm. The presence of multiple peaks in the detected acoustic signals indicates the occurrence of reflected acoustic signals. It's noteworthy that the magnitude of these reflected signals is approximately one third of the magnitude of the original acoustic signal. Additionally, the acoustic signal exhibited minimal propagation capability compared to other materials investigated in this study. This diminished propagation capability led to a higher rate of decay in the magnitude of the propagating acoustic signal.
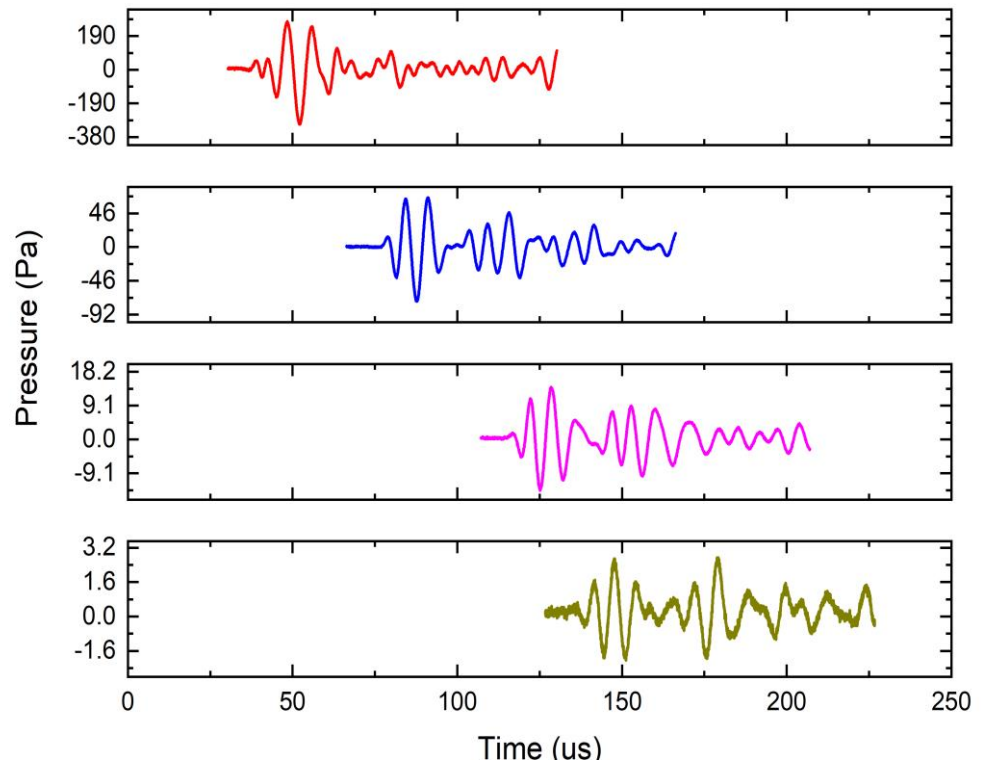
Figure 9.10: Propagation of acoustic signal in PP from top 10 cm, 20cm, 25 cm to bottom 30 cm.

9.2.3 Drop in Acoustic Peak Magnitude of Propagating Signal

To understand the effects of the material's physical characteristics on the propagating acoustic signal, it is necessary to quantify the impact of damping for each type of material. A thorough investigation was conducted to analyse how the peak magnitude of the acoustic propagating signal decreased as the length of the rod increased. The damping in the peak magnitude of the acoustic signal behaviour in each type of PU was plotted separately in Figure 9.11, while Figure 9.12 shows the behaviour of the peak magnitude of the propagating acoustic signal in Nylon and PP.

The behaviour of the peak acoustic signal was found to follow an exponential behaviour with distance.

$$P_{peak}(x) = P_0 e^{-\alpha_p x} \qquad (9.1)$$

Here P_0 represent the pressure at the surface of the rod transmitted into the rod while $P_{peak}(x)$ represent the peak value of the pressure at x distance away from the surface of the rod which in this case is represented as the rod lengths in cm. Moreover, the recorded data for the signals at each length of the rod was used to analyse the peak pressure and subsequently used to calculate the attenuation coefficient of peak pressure α_p of the acoustic signal as it propagates through the rods by finding the curve of best fit accompanied by the 95% confidence interval.
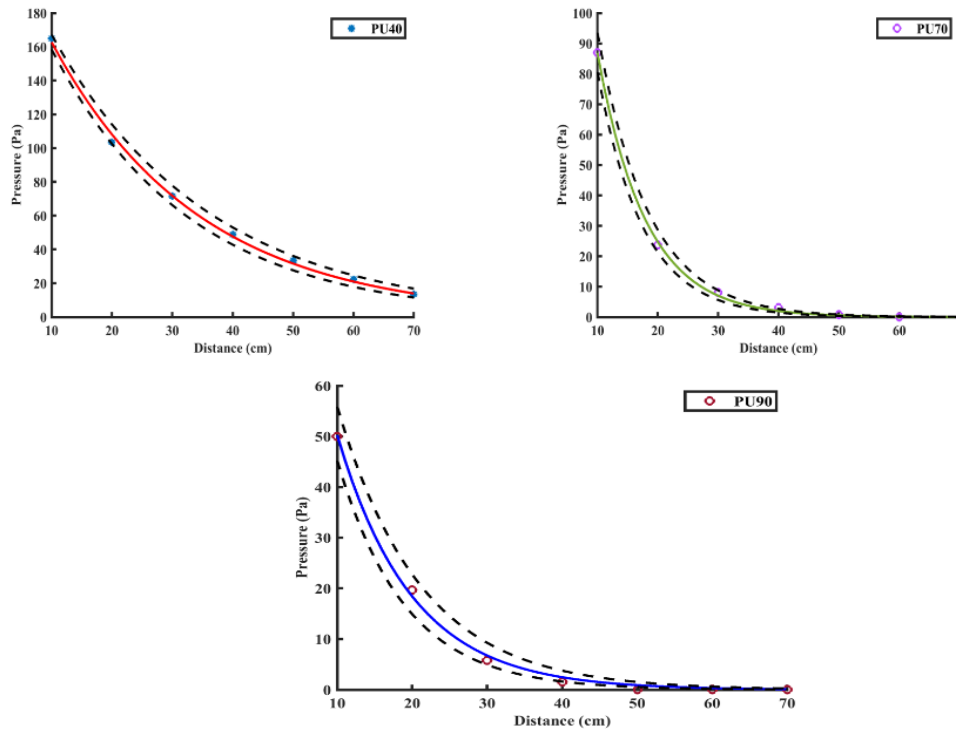
Figure 9.11: The magnitude of peak acoustic signal as a function of distance in each type of PU with exponential curve fit along with 95% confidence interval (dashed lines).
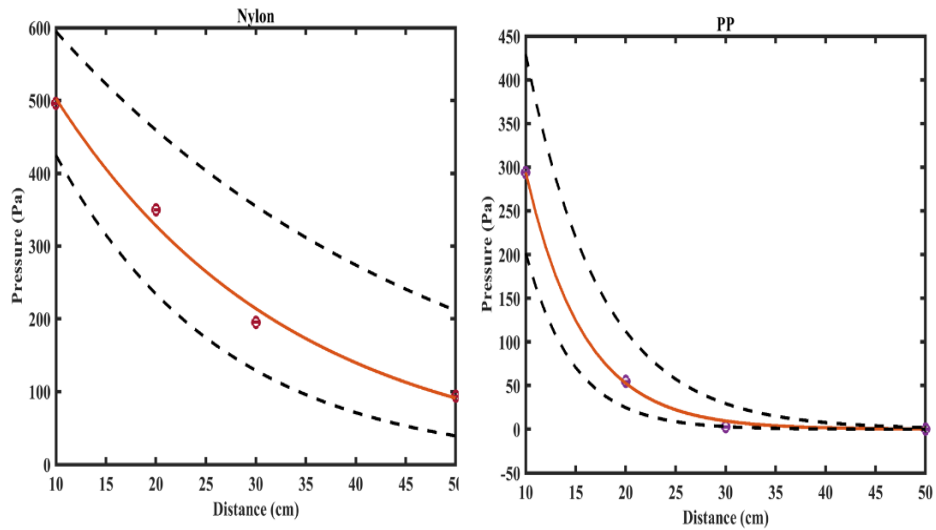
Figure 9.12: The magnitude of peak acoustic signal as a function of distance in Nylon and PP with exponential curve fit along with 95% confidence interval (dashed lines).

Table 9.1 shows the attenuation coefficient of peak pressure of the propagating acoustic signals in different materials along with the 95% confident intervals and standard error evaluated using the curve fitting tools in MATLAB. The peak pressure attenuation coefficient of the propagating acoustic signal was estimated using the curve of best fit. CI-1 and CI-2 in the Table 9.1 represents the upper and lower values of peak pressure attenuation coefficient within the 95% confidence intervals.

Table 9.1: Attenuation coefficient of peak pressure of the acoustic pulse in polymeric materials.

Material	Peak Pressure Attenuation Coefficient (Np/cm)	Confidence Interval (CI-1)	Confidence Interval (CI-2)	Standard Error (SE)
PU40	0.0409	0.0436	0.0383	0.0014
PU70	0.1258	0.1332	0.1183	0.0038
PU90	0.1004	0.111	0.0898	0.0054
Nylon	0.0427	0.0595	0.0258	0.0086
PP	0.1720	0.2098	0.1342	0.0193

9.2.4 Propagation Velocity of Acoustic signal

A tailored adaptation of the time of arrival approach was employed to estimate the propagation speed of the acoustic signal in each polymer. The arrival time of the pulse was determined by when the signal form the acoustic sensor first rose above the noise floor. Given that the polymeric rods were positioned at 3 cm from the discharge source, the acoustic signal was assumed to originate from the

discharge, pass through the air, and then transmit through the polymeric rod before being recorded on the scope. Two different approaches from here were adopted to estimate the propagation velocity in each material and both are explained below and the deviation in results of both these approaches are also tabulated below. In first approach, it was assumed that the speed of acoustic signal propagation in air is 343 m/s. Therefore, the relevant time delay of 87.5 µs for 3cm air gap was subtracted from the measured TOA of the acoustic signal in each material.

For each length of the rod, the effective TOA was calculated and plotted against the respective rod length. The slope ($m = \frac{1}{V_{Polymer}}$) of the line of best fit through these data points allowed the estimation of the propagation speed of the acoustic signal within each material. Figure 9.13 and Figure 9.14 illustrate the relationship between effective TOA and rod length for various PU materials and Nylon and PP, respectively. Additionally, Table 9.2 summarizes the estimated propagation velocities of the acoustic pulse in each material.
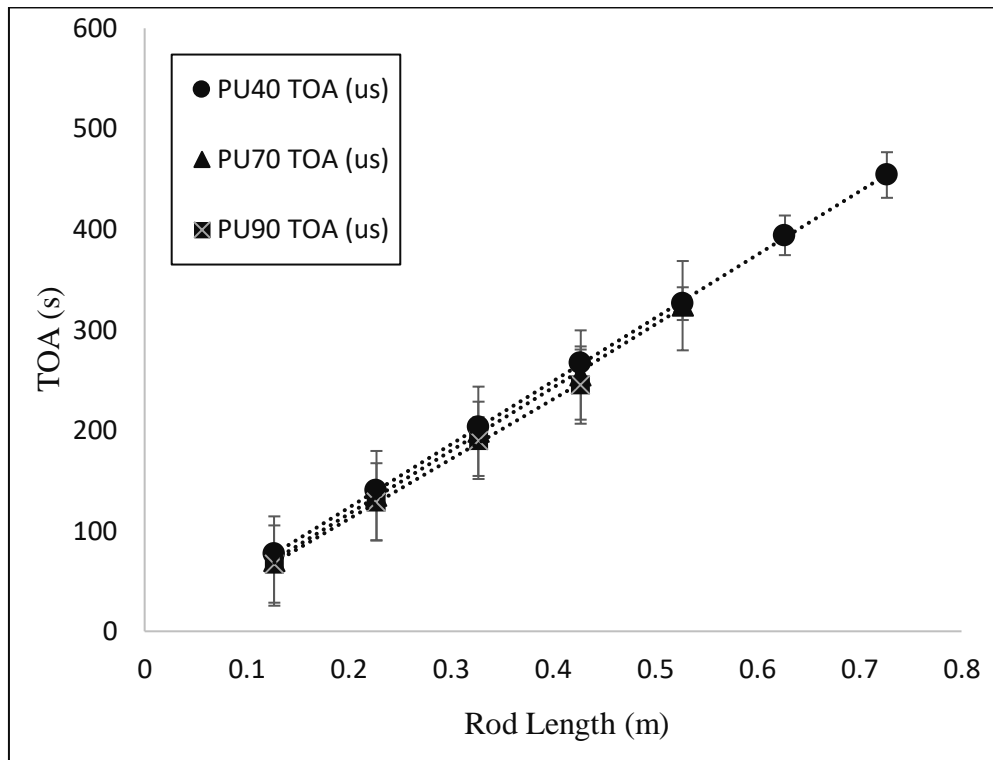
Figure 9.13: Time of Arrival (TOA) of acoustic pulse at different lengths in each type of PU.
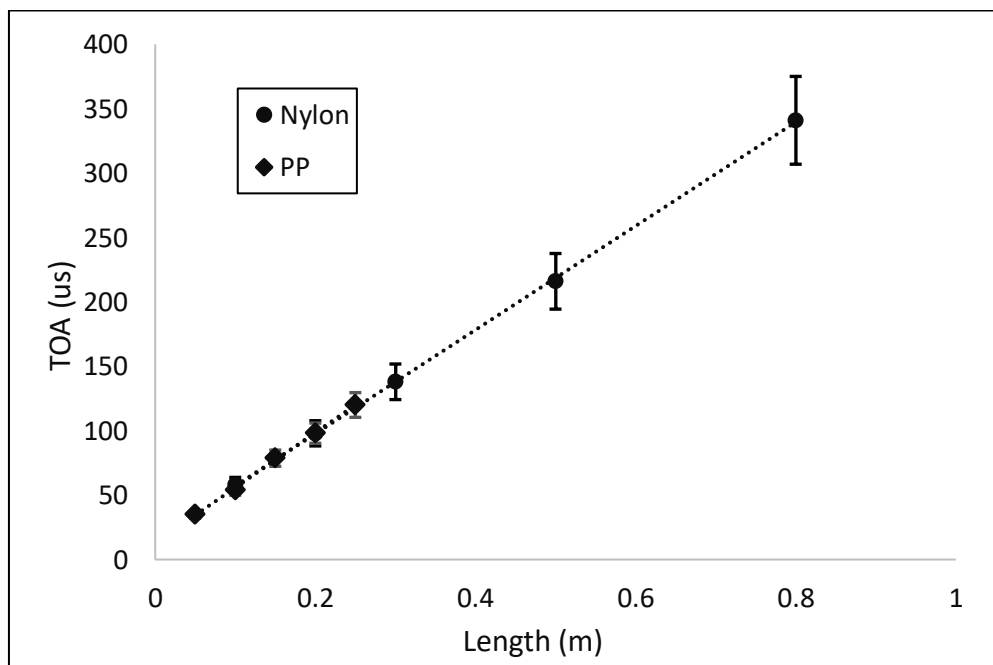
Figure 9.14: Time of Arrival (TOA) of acoustic pulse at different lengths in each type of Nylon and PP.

Table 9.2: Propagation velocity of acoustic signals in polymeric rods.

Material	Speed of Propagation (m/s)
PU40	1589
PU70	1592
PU90	1678
Nylon	2481
PP	2364

The propagation velocity of the acoustic signal in each material was also estimated without assuming the propagation velocity of the acoustic signal in air. The propagation velocity of the acoustic signal in each material was estimated using the measured TOA of the acoustic signal for the respective lengths of the rods and a linear fit was made to this data. The gradient of the line of best fit again is equal to the reciprocal of the propagation velocity. The intercept with the TOA axis indicates the time taken for the pressure wave to form and to propagate across the air gap. Further, the harder materials tend to have higher densities and greater elasticity than softer materials. As a result, acoustic signals propagate faster through hard materials because the atoms or molecules in these materials are more closely packed and can transmit energy more efficiently through elastic interactions. Conversely, in softer materials, the lower density and reduced elasticity impede the transmission of acoustic signals, resulting in slower propagation speeds. Table 9.3 shows the estimated propagation speed in air and the polymeric rods.
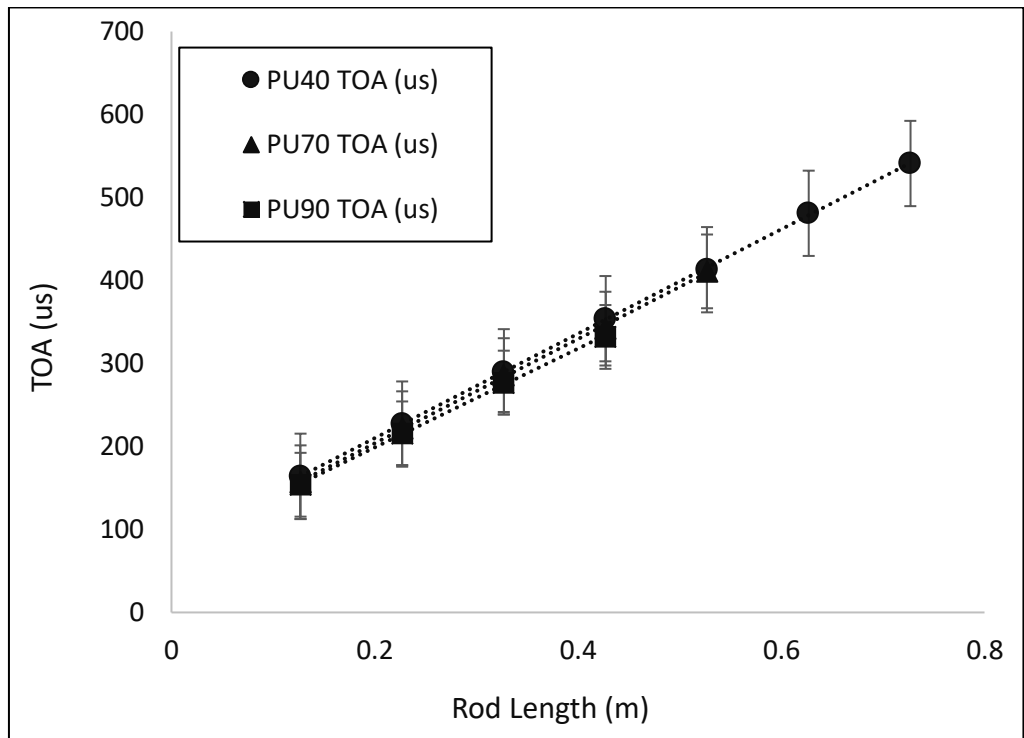
Figure 9.15: TOA of acoustic signal propagating through air and PUs.
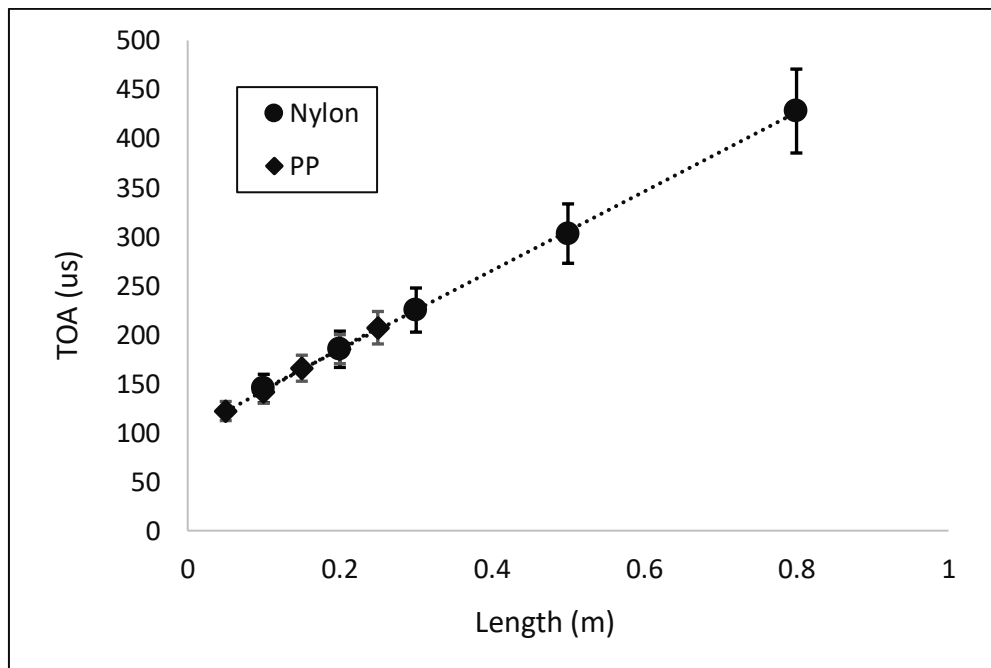
Figure 9.16: TOA of acoustic signal propagating through air and Nylon and PP.

Table 9.3: Propagation velocity of acoustic signals in polymeric rods.

Medium	Speed of Propagation (m/s)
Air	337
PU40	1589
PU70	1594
PU90	1681
Nylon	2480
PP	2365

9.2.5   Attenuation of Energy of the acoustic signal

It was observed that the propagation capability of the acoustic signal decreases as the hardness of the PU material increases. This suggests that higher hardness materials lead to greater energy loss of the acoustic signal. Hence, it is valuable to explore the attenuation coefficient of the energy as the acoustic travels through the material.

The acoustic signal, when propagating through the cylindrical polymeric rods, strike at the surface of the sensor. The energy associated with this acoustic signal can be determined by integrating the signal's energy density over the volume it occupies within the material. Considering the cylindrical shape of the rods and if the pulse travels along the length of the cylinder, we can define that at time t_0 the signal lies between two points: x_1 as the point closest to the source of the pressure signal and x_2 as the point farthest from the source. The vector $\bar{x}_{12}$ points in the direction of signal travel.

Assuming that the pulse can be described at the moment of observation by:

$$P_{t_0}(x) = \begin{cases} 0 & x < x_1 \\ \Phi(x - x_1) & x_1 \leq x \leq x_2 \\ 0 & x > x_2 \end{cases} \qquad (9.2)$$

Φ is a function defining the shape of the pressure signal. The energy contained in an infetisimal volume at position x can be calculated $dV = Adx$. It is important to note that the surface area of the sensor's mating surface was smaller than the surface area of the cylindrical rods, and thus, the variable "A" represents the surface area of the sensor.

$$dW = \frac{1}{\rho c^2} A \left(P_{t_0}(x) \right)^2 dx \qquad (9.3)$$

And therefore the total energy would be

$$W = \frac{1}{\rho c^2} A \int_{x_1}^{x_2} \left(P_{t_0}(x) \right)^2 dx \qquad (9.4)$$

To take into account what is happening in time the volume swept out by the signal associated with a infetisimal time interval dt should be considered. As time and the position of a point on the signal can be related through the velocity of the signal $x = ct$ so $dx = cdt$ therefore, the integral will become;

$$W = \frac{1}{\rho c^2} A \int_{t_1}^{t_2} \left(P_{x_0}(t) \right)^2 c\, dt = \frac{1}{\rho c} A \int_{t_1}^{t_2} \left(P_{t_0}(t) \right)^2 dt \qquad (9.5)$$

Equation 9.5 was used to estimate the energy of the acoustic signal detected by the sensor at various points along the rods. The MATLAB "trapz" function was employed to numerically evaluate the integral.

While the scalar speed of propagation of acoustic signal in each material were used as tabulated in Table 9.3, The density of each type of PU was also measured

in the laboratory using a flask and partly filling this flask with water. The water level was measured by using the scale on the flask. The small piece of PU40 was then inserted into the flask partly filled with water and new water level was measured. The difference in both water levels was used to calculate the density of the PU40. The same procedure was repeated for the other variants of PU, and it was found that the density of PU40, PU70 and PU90 was 1001 kg/m^3, 1070 kg/m^3, and 1120 kg/m^3 respectively.

For each length of the polymeric rods, ten acoustic signals were recorded. The energy of each of these ten signals was calculated using the above approach and then an average of these ten signals was calculated. The data was plotted to estimate the attenuation coefficient of energy by finding the curve of best fit accompanied by the 95% confidence interval using the same approach as adopted in section 9.2.3, while estimating the attenuation coefficient of the peak pressure of the acoustic signal. This assumed that the attenuation followed an exponential behaviour. Table 9.4 shows the attenuation coefficient of energy of the propagating acoustic signals in different materials along with the 95% confident intervals and standard error evaluated using the curve fitting tools in MATLAB. Figures 9.17 and 9.18 illustrate the acoustic energy of the signals at various lengths for all types of polymers accompanied by the 95% confidence intervals.
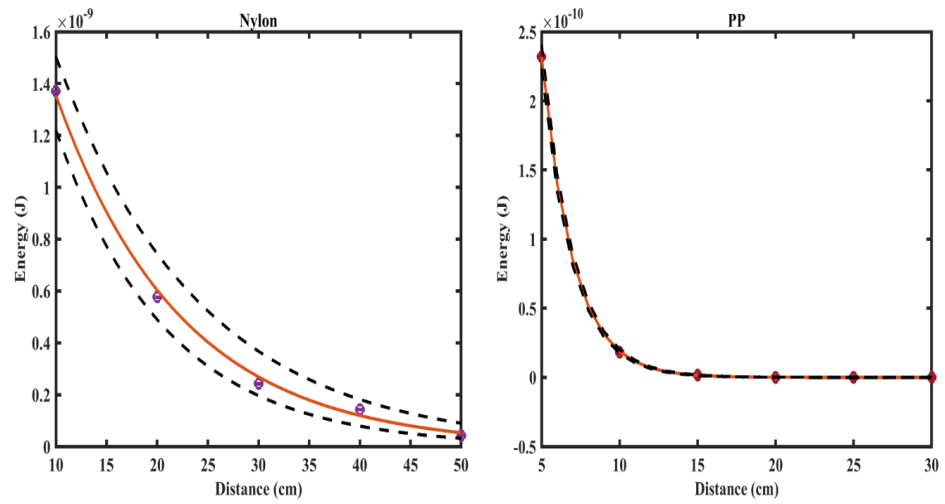
Figure 9.17**:** Energy of acoustic signals at different lengths of the rod for Nylon and PP with 95% confident interval (dashed lines).
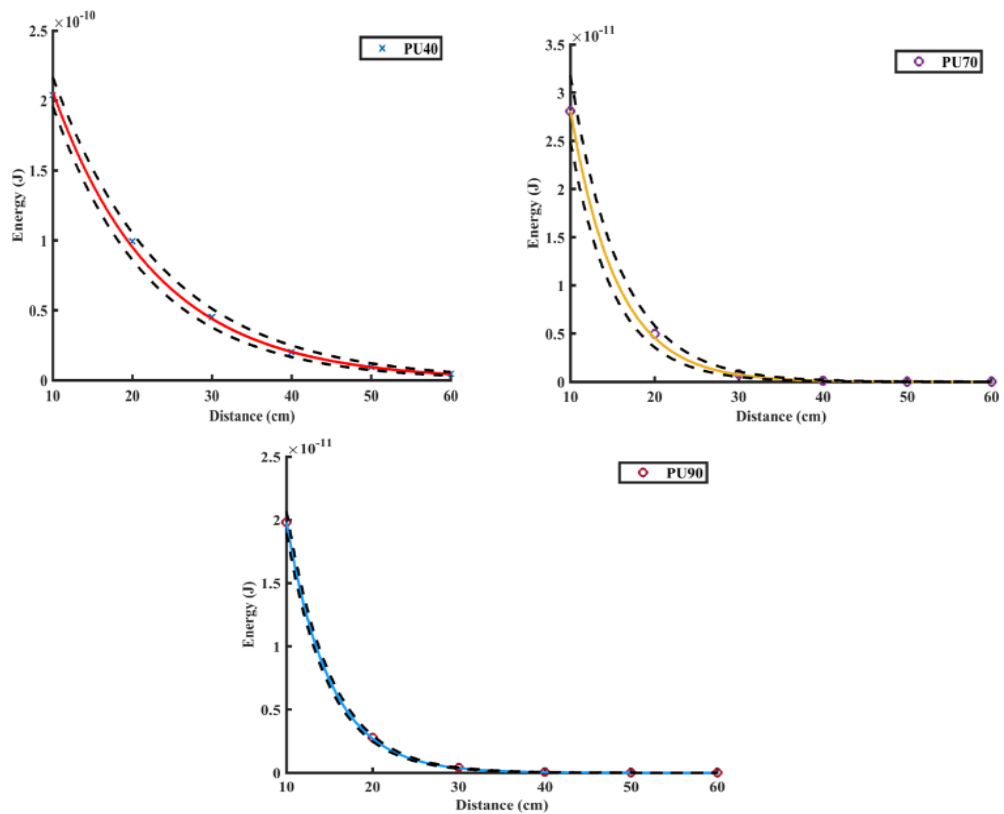
Figure 9.18**:** Energy of acoustic signals at different lengths of the rod for PU40, PU70, and PU90 with 95% confident interval (dashed lines).

Table 9.4 shows the value of α_E in each type of material along with 95% confidence intervals and standard error estimated using the curve fitting tools in MATLAB. The peak pressure attenuation coefficient of the propagating acoustic signal was estimated using the curve of best fit. CI-1 and CI-2 in the Table 9.4 represents the upper and lower values of peak pressure attenuation coefficient within the 95% confidence intervals.

Table 9.4: Attenuation coefficient α_E of energy of the acoustic signal in polymeric materials accompanied by 95% confidence intervals.

Material	Attenuation Coefficient of energy (Np/m)	Confidence Interval (CI-1)	Confidence Interval (CI-2)	Standard Error (SE)
PU40	0.0773	0.0823	0.0723	0.0026
PU70	0.1819	0.1941	0.1696	0.0062
PU90	0.1993	0.2038	0.1949	0.0023
Nylon	0.0809	0.0914	0.0705	0.0053
PP	0.5028	0.5103	0.4953	0.0038

9.2.6 Spectrum Analysis

Further, to explore the frequency spectrum of the acoustic signal propagating through the polymeric materials and the effects of the material`s composition on the spectrum of the propagating acoustic signal, Fast Fourier Transform (FFT) method was used. One of the pivotal parameters in frequency analysis is the sampling frequency. To capture the frequency content of the signals accurately

while ensuring that crucial information was preserved, the sampling frequency was defined according to the scope's sampling rate.

The standard response of the sensor, as shown in Figure 4.3, was used to estimate the sensor's transfer function analytically. Figure 9.19 visually represents this estimated transfer function.
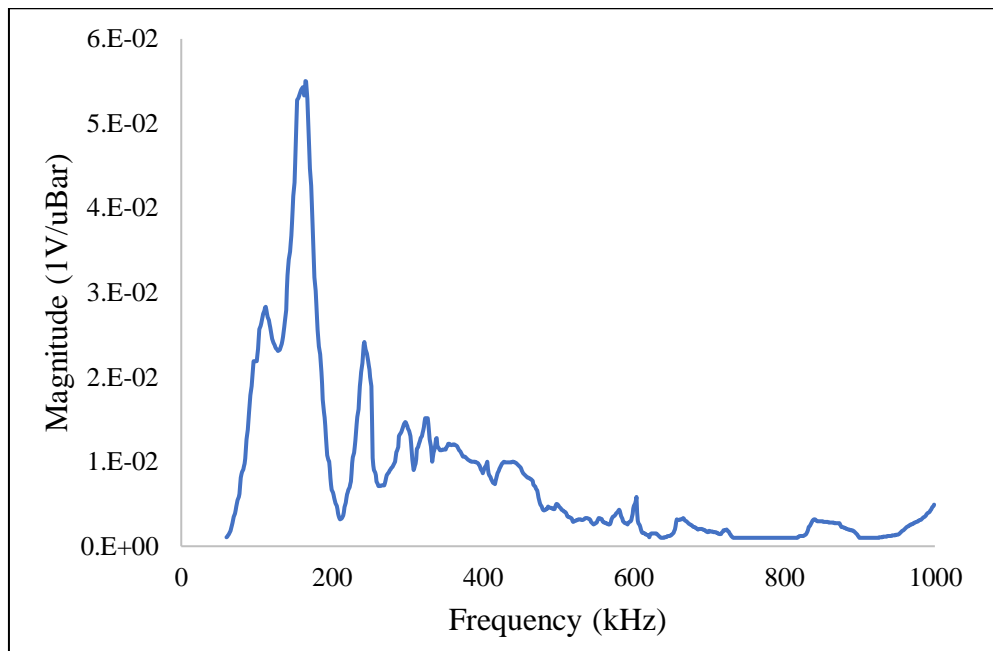
Figure 9.19: The transfer function of the sensor.

Moreover, the actual spectrum of the signal can be calculated using,

$$Actual\ Spectrum = \frac{FFT\ of\ the\ time\ domain\ signal}{Transfer\ function\ of\ the\ sensor} \tag{9.8}$$

9.2.6.1   Spectrum Analysis of Acoustic Signal in PU40

Figure 9.20 shows the changes in the actual spectra of the acoustic signals as they travel for different lengths in PU40. The FFT analysis was conducted to the average of multiple waveforms, with a waveform duration of 75 microseconds. The sampling

frequency utilized for this analysis was set at 25 MHz. The acoustic signal spectrum within PU40 is primarily concentrated within the frequency range of 60 kHz to 200 kHz. The deviation from a flat spectrum after applying the transfer function can be attributed to the characteristics of the sensor's response. Sensors typically have frequency-dependent sensitivities or filtering effects, meaning they may not equally detect all frequencies present in the original signal. As a result, applying the transfer function modifies the amplitudes of different frequency components, leading to a spectrum that reflects the true distribution of frequencies as detected by the sensor. This practical approach enhances the accuracy of the spectrum analysis by accounting for the sensor's inherent characteristics, providing a more realistic representation of the signal's frequency content. The dominant frequency spectra shift around the resonance frequency response at150 kHz. The frequency spectrum is dominated by frequency response of sensor.

Figure 9.20: The frequency spectrum of the acoustic signals propagating through PU40 at different lengths. The magnitude along the y-axis is in arbitrary units (a.u.).

171

9.2.6.2   Spectrum Analysis of Acoustic Signal in PU70

Figure 9.21 Illustrates the behaviour of the frequency spectra for acoustic signals propagating through PU rods of various lengths. The frequency range of the acoustic signal within PU70 falls between 60 kHz to 300 kHz. The transfer function of the sensor, depicted in Figure 9.19, indicates that the sensor's response does not detect the signal at zero frequency. However, in the process of calculating the actual spectrum of the signal, the division by the transfer function yields a higher value at 0 Hz. This intentional inclusion of the zero-frequency component provides a more realistic approach to comprehending the spectrum of the signal. Despite the sensor's inability to detect signals at zero frequency which can be observed in the spectrum at 40cm and 50cm in PU70. The alternative approach could be adopted by filtering all the frequency component which are below the sensitivity range of the sensor.

Furthermore, a discernible shift in the spectral peaks is noted in the spectrum of the acoustic signal as it propagates through PU70. Specifically, within the 10cm to 20cm length range of the rod, the frequency spectrum of the acoustic signal spans from 120kHz to 160kHz. However, at 30cm, this spectrum shifts to a lower frequency range of 80kHz to 100kHz. Subsequently, for rod lengths of 40cm and 50cm, the spectrum shifts towards higher frequencies, ranging from 150 kHz to 200kHz. These variations in spectral peaks suggest changes propagation characteristics along the length of the rod, indicating the influence of distance on the frequency content of the acoustic signal within PU70.
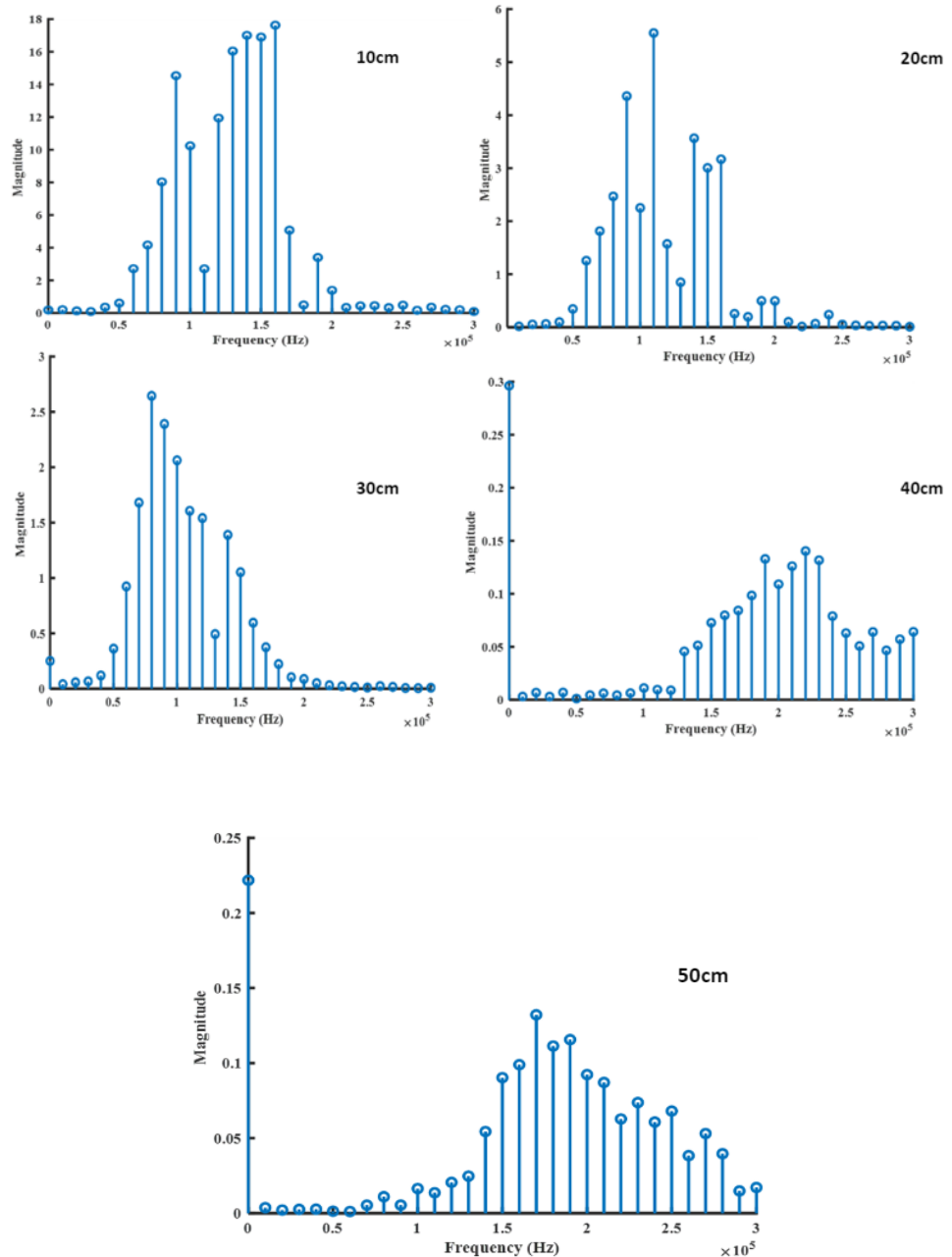
Figure 9.21: The frequency spectrum of the acoustic signal propagating through PU70 at different lengths. The magnitude along the y-axis is in arbitrary units (a.u.).

9.2.6.3 Spectrum Analysis of Acoustic Signal in PU90

Figure 9.22 Shows the behaviour of the frequency spectra for acoustic signals propagating through PU 90 rods of different lengths. The spectrum of the acoustic signal within PU90 exhibits a dominant frequency component at 80kHz and 90kHz

across rod lengths ranging from 10cm to 30cm. However, a notable shift in the spectrum was observed at 40cm, where the dominant component shifts to 200kHz. The shift in the spectrum of the acoustic signal with distance was observed for all the PU variants. However, this effect was more pronounced in PU70 and PU90 as compared to PU40 where the dominant component of the frequency spectrum remains around the 150kHz.
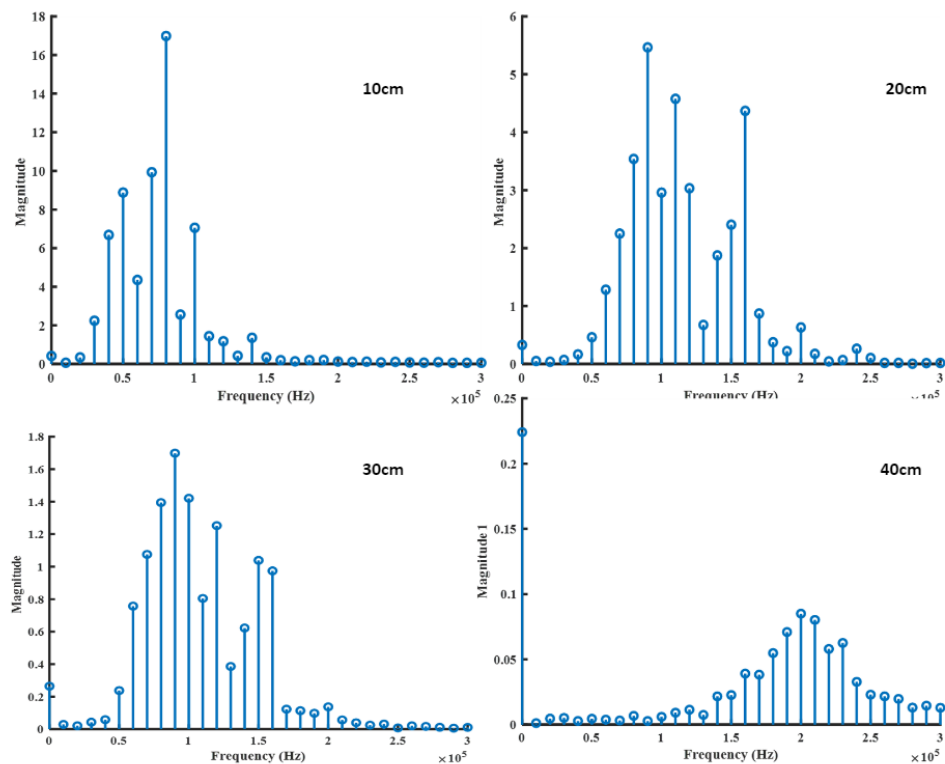
Figure 9.22: The frequency spectrum of the acoustic signal propagating through PU90 at different lengths. The magnitude along the y-axis is in arbitrary units (a.u.).

9.2.6.4   Spectrum Analysis of Acoustic Signal in Nylon

This section examines the effect of Nylon rod length on acoustic signal frequency distribution. Figure 9.23 shows the signal's frequency spectrum as it propagates through the Nylon. The frequency spectrum of Nylon lies between 70 kHz to 160 kHz.

174

The dominant frequency component of the acoustic signal for the rod length up to 30cm remain around 150 kHz like what was observed in PU40. However, the spectrum was shifted towards to lower frequencies below 80 kHz at 80cm like what was observed in PU70 and PU90.
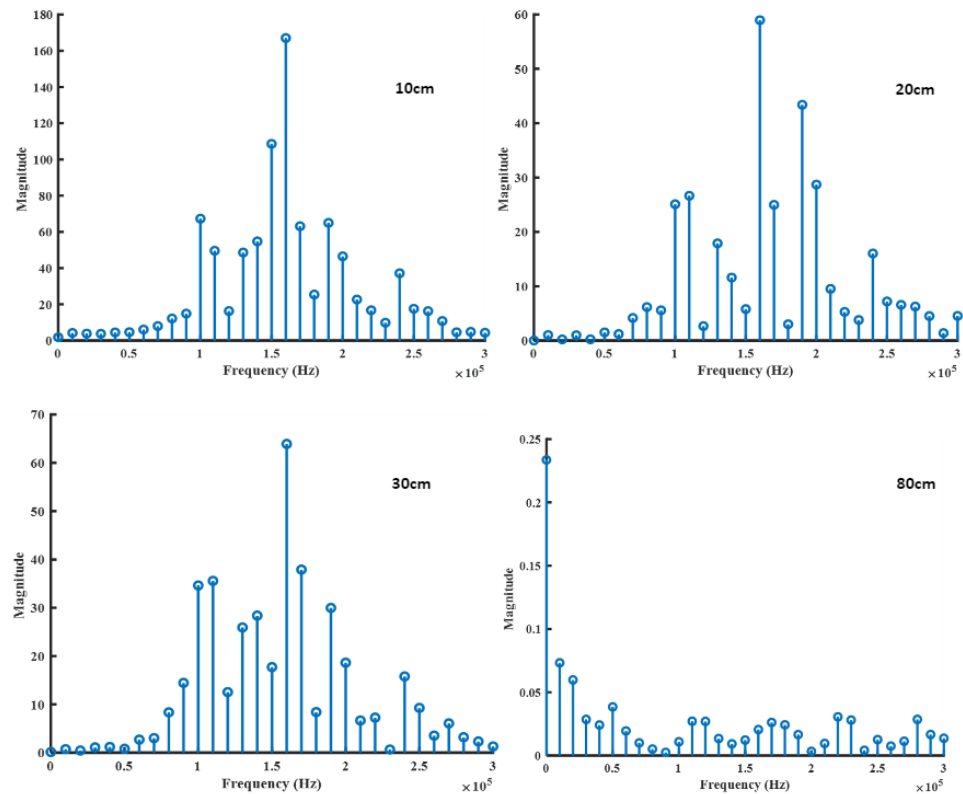
Figure 9.23: Frequency spectrum of Acoustic Signal in Nylon. The magnitude along the y-axis is in arbitrary units (a.u.).

9.2.6.5 Spectrum Analysis of Acoustic Signal in PP

Figure 9.24 Shows the changes in the frequency spectra between acoustic signals that have propagated through PP rods of various lengths. One noteworthy observation is that the spectrum lies between 60 kHz to 250 kHz unlike the other polymeric materials where the spectrum peaks were observed until 170 kHz.
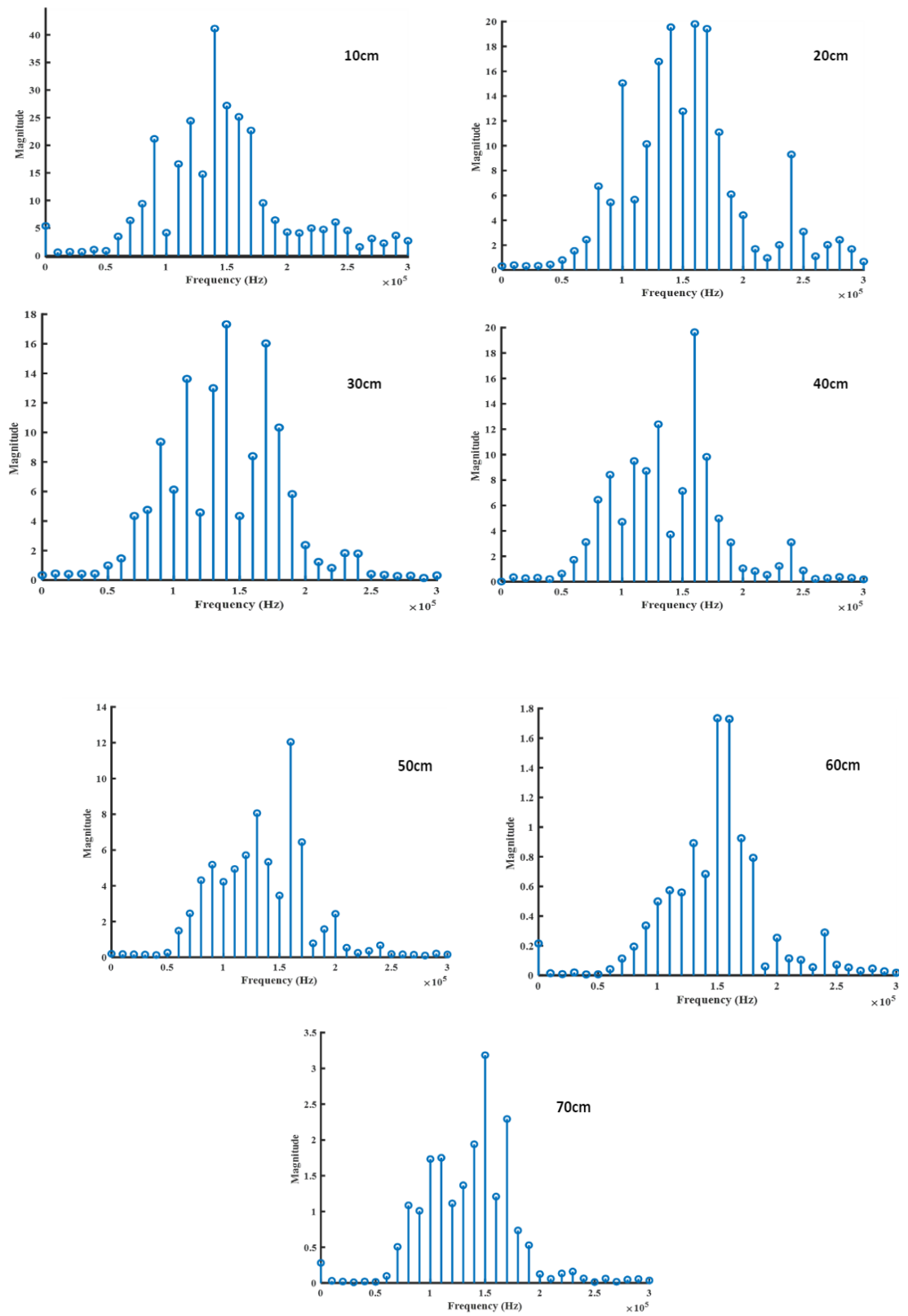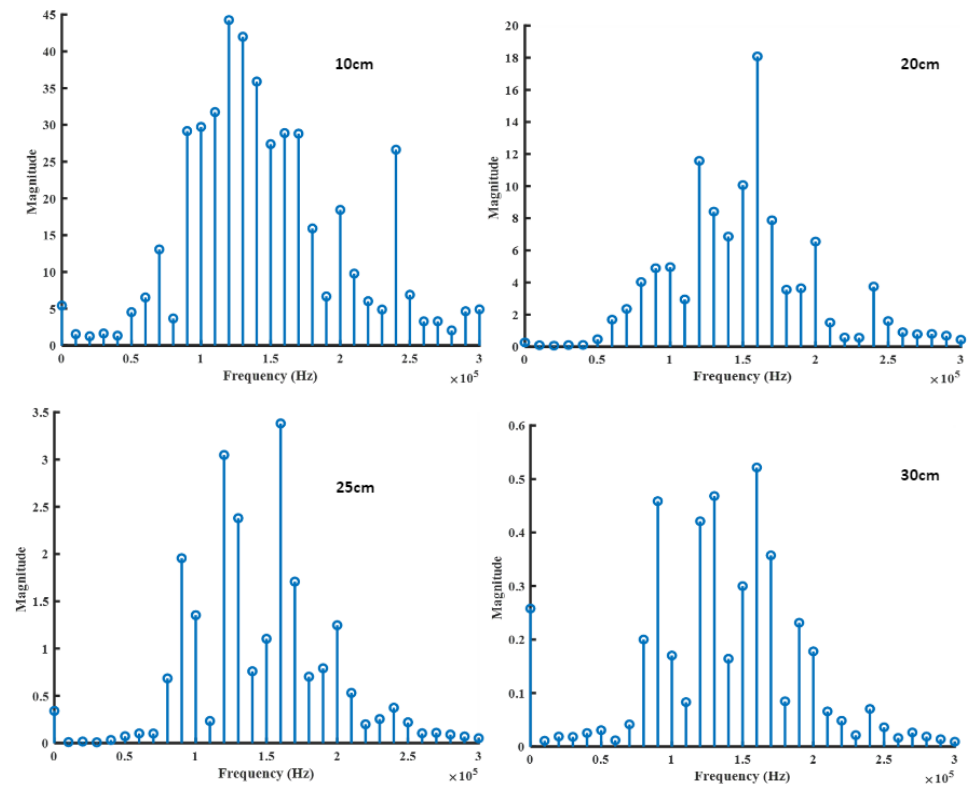
Figure 9.24: Frequency spectrum of acoustic signal propagating through PP.
The magnitude along the y-axis is in arbitrary units (a.u.).

9.3 Discussion

9.3.1   Propagation of Acoustic Signal

The results presented in section 9.2.6 shows that the acoustic signals were detectable at higher lengths of the rods for PU40, and Nylon as compared to the rest of the materials. PU40 and Nylon transmit the signal over longer distances due to the attenuation coefficient is smaller as compared to the other materials. Moreover, Table 9.5 shows the energies of the acoustic signals transmitted into the rods of different polymers along with the attenuation coefficients.

Table 9.5: Energies of the signals transmitted into different polymers.

In Chapter 8, the analysis of dielectric breakdown strength data unveiled a notable trend: the dielectric breakdown strength of the PU variants exhibited an increasing trend as the shore hardness of the material increased. This correlation between dielectric breakdown strength and shore hardness highlights the influence of material hardness on electrical insulation performance. Similarly, when investigating the propagation characteristics of acoustic signals in PU materials with varying hardness levels, a parallel behaviour was observed. Specifically, the transmittance of acoustic energy through the material from air demonstrated a decreasing trend as the hardness of the PU increased. This observation suggests that as the material hardness increases, there is a tendency for acoustic energy to be attenuated to a greater extent outside the material. Further analysis revealed a correlation between shore hardness and attenuation in energy of the propagating

acoustic signal within the PU variants. This correlation implies that PU materials with higher levels of hardness exhibit greater capability to attenuate energy.

Moreover, the energy transmitted into the system greatly depends upon the acoustic impedance of the systems which can be represented by,

$$z_0 = \rho c \qquad (9.7)$$

ρ being the density and c being the propagation velocity. Furthermore, the transmission of energy at the boundary between the air and the polymer depended on the transmission coefficient,

$$\Lambda = \frac{2z_p}{z_p + z_{air}} \qquad (9.8)$$

In PU, the differences in energy at the surface between PU40 and PU70 cannot be attributed to variations in density or propagation velocity, as these factors show negligible differences. Hence, the reduced transmission of acoustic energy can be attributed to the hardness of the materials while the hardness of the material depends on many factors apart from the density of the material as shown in Table 9.5.

Material	Energy at surface J	Alpha for Energy Np/cm	Shore Hardness
PU40	4.44E-10	0.0773	40
PU70	1.73E-10	0.1819	70
PU90	1.47E-10	0.1993	90
Nylon	31E-10	0.0809	80
PP	351E-10	0.5028	95

Furthermore, prior to striking the surface of the polymeric rods, the acoustic signals travels through air which results in dissipation of the acoustic energy. When this signal strikes with the surface of the rod, some of the energy is transmitted into the material, while the remaining energy is reflected from the surface. However, we all know that in actual PD event in a cavity in an underground cable insulation or cable joint, some of the energy is converted into heat and light while rest of the energy is available to initiate the acoustic impulse. In our case, significant decay in the energy of the acoustic impulse occurred due to two reasons: first, the propagation of the acoustic impulse through air before striking the surface of the rod, and second, the reflections from the surface of the rod. This is in addition to the energy loss incurred by heating and lighting.

However, despite all this energy loss, the partially transmitted acoustic energy was still detectable after 80cm of propagation through the material. This suggests that the acoustic signal may be able to travel until 100 cm, which is promising for its application in detecting PD in cable joints.

Another possible reasons behind the reduced capability of propagation of acoustic signal is the crystallinity of the polymers. The DSC results presented in chapter 6, showed that the degree of crystallinity of the PU increases as the hardness of PU increases. As the propagating acoustic signal interact with the crystals in the material, can result in scattering of the acoustic signal in various direction. This scattering results in the loss of energy of the propagating signal leading to the reduced capability of propagation.

9.3.2 Attenuation in Pressure and Energy of Acoustic Signals

The peak magnitude of the propagating acoustic signal was estimated for different lengths of rod and resulted in exponential decay in peak pressure of the signal with distance. The peak pressure attenuation coefficient of the PU materials increases as the hardness of the material increase as shown in Table 9.1. Therefore, the acoustic signal was detectable for longer distance in PU40 and Nylon while least detectable in PU90 and PP.

Based on equation 9.1 and 9.5 the expected relationship between pressure and the energy of the acoustic signal

$$W(x) \propto \left(P(x)\right)^2 = P_0 e^{-2\alpha x} \qquad (9.9)$$

Therefore, it would be expected that the attenuation coefficient of the energy of the acoustic signal should be twice of the attenuation coefficient of the acoustic signals peak pressure. It was observed that the α_P and α_E for PU40, PU90, Nylon, and PP were in good agreement but the α_E for PU70 was 7% less the twice of α_P as shown in Table 9.1 and Table 9.4 as well as in Figure 9.17 and 9.18. The α_P and α_E of all the materials obtained during the curve fitting shown in Figure 9.17 and 9.18 represented in Table 9.1 and 9.4 are plotted in Figure 9. 25.
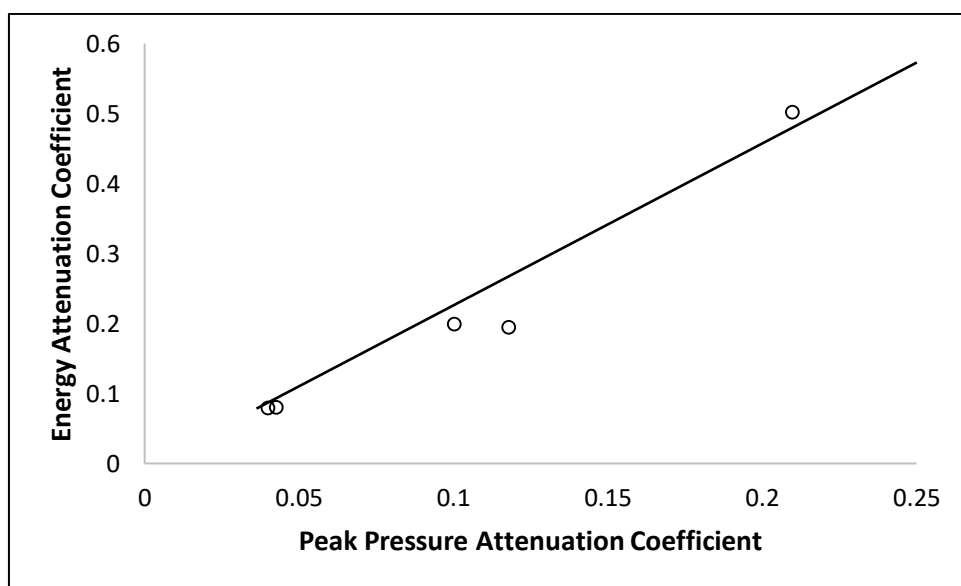
Figure 9.15: Attenuation coefficients of peak pressure VS acoustic energy in PU40, PU70, PU90, Nylon and PP.

Moreover, the properties like viscosity and elasticity of the propagating medium, the nature of the sound source, and the external environment in which the acoustic source is located, greatly affect the propagating AE signal. This complex interplay between the properties of the propagating medium, the nature of the source and the environment in which the source is located causes the AE signal to follow different path lengths or travel with different velocities. This results in a complex signal at the detector. Results of detected acoustic signals in section 9.2.6 shows

that AE signal detected at sensor has more than one impulse in each case. The presence of multiple impulses can be traced by the external reflections. As the discharge was created in air away from the surface of the rod and the acoustic impulse emitted from the discharge site travels in air and strike with the surface of the rod. It was observed that some of the acoustic energy was reflected from the surface of the rod. This acoustic pulse after being reflected, can collide with the electrode setup, and rebounded back to the surface of the polymeric rod, subsequently propagating through the material as shown in figure 9.25.
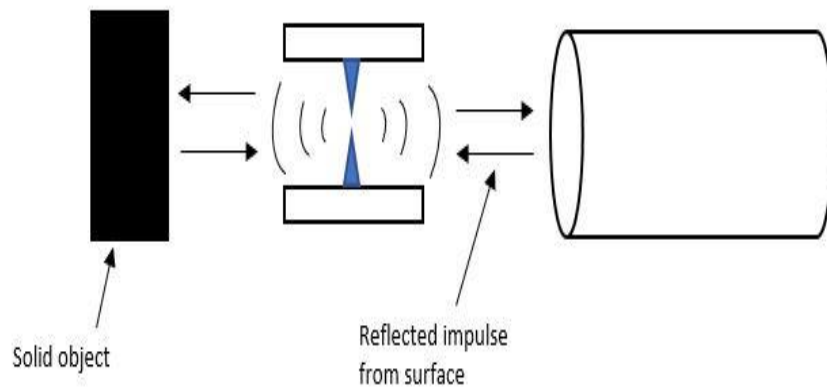
Figure. 9.26 Reflection of AE impulse model.

The spectrum analysis of the propagating acoustic signals at different lengths of the rods for each material suggests that the actual spectrum of the propagating acoustic signal is not consistent. However, reporting the actual spectrum by considering the transfer function of the sensor revealed new challenges in analysing the spectrum of the propagating acoustic signal unlike the results reported in the past where a consistent frequency spectrum was observed without considering the transfer function of the sensor. Moreover, efforts were undertaken to investigate whether there was any discernible correlation between the shift in

the magnitude of the spectrum and the length of the rods. However, despite these efforts, no consistent correlation was identified as this could have been affected by the presence of multiple impulses and their impact on the spectra. Further, investigations are needed to analyse the impact of multiple impulses on the frequency spectra of the propagating acoustic signal.

Overall, the results related to the propagation capability of acoustic signal show that the acoustic signals from a discharge has the capability to propagate through the polymeric materials and was detectable until 80cm long Nylon rod unlike the observation made in a FEA based COMSOL simulation model by T. Czaszejko [125] where the acoustic signal was hardly able to travel few millimetres. Further, the focus of the work by T. Czaszejko was to analyse the spectrum of the acoustic signal rather than analysing the propagation capability of the acoustic signal. Moreover, the COMSOL-based model simulation by T. Czaszejko was carried out on different polymers with idealized assumption. Nevertheless, significant differences in the propagation characteristics in polymeric materials used in this study suggest that each individual of the polymer family reacts differently towards the propagating acoustic signal. Therefore, we cannot rule out the use of acoustic detection techniques to detect and locate the PD in solid polymeric insulations. Similarly, it also suggests that the propagation capability of AE signal significantly depends upon the physical characteristics and morphology of the polymers. For instance, factors such as the polymer's composition, density, crystallinity, and molecular structure can influence its mechanical properties, including stiffness, elasticity, and thermal stability. These properties, in turn, affect the material's ability to transmit and propagate acoustic signals generated by internal events such as electrical discharges or mechanical stress. Additionally, variations in polymer

183

morphology, such as the presence of voids, inclusions, or structural defects, can create localized areas of acoustic impedance mismatch, leading to reflections, scattering, or attenuation of the propagating AE signals.

9.4 Summary

This chapter describes the propagation characteristics of an acoustic signal initiated from an electrical discharge propagating through different polymeric materials.

Here is the summary of the findings:

- The decay in energy and peak pressure values of the propagating acoustic signal follows an exponential decay pattern across all types of materials.

- The energy attenuation coefficient of PU variants increases with the hardness of the PU material, indicating higher attenuation in harder PU.

- The propagation velocity of the acoustic signal also increases with the hardness of PU, suggesting a relationship between material hardness and signal speed.

- When analysing the spectrum of the acoustic signal, it was observed that higher frequencies exhibited more significant attenuation in magnitude with distance, compared to lower frequencies. However, no consistent trend was identified in the attenuation of the spectrum peaks of the propagating acoustic signal in different materials. This lack of consistency can be attributed to the influence of the transfer function on

184

the spectral peaks, leading to variations in the attenuation levels across different frequency components.

These findings provide valuable insights into the behaviour of acoustic signals in different materials and highlight the influence of material properties on signal characteristics.

Chapter 10

Conclusions and Recommendations for Future Work

10.1   Conclusions

In this project, a comprehensive dual approach was adopted to address the challenges of high voltage insulation.

Firstly, PU (which is well-known for its self-healing properties) with different levels of hardness, was investigated for its dielectric characteristics and potential to be utilized as an insulating material for high voltage cable insulation. The study aimed to explore the effectiveness of PU in improving the insulation performance of high voltage cables and reducing the risk of electrical breakdowns. Additionally, Nylon and PP were employed for comparison with the PU variants to assess and contrast the results across different polymer families. The dielectric breakdown characteristics of PU materials exhibit a consistent trend in both AC and DC scenarios. The experimental results demonstrate that as the hardness of the PU increases, the dielectric breakdown strength also increases. Previous research reveals that the self-healing capability of PU can decrease as the material's hardness increases, whereas the dielectric strength of PU demonstrates an increase with hardness.

Secondly, the potential of the acoustic emission technique was also explored to detect and locate PD faults in electrical power cables' insulation. The study aimed

to investigate the challenges and effectiveness of this technique in detecting and locating PD faults in high voltage cables' insulation. A finite element method (FEM) based methods of COMSOL Multiphysics and MATLAB were used to analyse acoustic pulse propagation in polymeric insulating materials. The simulations revealed the significant impact of reflections and multiple paths on the shape, magnitude, and arrival time of the acoustic pulse and this challenge can be addressed by using the PML in COMSOL Multiphysics. Moreover, experimental analyses were conducted to examine the propagation characteristics of AE signals across different hardness levels of PU, Nylon, and PP. While attenuation coefficients exhibited an exponential decay across all materials, AE signals remained detectable up to considerable distances, particularly in PU40 and Nylon. These findings suggest the viability of AE techniques, especially in cable joints, despite attenuation challenges. Furthermore, PU40, characterized by its lower energy attenuation coefficient and flexibility as compared with its counterparts, makes it a promising candidate for use in cable joints where maintaining the integrity of insulation is crucial. The following conclusions can be made from the study;

1. The dielectric breakdown strength of polymers tends to increase as the shore hardness of the material increases. However, in the case of PU, previous research revealed that the self-healing capability can decrease with higher shore hardness. This suggests that harder materials exhibit greater resistance to electrical breakdown but can compromise self-healing properties. Therefore, it is important to explore the balance between self-healing capability, dielectric breakdown strength, and hardness of PU.

2. The FEA model and MATLAB model revealed that reflections occurring at the boundary of the material significantly influence both the magnitude and shape of propagating acoustic impulses. Consequently, it is important to accurately quantify the cumulative impact of these reflections when interpreting acoustic impulses detected from PD sources. Understanding and accounting for these reflections are essential for accurately diagnosing and locating PD faults within power cable insulation.

3. Acoustic signals propagating through the polymeric rod in each material exhibited a higher attenuation coefficient of energy, which can limit the effectiveness of AE detection techniques in power cables over long distances. Despite this limitation, there is potential for AE detection to be employed effectively at cable joints and cable terminations. At these localized points, the higher attenuation coefficient may be less of a hindrance, making AE detection a viable method for detecting and locating PD faults, thereby improving the reliability and safety of power cable systems.

10.2   Recommendations for Future Work

The results presented in this project show that a great deal of further investigation is needed in the following areas:

a) The PU, synthesized in the laboratory with different ratios of hard and soft segment could be analysed for its dielectric characteristics as well as the self- healing capabilities. This is crucial as our results showed that the dielectric characteristics are improved with higher hardness of PU which according to literature may result in poor self-healing capabilities. Therefore,

it is necessary to uncover the trade-off between the dielectric characteristics and self-healing capabilities of PU. Further, understanding this trade-off is crucial for potential applications of PU as insulation material in high voltage systems.

b) The potential of the AE technique in detecting and locating defects in various materials could be explored with the development of more advanced models that incorporate additional factors such as environmental conditions, ultimately improving the accuracy and efficiency of acoustic pulse detection in real world settings.

c) More realistic PD simulators could be developed. In service cable insulation, PD frequently occurs inside cavities within the polymeric insulation. The acoustic energy is conserved within the cavity and available to propagate through the polymeric insulation, unlike the current system where the acoustic energy first propagates through air. However, the energy provided to the point-point gap in the current simulator is considerably higher than that which would be expected for a partial discharge occurring in a void. Therefore, more sophisticated experimental setups should be developed to allow more accurate analysis of the detectability of acoustic pulses generated by partial discharges in polymeric insulation.

d) The experimental work was performed on rod-based samples surrounded by air. The structure of a practical cable is more complex, and experiments should be performed on models that more closely resemble the structures of a cable or a section of a service cable.

e) The acoustic sensor was positioned at the end of the rod optimising the detection of the signal this would not be possible in a practical cable and other detector locations like radial axis of the rod should also be considered.

Appendices

Appendix 1: MATLAB code to simulate the effects of multiple propagation paths on the propagating acoustic pulse in cylinder

```matlab
function [outputArg1] = pulse(time,start, width, ramp )

if time <=start
        outputArg1=0;

elseif time <=start+ramp
    outputArg1=(time-start)/ramp;

elseif time<=start+(width-ramp)
    outputArg1=1;

elseif time<=start+ width
    outputArg1=1-((time -(start+width-ramp))/ramp);

else
    outputArg1=0;
end
end
```

This script simulates the propagation of pulses along a rod of material

It takes into account multiple reflections from the boundary of the rod.

It assumes:

- the rod is infinite in length with no reflections occurring at the end of the rod
- The point of observation is assumed to lie on the axis of the rod
- the material is linear and lossless.
- the pulses represent a pressure
- The base unit for time is the microsecond
- The propagation velocity is constant

Background analysis

Figure 1 below shows a set of 4 possible paths for pulse to travel between the source S and point of observation P.
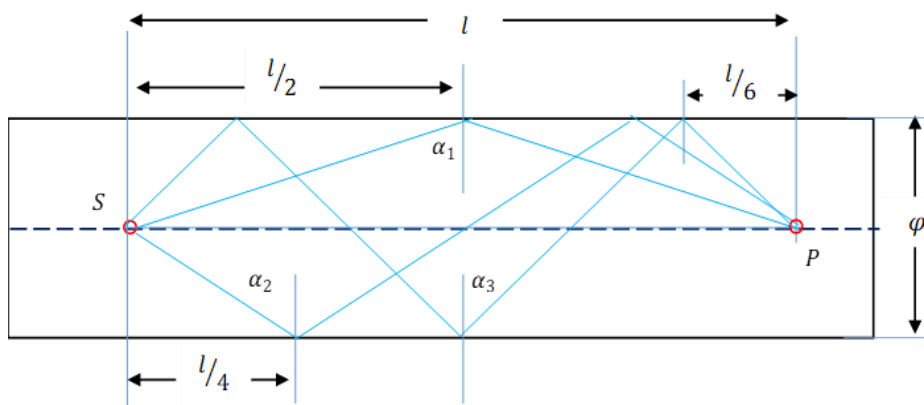
The length of a path with n reflections can be shown as

$$d_n = l \sqrt{1 + n^2 \left(\frac{\varphi}{l}\right)^2}$$

and the sin of the angle α_n associated with the path with n reflections is:

$$\sin \alpha_n = \frac{d_0}{d_n} = \frac{1}{\sqrt{1 + n^2 \left(\frac{\varphi}{l}\right)^2}}$$

193

assume that a pressure wave defined by the function $\zeta(t)$ propagates along each path

the pressure wave normal to the cross section of the rod associated with a path with n reflections is given by

$$P_n = \sin\alpha_n \zeta\left(t - \frac{l}{u_p}\sqrt{1 + n^2\left(\frac{\varphi}{l}\right)^2}\right) = \frac{d_0}{d_n}\zeta\left(t - \frac{l}{u_p}\sqrt{1 + n^2\left(\frac{\varphi}{l}\right)^2}\right) = \frac{1}{\sqrt{1 + n^2\left(\frac{\varphi}{l}\right)^2}}\zeta\left(t - \frac{l}{u_p}\sqrt{1 + n^2\left(\frac{\varphi}{l}\right)^2}\right)$$

If a reflection coefficient iΓs considered the expression will become:

$$P_n = \Gamma^n \frac{d_0}{d_n}\zeta\left(t - \frac{l}{u_p}\sqrt{1 + n^2\left(\frac{\varphi}{l}\right)^2}\right) = \Gamma^n \frac{1}{\sqrt{1 + n^2\left(\frac{\varphi}{l}\right)^2}}\zeta\left(t - \frac{l}{u_p}\sqrt{1 + n^2\left(\frac{\varphi}{l}\right)^2}\right)$$

Pulse Set Up

Note pulse is trapezoidal and is defined by two parameters pulseWidth indicating time in microseconds pulse is non zero and pulseRamp the time taken for the pulse to transition between zero and one, the maximum amplitude of the pulse. The pulse is

```
%base unit is the microsecond

pulseWidth=20;

pulseRamp=4;
```

General parameters in model

propVel is the speed of propagation for the pulses the unit is m/us, rodDiameter is the diameter of the rod in it is in meteres obPos is the distance between the source and the point where pressure is being measured in metres. the parameter noPaths defines the number of paths considered. The path with index equal to noPaths is involved with noPaths-1 reflections. simLength is the period of simulation in microseconds

```
propVel = 0.001; % in m/us effectively 1mm/us equivalent to 1000m/s

rodDiameter = 0.01; % in metres

obsPos = 10;        % in metres
```

```
noPaths =500;

simLength =2000;

timeStep = 0.05

gamma = 0.95
```

Array initialisation

pathLength(b) will hold the length travelled by a pulse undergoing b-1 reflections

normalMag(b) is the component of the pulse travelling along the axis of the rod effectively

```
pathLength=zeros(1,noPaths);

normalMag=zeros(1,noPaths);
```

pathLength(1) no reflections is set to separation of source and observation point on axis of rod

then remaining path lengths are calculated using equation above

```
pathLength(1)=obsPos;

for i=2:noPaths

 pathLength(i)=obsPos*sqrt(1+(i-1)^2*(rodDiameter/obsPos)^2);

end
```

Calculate values of normal component using $\sin \alpha_n = \dfrac{d_0}{d_n}$

```
normalMag=obsPos./pathLength;
```

calculate time taking pulse to travel for each path

```
propTimes=pathLength/propVel;
```

Calculate a starting time for the simulation to cover this is based on the propagation time for the shortest path minus 500 microseconds. This is used with simLength to set up a linearly spaced vector of time values

```
startTime=floor(propTimes(1)/500-1)*500;

time = startTime:timeStep:startTime+simLength;
```

Determine number of timesteps in time vector. This is not known as will depend on the values of simLength and timeStep. This is then used to initiate the array which stores the temporal behaviour of the pulse on each path.

```
[noRows,noCols]=size(time);

output=zeros(noPaths+1,noCols);
```

Calculate the temporal behaviour for all pulses at point of observation.

```
for i=100:noPaths

    effectMag =gamma^i*normalMag(i);

    for j =1:noCols

output(i,j)=effectMag*pulse(time(j),propTimes(i),pulseWidth,pulseRa
mp);

    end

end
```

Sum the individual temporal behaviours over all possible paths

```
for i=100:noPaths

    output(noPaths+1,:) = output(noPaths+1,:) + output(i,:);

end
```

```
plot(time,output(noPaths+1,:))

disp(max(output(1,:)));
```

Appendix 2: Propagation of Acoustic Pulse (Analytical Modelling)

Let us consider a pressure wave propagating spherically from a source. For simplicity assume that the pressure profile of this wave is rectangular and is with width ρ and the leading edge of the wave appears at a position r_p at a particular instant of time t_0

$$P(r, t_0) = \begin{cases} 0 & r < r_p - \rho \\ A(r_p) & r_p - \rho \le r \le r_p \\ 0 & r > r_p \end{cases} \qquad (1)$$

Note it is assumed that the relationship between r_p and t_0 is

$$r_p = ct_0$$

Where c is the propagation velocity;

Definition of the acoustic energy density is given by:

$$W = \frac{pv}{c} \qquad (2)$$

p pressure v is particle velocity c propagation velocity units of energy density is the Jm^{-3} or the pascal

what is the relationship between pressure and particle velocity this will come through the acoustic impedance Z

$$Z = \frac{p}{v} \qquad (3)$$

We can also define acoustic impedance in terms of the density of the material σ and the propagation velocity

$$Z = \sigma c \qquad (4)$$

Rearranging 3 and substituting from 4 gives

$$v = \frac{p}{Z} = \frac{p}{\sigma c} \qquad (5)$$

Substituting 5 into 1 leads to an expression for energy density in terms of pressure:

$$w = \frac{1}{\sigma c^2} p^2 \qquad (6)$$

Taking into account the form defined for the pressure wave in (1) we can write an expression for the energy density as a function of position r at time t_0.

$$w(r, t_0) = \frac{1}{\sigma c^2} \left(P(r, t_0) \right)^2 \qquad (7)$$

Considering a spherical shell thickness dr at distance r from the origin the energy contained within the shell can be defined as:

$$dw(r, t_0) = \frac{1}{\sigma c^2} \left(P(r, t_0) \right)^2 dV \qquad (8a)$$

Where dV is the volume of the shell.

$$dV = 4\pi r^2 dr \qquad (8b)$$

Therefore

198

$$dw(r, t_0) = \frac{4\pi}{\sigma c^2} r^2 \big(P(r, t_0) \big)^2 dr \qquad (8c)$$

The total acoustic energy present in the system can be found by integrating 8c

$$W = \frac{4\pi}{\sigma c^2} \int_0^\infty r^2 \big(P(r, t_0) \big)^2 dr \qquad (9a)$$

The integral in 9a can be rewritten as

$$\int_0^\infty r^2 \big(P(r, t_0) \big)^2 dr = \int_0^{r_p - \rho} r^2 \big(P(r, t_0) \big)^2 dr + \int_{r_p - \rho}^{r_p} r^2 \big(P(r, t_0) \big)^2 dr +$$

$$\int_{r_p}^\infty r^2 \big(P(r, t_0) \big)^2 dr \qquad (9b)$$

From properties of $P(r, t_0)$ defined in 1

$$\int_0^{r_p - \rho} r^2 \big(P(r, t_0) \big)^2 dr = 0 = \int_{r_p}^\infty r^2 \big(P(r, t_0) \big)^2 dr \qquad (9c)$$

Therefore equation 9a becomes

$$W = \frac{4\pi}{\sigma c^2} \int_{r_p - \rho}^{r_p} r^2 \big(A(r_p) \big)^2 dr = \frac{4\pi}{\sigma c^2} \big(A(r_p) \big)^2 \int_{r_p - \rho}^{r_p} r^2 dr \qquad (9d)$$

Performing the integration in 9d

$$W = \frac{4\pi}{\sigma c^2} \int_{r - \rho}^{r_p} r^2 \big(A(r_p) \big)^2 dr = \frac{4\pi}{\sigma c^2} \big(A(r_p) \big)^2 \frac{1}{3} [r^3]_{r_p - \rho}^{r_p} = \frac{1}{\sigma c^2} \frac{4\pi}{3} \Big[r_p{}^3 -$$

$$\big(r_p - \rho \big)^3 \Big] \qquad (10)$$

Where, as expected, we are seeing terms giving the volume of a spherical shell with thickness ρ .Problem here is the combination of terms associated with that volume $r_p{}^3 - \big(r_p - \rho \big)^3$ this prevents the possibility of producing a simple relationship between r_p and $A(r_p)$ at this point.

Try expanding out $r_p{}^3 - (r_p - \rho)^3$ to perhaps get a better form

$$3r_p{}^2\rho - 3r_p\rho^2 + \rho^3 = (3r_p{}^2 - 3r_p\rho + \rho^2)\rho \qquad \text{(11a)}$$

$$r_p{}^3 - (r_p - \rho)^3 = r_p{}^3 - (r_p{}^3 - 3r_p{}^2\rho + 3r_p\rho^2 - \rho^3) \qquad$$

This still leads to a polynomial in r_p and ρ it may be possible to get a more amenable form if the square is completed this would take the polynomial term into the form:

$$(3r_p{}^2 - 3r_p\rho + \rho^2)\rho = \left(3\left(r_p - \tfrac{1}{2}\rho\right)^2 + \tfrac{1}{4}\rho^2\right)\rho \qquad \text{(11b)}$$

Substituting 11b in 10 gives:

$$W = \frac{1}{\sigma c^2}\left(A(r_p)\right)^2 \frac{4\pi}{3}\left(3\left(r_p - \tfrac{1}{2}\rho\right)^2 + \tfrac{1}{4}\rho^2\right)\rho \qquad \text{(12)}$$

Normalise 12 by setting $W = 1$ this assumes energy conservation in the system independent of pulse position

$$\frac{1}{\sigma c^2}\left(A(r_p)\right)^2 \frac{4\pi}{3}\left(3\left(r_p - \tfrac{1}{2}\rho\right)^2 + \tfrac{1}{4}\rho^2\right)\rho = 1 \qquad \text{(13)}$$

Rearrange 13 to express $A(r_p)$

$$\left(A(r_p)\right)^2 = \sigma c^2 \frac{3}{4\pi}\frac{1}{\rho}\frac{1}{\left(3\left(r_p - \tfrac{1}{2}\rho\right)^2 + \tfrac{1}{4}\rho^2\right)} \qquad \text{(14a)}$$

So

$$A(r_p) = \sqrt{\sigma c^2 \frac{3}{4\pi}\frac{1}{\rho}\frac{1}{\left(3\left(r_p - \tfrac{1}{2}\rho\right)^2 + \tfrac{1}{4}\rho^2\right)}} \qquad \text{(14b)}$$

Behaviour in 12 b is complex, there is not a direct relationship between $A(r_p)$ and r_p. Why is the term in ρ^2 present in the denominator?

What happens when $r_p = 0$, part of equation 14 becomes:

$$3\left(r_p - \frac{1}{2}\rho\right)^2 = \frac{3}{4}\rho^2 \qquad (15a)$$

And 14b becomes

$$A(r_p) = \sqrt{\sigma c^2 \frac{3}{4\pi} \frac{1}{\rho^3}} \qquad (15b)$$

Note there is now terms describing the volume of a sphere with radius equal to the pulse width in equation 15b. This is physically unrealistic as it is describing a pulse that is associated with negative values of r in a polar coordinate system. This is a result of an inherent assumption in the maths that the pulse always exists, i.e. that there is no development of the pressure wave as energy is converted from an electrostatic to an acoustic form.

Would there be a benefit in defining r_p as the trailing edge of the pulse as this would remove the requirement for negative values of r the behaviour? In this case equation 1 would become:

$$P(r, t_0) = \begin{cases} 0 & r < r_p \\ A(r_p) & r_p \leq r \leq r_p + \rho \\ 0 & r > r_p + \rho \end{cases} \qquad (16)$$

Which leads to equation 12 taking the form:

$$W = \frac{4\pi}{\sigma c^2} \int_{r_p}^{r_p+\rho} r^2 \left(A(r_p)\right)^2 dr = \frac{4\pi}{\sigma c^2} \left(A(r_p)\right)^2 \frac{1}{3} [r^3]_{r_p}^{r_p+\rho} = \frac{1}{\sigma c^2} \frac{4\pi}{3} \left[(r_p + \rho)^3 - r_p^3 \right]$$ (17)

Again there are the polynomial terms involving r_p and ρ which can be simplified following the approach above 11a and 11b

$$\left[(r_p + \rho)^3 - r_p^3 \right] = 3r_p^2\rho + 3r_p\rho^2 + \rho^3 = \rho \left(3 \left(r_p + \frac{1}{2}\rho \right) + \frac{1}{4}\rho^2 \right)$$

(18)

So only change to equation 14(b) would be:

$$A(r_p) = \sqrt{\sigma c^2 \frac{3}{4\pi} \frac{1}{\rho} \frac{1}{\left(3\left(r_p + \frac{1}{2}\rho \right)^2 + \frac{1}{4}\rho^2 \right)}}$$ (19)

Setting $r_p = 0$ implies

$$3 \left(r_p + \frac{1}{2}\rho \right)^2 = \frac{3}{4}\rho^2$$ (20a)

Therefore

$$A(r_p) = \sqrt{\sigma c^2 \frac{3}{4\pi} \frac{1}{\rho^3}}$$ (20b)

Note this is identical to the expression obtained in 15b corresponding to a sphere of radius ρ This is physically realistic as it describes the system at the point when the transfer of electrostatic to acoustic energy has been completed.

Last thing to try is expressing the pulse in terms of the middle of the rectangular peak equation 1 would become:

$$P(r, t_0) = \begin{cases} 0 & r < r_p - \rho' \\ A(r_p) & r_p - \rho' \leq r \leq r_p + \rho' \\ 0 & r > r_p + \rho' \end{cases} \qquad (20c)$$

Note here we are using $\rho' = \rho/2$ for convenience

Equation 12 now takes the form:

$$W = \frac{4\pi}{\sigma c^2} \int_{r_p - \rho'}^{r_p + \rho'} r^2 \left(A(r_p) \right)^2 dr = \frac{4\pi}{\sigma c^2} \left(A(r_p) \right)^2 \frac{1}{3} [r^3]_{r_p - \rho'}^{r_p + \rho'} = \frac{1}{\sigma c^2} \frac{4\pi}{3} \Big[(r_p + \rho')^3 - (r_p - \rho')^3 \Big] \qquad (21)$$

Expanding out the cubic terms

$$\left(r_p + \rho' \right)^3 - \left(r_p - \rho' \right)^3 = \left(r_p^3 + 3r_p^2 \rho' + 3r_p \rho'^2 + \rho'^3 \right) - \left(r_p^3 - 3r_p^2 \rho' + 3r_p \rho'^2 - \rho'^3 \right) \qquad (22a)$$

$$\left(r_p + \rho' \right)^3 - \left(r_p - \rho' \right)^3 = 6r_p^2 \rho' + 2\rho'^3 = \rho' \left(6r_p^2 + 2\rho'^2 \right) \qquad (22b)$$

Substituting $\rho' = \rho/2$ in 22b gives:

$$W \rho' \left(6r_p^2 + 2\rho'^2 \right) = \rho \left(3r_p^2 + \frac{1}{4}\rho^2 \right) \qquad (22c)$$

This leads to equation 14 taking the form:

$$A(r_p) = \sqrt{\sigma c^2 \frac{3}{4\pi} \frac{1}{\rho} \frac{1}{\left(3r_p^2 + \frac{1}{4}\rho^2 \right)}} \qquad (23)$$

203

Note in this case the point where $r_p = \rho/2$ marks the point where the pulse has completely formed and the conversion of electrostatic energy to acoustic energy has been completed.

References

1. L'Abbate, A., et al. *The role of facts and HVDC in the future paneuropean transmission system development.* in *9th IET International Conference on AC and DC Power Transmission (ACDC 2010)*. 2010. IET.

2. Li, X., et al. *Influence of compatibilizers on the water-tree property of montmorillonite/cross-linked polyethylene nanocomposites.* in *2012 IEEE 10th International Conference on the Properties and Applications of Dielectric Materials*. 2012. IEEE.

3. Hanley, T.L., et al., *A general review of polymeric insulation for use in HVDC cables.* IEEE Electrical Insulation Magazine, 2003. **19**(1): p. 13-24.

4. Maruyama, S., et al., *Development of a 500-kV DC XLPE cable system.* Furukawa review, 2004. **25**(Mar.): p. 47-52.

5. Salivon, T., X. Colin, and R. Comte. *Degradation of XLPE and PVC cable insulators.* in *2015 IEEE Conference on Electrical Insulation and Dielectric Phenomena (CEIDP)*. 2015. IEEE.

6. Ma, F., et al. *Effect of thermal aging on mechanical and physical performances of resisting water tree XLPE.* in *2018 12th International Conference on the Properties and Applications of Dielectric Materials (ICPADM)*. 2018. IEEE.

7. Steennis, E. and F. Kreuger, *Water treeing in polyethylene cables.* IEEE Transactions on Electrical Insulation, 1990. **25**(5): p. 989-1028.

8. Zhang, Y.-Q., et al., *Water-tree resistant characteristics of crosslinker-modified-SiO2/XLPE nanocomposites.* Materials, 2021. **14**(6): p. 1398.

9. AlShaikh Saleh, M., et al., *The effect of protrusions on the initiation of partial discharges in XLPE high voltage cables.* Bulletin of the Polish Academy of Sciences. Technical Sciences, 2021. **69**(1).

10. Arachchige, T.G., et al. *Breakdown mechanisms of XLPE cable with insulation defects.* in *2020 IEEE Conference on Electrical Insulation and Dielectric Phenomena (CEIDP)*. 2020. IEEE.

11. Jeon, S.-I., et al. *A study on the partial discharge characteristics according to the distribution pattern of voids within an insulation.* in *Proceedings of 1995 IEEE 5th International Conference on Conduction and Breakdown in Solid Dielectrics*. 1995. IEEE.

12. Usuki, A., et al., *Synthesis of nylon 6-clay hybrid.* Journal of Materials Research, 1993. **8**(5): p. 1179-1184.

13. Kojima, Y., et al., *Mechanical properties of nylon 6-clay hybrid.* Journal of materials research, 1993. **8**(5): p. 1185-1189.

14. Yano, K., et al., *Synthesis and properties of polyimide–clay hybrid.* Journal of Polymer Science Part A: Polymer Chemistry, 1993. **31**(10): p. 2493-2498.

15. Lewis, T., *Nanometric dielectrics.* IEEE Transactions on Dielectrics and Electrical Insulation, 1994. **1**(5): p. 812-825.

16. Samad, A., et al., *Structure and breakdown property relationship of polyethylene nanocomposites containing laboratory-synthesized alumina, magnesia and magnesium aluminate nanofillers.* Journal of Physics and Chemistry of Solids, 2018. **120**: p. 140-146.

17. Lau, K., A. Vaughan, and G. Chen, *Nanodielectrics: opportunities and challenges.* IEEE Electrical Insulation Magazine, 2015. **31**(4): p. 45-54.

18. Van Herck, N. and F.E. Du Prez, *Fast healing of polyurethane thermosets using reversible triazolinedione chemistry and shape-memory.* Macromolecules, 2018. **51**(9): p. 3405-3414.

19. Kim, J., et al., *A heterocyclic polyurethane with enhanced self-healing efficiency and outstanding recovery of mechanical properties.* Polymers, 2020. **12**(4): p. 968.

20. Du, P., et al., *Synthesis of linear polyurethane bearing pendant furan and cross-linked healable polyurethane containing Diels–Alder bonds.* New Journal of Chemistry, 2014. **38**(2): p. 770-776.

21. Yaacob, M., et al., *Review on partial discharge detection techniques related to high voltage power equipment using different sensors.* Photonic sensors, 2014. **4**: p. 325-337.

22. Schwarz, R., T. Judendorfer, and M. Muhr. *Review of partial discharge monitoring techniques used in high voltage equipment.* in *2008 Annual Report Conference on Electrical Insulation and Dielectric Phenomena.* 2008. IEEE.

23. Czaszejko, T. and J. Sookun. *Acoustic emission from partial discharges in cable termination.* in *Proceedings of 2014 International Symposium on Electrical Insulating Materials.* 2014. IEEE.

24. Czaszejko, T. and J.A. Stephens. *Toward acoustic detection of partial discharges in high voltage cables.* in *9th International Conference on Insulated Power Cables.* 2015.

25. Phung, B., T. Blackburn, and Z. Liu, *Acoustic measurements of partial discharge signals.* Journal of Electrical & Electronics Engineering, Australia, 2001. **21**(1): p. 41-47.

26. Samad, A., et al. *Propagation of Acoustic Pulse Due to PD in Polymeric Insulating Material.* in *2023 INSUCON-14th International Electrical Insulation Conference (INSUCON).* 2023. IEEE.

27. Czaszejko, T. *The rustle of electrical trees.* in *2016 IEEE Conference on Electrical Insulation and Dielectric Phenomena (CEIDP).* 2016. IEEE.

28.   Ieda, M., *Electrical conduction and carrier traps in polymeric materials.* IEEE transactions on electrical insulation, 1984(3): p. 162-178.

29.   Green, C., et al., *Electrical and mechanical properties of new recyclable power cable insulation materials based upon polyethylene blends.* 2011.

30.   Hosier, I.L., et al., *High performance polymer blend systems for HVDC applications.* IEEE Transactions on Dielectrics and Electrical Insulation, 2019. **26**(4): p. 1197-1203.

31.   Tan, D.Q., *The search for enhanced dielectric strength of polymer-based dielectrics: a focused review on polymer nanocomposites.* Journal of Applied Polymer Science, 2020. **137**(33): p. 49379.

32.   Calebrese, C., et al., *A review on the importance of nanocomposite processing to enhance electrical insulation.* IEEE Transactions on Dielectrics and Electrical Insulation, 2011. **18**(4): p. 938-945.

33.   Mohamed, A.T., *Experimental enhancement for dielectric strength of polyethylene insulation materials using cost-fewer nanoparticles.* International Journal of Electrical Power & Energy Systems, 2015. **64**: p. 469-475.

34.   Andersson, M., *Polyethylene Blends, a Material Concept for Future HVDC-Cable Insulation.* 2017: Chalmers University of Technology.

35.   Dissado, L.A. and J.C. Fothergill, *Electrical degradation and breakdown in polymers.* Vol. 9. 1992: Iet.

36.   Ellis, B., *Chemistry and technology of epoxy resins.* 1993: Springer.

37.   Hong, R. and Q. Chen, *Dispersion of inorganic nanoparticles in polymer matrices: challenges and solutions*, in *Organic-Inorganic Hybrid Nanomaterials.* 2014, Springer. p. 1-38.

38.   Singha, S. and M.J. Thomas. *Polymer composite/nanocomposite processing and its effect on the electrical properties.* in *2006 IEEE Conference on Electrical Insulation and Dielectric Phenomena.* 2006. IEEE.

39.   Kurimoto, M., et al., *Dielectric properties of epoxy/alumina nanocomposite influenced by control of micrometric agglomerates.* IEEE Transactions on Dielectrics and Electrical Insulation, 2010. **17**(3): p. 662-670.

40.   Singha, S. and M.J. Thomas, *Permittivity and tan delta characteristics of epoxy nanocomposites in the frequency range of 1 MHz-1 GHz.* IEEE Transactions on Dielectrics and Electrical Insulation, 2008. **15**(1): p. 2-11.

41.   Li, Z., et al., *Highly conductive, flexible, polyurethane-based adhesives for flexible and printed electronics.* Advanced Functional Materials, 2013. **23**(11): p. 1459-1465.

42.   Jiang, S., et al., *Effect of surface silanization of carbon fiber on mechanical properties of carbon fiber reinforced polyurethane composites.* Composites Science and Technology, 2015. **110**: p. 87-94.

43.   Savas, L.A., et al., *Effect of microcapsulated red phosphorus on flame retardant, thermal and mechanical properties of thermoplastic polyurethane composites filled with huntite&hydromagnesite mineral.* Polymer Degradation and Stability, 2017. **135**: p. 121-129.

44.   Pokharel, P. and S. Choi, *The effect of hard segment length on the thermal and mechanical properties of polyurethane/graphene oxide nanocomposites.* Composites Part A: Applied Science and Manufacturing, 2015. **69**: p. 168-177.

45.   Zhu, D.Y., M.Z. Rong, and M.Q. Zhang, *Self-healing polymeric materials based on microencapsulated healing agents: From design to preparation.* Progress in Polymer Science, 2015. **49**: p. 175-220.

46.   Willocq, B., et al., *Advances in intrinsic self-healing polyurethanes and related composites.* RSC advances, 2020. **10**(23): p. 13766-13782.

47.   Lee, W.-J., H.-G. Oh, and S.-H. Cha, *A brief review of self-healing polyurethane based on dynamic chemistry.* Macromolecular Research, 2021. **29**(10): p. 649-664.

48.   Ku, C.C. and R. Liepins, *Electrical properties of polymers.* 1987: Hanser publishers Munich.

49.   Blythe, A.R. and D. Bloor, *Electrical properties of polymers*. 2005: Cambridge university press.

50.   Kelen, A., *Ageing of Insulatiog Materials and Equipment Insulation in Service and in Tests.* IEEE Transactions on Electrical Insulation, 1977(1): p. 55-60.

51.   Densley, J. *Ageing and diagnostics in extruded insulations for power cables*. in *Proceedings of 1995 IEEE 5th International Conference on Conduction and Breakdown in Solid Dielectrics*. 1995. IEEE.

52.   Mills, N., M. Jenkins, and S. Kukureka, *Plastics: microstructure and engineering applications*. 2020: Butterworth-Heinemann.

53.   Hutchinson, J.M., *Physical aging of polymers.* Progress in polymer science, 1995. **20**(4): p. 703-760.

54.   Harvey, J.A., *Chemical and physical aging of plastics*, in *Handbook of environmental degradation of materials*. 2005, Elsevier. p. 153-163.

55.   Fothergill, J.C. *Ageing, space charge and nanodielectrics: ten things we don't know about dielectrics*. in *2007 IEEE International Conference on Solid Dielectrics*. 2007. IEEE.

56.   Rowe, S. *Electrical ageing of composites: An industrial perspective*. in *2007 IEEE International Conference on Solid Dielectrics*. 2007. IEEE.

57. Champion, J. and S. Dodd, *The effect of voltage and material age on the electrical tree growth and breakdown characteristics of epoxy resins.* Journal of Physics D: Applied Physics, 1995. **28**(2): p. 398.

58. Montanari, G., *The electrical degradation threshold of polyethylene investigated by space charge and conduction current measurements.* IEEE Transactions on Dielectrics and Electrical Insulation, 2000. **7**(3): p. 309-315.

59. Dissado, L., et al., *Demonstrating a threshold for trapped space charge accumulation in solid dielectrics under DC field.* IEEE Transactions on Dielectrics and Electrical Insulation, 2005. **12**(3): p. 612-620.

60. Bahder, G., et al., *Physical model of electric aging and breakdown of extruded polymeric insulated power cables.* IEEE Transactions on Power Apparatus and Systems, 1982(6): p. 1379-1390.

61. Densley, J., *Ageing mechanisms and diagnostics for power cables-an overview.* IEEE electrical insulation magazine, 2001. **17**(1): p. 14-22.

62. Gargari, S.M., et al. *Practical experiences with on-line PD monitoring and interpretation for MV cable systems*. in *2010 10th IEEE International Conference on Solid Dielectrics*. 2010. IEEE.

63. Cuppen, A.N., E.F. Steennis, and P.C. van der Wielen. *Partial discharge trends in medium voltage cables measured while in-service with PDOL*. in *IEEE PES T&D 2010*. 2010. IEEE.

64. Takada, T., et al., *Space charge measurement in dielectrics and insulating materials.* Technical Brochures, 2006. **288**.

65. Takada, T., et al., *Guide for space charge measurements in dielectrics and insulating materials.* Electra, 2006. **224**: p. 52-63.

66. Mizutani, T., et al., *Pre-breakdown currents due to filamentary thermal breakdown in polyimide films.* IEEE transactions on electrical insulation, 1987(4): p. 473-477.

67. Kemp, I., *Partial discharge plant-monitoring technology: Present and future developments.* IEE Proceedings-Science, Measurement and Technology, 1995. **142**(1): p. 4-10.

68. Cavallini, A., et al., *First electron availability and partial discharge generation in insulation cavities: effect of light irradiation.* IEEE transactions on dielectrics and electrical insulation, 2005. **12**(2): p. 387-394.

69. Kreuger, F.H., *Partial discharge detection in high-voltage equipment.* (No Title), 1989.

70. Qiu, C. and N. Wang, *Techniques for measuring partial discharges in electrical apparatus*. 1994, Mechanical Industry Press, China.

71.   Bargigia, A., W. Koltunowicz, and A. Pigini, *Detection of parallel discharges in gas insulated substations.* IEEE Transactions on Power Delivery, 1992. **7**(3): p. 1239-1249.

72.   Chu, F., *SF6 decomposition in gas-insulated equipment.* IEEE Transactions on Electrical Insulation, 1986(5): p. 693-725.

73.   Chendong, X. *Monitoring paper insulation aging by measuring furfural contents in oil.* in *7th international symposium on high voltage engineering.* 1991.

74.   Sun, C., P.R. Ohodnicki, and E.M. Stewart, *Chemical sensing strategies for real-time monitoring of transformer oil: A review.* IEEE Sensors Journal, 2017. **17**(18): p. 5786-5806.

75.   Mariprasath, T. and V. Kirubakaran, *A real time study on condition monitoring of distribution transformer using thermal imager.* Infrared Physics & Technology, 2018. **90**: p. 78-86.

76.   Saha, T.K., *Review of modern diagnostic techniques for assessing insulation condition in aged transformers.* IEEE transactions on dielectrics and electrical insulation, 2003. **10**(5): p. 903-917.

77.   Liu, L., et al., *Remote optical thermography detection method and system for silicone polymer insulating materials used in power industry.* IEEE Transactions on Instrumentation and Measurement, 2019. **69**(8): p. 5782-5790.

78.   Wang, M., A.J. Vandermaar, and K.D. Srivastava, *Review of condition assessment of power transformers in service.* IEEE Electrical insulation magazine, 2002. **18**(6): p. 12-25.

79.   Villaran, M. and R. Lofaro, *Condition Monitoring of Cables Task 3 Report: Condition Monitoring Techniques for Electric Cables.* 2009, Brookhaven National Lab.(BNL), Upton, NY (United States).

80.   Gubanski, S., et al., *Diagnostic methods for outdoor polymeric insulators.* IEEE Transactions on Dielectrics and Electrical Insulation, 2007. **14**(5): p. 1065-1080.

81.   Singh, R., et al. *A review on traditional methods of condition monitoring of transformer.* in *2020 International Conference on Electronics and Sustainable Communication Systems (ICESC).* 2020. IEEE.

82.   Xia, C., et al., *Infrared thermography-based diagnostics on power equipment: State-of-the-art.* High Voltage, 2021. **6**(3): p. 387-407.

83.   Kemp, I. *Developments in partial discharge plant-monitoring technology.* in *1993 International Conference on Partial Discharge.* 1993. IET.

84.   Nattrass, D.A., *Partial discharge measurement and interpretation.* IEEE Electrical Insulation Magazine, 1988. **4**(3): p. 10-23.

85.   Wu, G. and D.-H. Park. *On-line monitoring instrument of fault discharge in large generators*. in *1999 Eleventh International Symposium on High Voltage Engineering*. 1999. IET.

86.   Zondervan, J., E. Gulski, and J. Smit, *Fundamental aspects of PD patterns of on-line measurements on turbogenerators*. IEEE Transactions on Dielectrics and Electrical Insulation, 2000. **7**(1): p. 59-70.

87.   Su, Q., *A new partial discharge detector for on-line insulation condition monitoring of generators*. 1997.

88.   Stone, G., *The use of partial discharge measurements to assess the condition of rotating machine insulation*. IEEE Electrical Insulation Magazine, 1996. **12**(4): p. 23-27.

89.   Lortie, R., et al., *Partial discharge detection on power transformers using a multi-terminal measurement method*. Proc. 10. ISH Montreal, Beitrag, 1997. **3210**.

90.   Boisseau, C. *Instrument transformers on line monitoring by means of partial discharge measurement*. in *7th International Symposium on High Voltage Engineering, 1991*. 1991.

91.   Cummings, H., J. Boyle, and B. Arp, *Continuous, online monitoring of freestanding, oil-filled current transformers to predict imminent failure*. IEEE transactions on power delivery, 1988. **3**(4): p. 1776-1783.

92.   Sheng, B., et al., *Partial discharge pulse propagation in power cable and partial discharge monitoring system*. IEEE Transactions on Dielectrics and Electrical Insulation, 2014. **21**(3): p. 948-956.

93.   Singsathien, J., et al. *Partial discharge detection and localization of defected power cable using HFCT and UHF sensors*. in *2017 14th International Conference on Electrical Engineering/Electronics, Computer, Telecommunications and Information Technology (ECTI-CON)*. 2017. IEEE.

94.   Álvarez, F., et al., *Application of HFCT and UHF sensors in on-line partial discharge measurements for insulation diagnosis of high voltage equipment*. Sensors, 2015. **15**(4): p. 7360-7387.

95.   Cox, B. *Partial discharge detection in GIS by an optical technique*. in *Proc. Int. Symp. on GIS*. 1985.

96.   De Maria, L., E. Colombo, and W. Koltunowicz. *Comparison among PD detection methods for GIS on-site testing*. in *1999 Eleventh International Symposium on High Voltage Engineering*. 1999. IET.

97.   Cosgrave, J., et al. *An optical fibre-based acoustic sensor for detecting electrical discharges in SF/sub 6/puffer circuit breakers*. in *Seventh International Conference on Dielectric Materials, Measurements and Applications (Conf. Publ. No. 430)*. 1996. IET.

98.   Runde, M., B. Skyberg, and M. Ohlen. *Vibration analysis for periodic diagnostic testing of circuit-breakers*. in *1999 Eleventh International Symposium on High Voltage Engineering*. 1999. IET.

99.   Hoidalen, H., et al. *Continuous monitoring of circuit-breakers using vibration analysis*. in *1999 Eleventh International Symposium on High Voltage Engineering*. 1999. IET.

100.   Phung, B. *Partial discharge ultrasonic wave propagation in steel transformer tanks*. in *7th International Symposium on High Voltage Engineering, 1991*. 1991.

101.   Bengtsson, T., H. Kols, and B. Jonsson, *Transformer PD diagnosis using acoustic emission technique*. 1997.

102.   Howells, E. and E. Norton, *Detection of partial discharges in transformers using acoustic emission techniques*. IEEE Transactions on Power Apparatus and Systems, 1978(5): p. 1538-1549.

103.   Rengarajan, S., A. Bhoomaial, and K.K. Kishore. *Acoustic partial discharge measurements for transformer insulation-an experimental validation*. in *1999 Eleventh International Symposium on High Voltage Engineering*. 1999. IET.

104.   Lundgaard, L., M. Runde, and B. Skyberg, *Acoustic diagnosis of gas insulated substations: A theoretical and experimental basis*. IEEE Transactions on Power Delivery, 1990. **5**(4): p. 1751-1759.

105.   Bozzo, R. and F. Guastavino, *PD detection and localization by means of acoustic measurements on hydrogenerator stator bars*. IEEE transactions on dielectrics and electrical insulation, 1995. **2**(4): p. 660-666.

106.   Ghirelli, L., et al. *Acoustical method for partial discharge detection in high power capacitors*. in *1993 International Conference on Partial Discharge*. 1993. IET.

107.   Boczar, T., A. Cichon, and S. Borucki, *Diagnostic expert system of transformer insulation systems using the acoustic emission method*. IEEE Transactions on Dielectrics and Electrical Insulation, 2014. **21**(2): p. 854-865.

108.   Boya, C., et al., *Identification of multiple partial discharge sources using acoustic emission technique and blind source separation*. IEEE Transactions on Dielectrics and Electrical Insulation, 2015. **22**(3): p. 1663-1673.

109.   Tian, Y., et al. *Acoustic emission techniques for partial discharge detection within cable insulation*. in *2000 Eighth International Conference on Dielectric Materials, Measurements and Applications (IEE Conf. Publ. No. 473)*. 2000. IET.

110.   Venkatesh, A.P., M. Danikas, and R. Sarathi. *Understanding of partial discharge activity in transformer oil under transient voltages adopting acoustic emission technique*. in *2011 6th International Conference on Industrial and Information Systems*. 2011. IEEE.

111. Casals-Torrens, P., A. González-Parada, and R. Bosch-Tous, *Online PD detection on high voltage underground power cables by acoustic emission.* Procedia Engineering, 2012. **35**: p. 22-30.

112. Wang, X., et al., *Acoustic energy shifting in transformer oil at different temperatures.* IEEE transactions on Power delivery, 2005. **20**(3): p. 2356-2357.

113. Boczar, T. and D. Zmarzly, *Application of wavelet analysis to acoustic emission pulses generated by partial discharges.* IEEE transactions on dielectrics and electrical insulation, 2004. **11**(3): p. 433-449.

114. Cremer, L., M. Heckl, and B.A. Petersson, *Structure-borne sound: structural vibrations and sound radiation at audio frequencies.* 2005: Springer Science & Business Media.

115. Tian, Y., et al. *Acoustic emission detection of partial discharges in polymeric insulation.* in *1999 Eleventh International Symposium on High Voltage Engineering.* 1999. IET.

116. Harrold, R., *Acoustic theory applied to the physics of electrical breakdown in dielectrics.* IEEE Transactions on Electrical Insulation, 1986(5): p. 781-792.

117. Tozzi, M., et al., *PD detection in extruded power cables: an approximate propagation model.* IEEE Transactions on Dielectrics and Electrical Insulation, 2008. **15**(3): p. 832-840.

118. Sujon, M.A.S., A. Islam, and V.K. Nadimpalli, *Damping and sound absorption properties of polymer matrix composites: A review.* Polymer Testing, 2021. **104**: p. 107388.

119. Lionetto, F. and A. Maffezzoli, *Polymer characterization by ultrasonic wave propagation.* Advances in Polymer Technology: Journal of the Polymer Processing Institute, 2008. **27**(2): p. 63-73.

120. Verdier, C. and M. Piau, *Acoustic wave propagation in two-phase viscoelastic fluids: The case of polymer emulsions.* The Journal of the Acoustical Society of America, 1997. **101**(4): p. 1868-1876.

121. Rossing, T., *Springer handbook of acoustics.* 2007: Springer Science & Business Media.

122. Refaat, S.S. and M.A. Shams. *A review of partial discharge detection, diagnosis techniques in high voltage power cables.* in *2018 IEEE 12th International Conference on Compatibility, Power Electronics and Power Engineering (CPE-POWERENG 2018).* 2018. IEEE.

123. Rathod, V.B., G.B. Kumbhar, and B.R. Bhalja. *Simulation of Partial Discharge Acoustic Wave Propagation Using COMSOL Multiphysics and Its Localization in a Model Transformer Tank.* in *2020 21st National Power Systems Conference (NPSC).* 2020. IEEE.

124. Boczar, T., *Identification of a specific type of PD from acoustic emission frequency spectra.* IEEE transactions on Dielectrics and Electrical Insulation, 2001. **8**(4): p. 598-606.

125. Czaszejko, T. and J. Sookun. *Acoustic emission from partial discharges in solid dielectrics.* in *2014 IEEE Electrical Insulation Conference (EIC).* 2014. IEEE.

126. . DF-1.6 %âãÏÓ 143 0 obj <</Filter/FlateDecode/First 10/Length 368/N 2/Type/ObjStm>>stream 0 œÏH&î Q>Ù1m é¿'MÌ × °)Ì…e =«– Ë Jð ëòaòÈÍoÂO¯YLÏWvA ³ÇŒ â-Þ .Ø-‹□ÈðŽG□©»‡ê3 Ð -q"c ›´• 4G +¨¼¤ Z¹ZzzAÙ§ ' º Öä,ëµ/AsöûSà }Ð Oî ø"cÏ²'xh« 6|¦¤ßsKš¡?û €Ñ‹Þ* O ÂÄsï ß¹8Ru¨ýÊØ½¬L&N,, 1œÂ¤Ï}Ï ¡áÎC>Ÿ³ ®®¿Ø:(ÖÄØ¿€ô>1¶¶êWú^ ‹ÍÔÄÿÅÅƒm"{GóŒ ÷ÓÇÉ|9Ç□Û Ï□#=<±ª õâ1žÜ¤,□Z □$ U #È□‰ »šUíá— Ø¬4‡□D€^*²ZŸv!E KŸ¾c(¯Ê\j j□ÿÜe‹,! …½^/Kj`ÍÛžt ÚØïœ"Ù Å□ü|1cÌÇÔ‹@'íeKÊÀR ;D³z@□! endstream endobj 144 0 obj <</Filter/FlateDecode/First 152/Length 1312/N 19/Type/ObjStm>>stream I‰ÎbÛ gym»□™CY□ 'Y 2 Œün Â tAáq°¦÷¼UTó`ÍÞ9Á œ~ô#9¼ûKÀ®æÙû¾…ûoÛ-@P å"œaë—æÝ»÷ôM»a/½Â%ì:÷.»‡½< D,òbÍÓ8. Ûàz £˜- ±åÜ!z'Ž…ïÈã]Å—n¢Ò×Ô²qʼL ä§²ohbÔu¹t\NÓ)ž™ý>"ã Tn k¸ÍÞî¯wãß¹.Q ý′ÌÓ1¬[çœ]Õ)š< …ÀIHŠ • ÃÂt½ÙíY2)"ðàË^õ"©»Š,,h… IÄ $+jmÿZÏÈ□7Œ‰¸– Ø–ê££, ežÆ– ©□9{#pFP;:ï£v.[#s™"•ýåç/ÞU ,®Ô_Uâ }¤>2•üÎ8ás©„ŒÏ© æúÿˆ-~`P@ -%h<fzÎÆdšq:ƒqÔú¤"t'<ŠÚ¹&X×Ä@'a×ñI)€öõ¢¶+• F ¸ Š~TîTêNýÐÁ·w0soa× § ÖíÐ k¨5£æ²dvYKÍXaï9¨'3 □J□…Y,íü (-ÂBn V¥þùf bt,ç…ÆW@′m…e ¢CR• ÊßR[®tÔé—-+Lx CõÎÆˆ ¥ZÃÆ[«.ª‹; ƒ ã˜Þ'¦Ÿ°L «¯'¹°G_›ÿV …Ä-ÌÁøxA/a^}Í¤Œ€i4Â]ÜNïG¿ È âÂÃã<‹! 1ý!5úä¶™}9é*•÷mx– + ÷«D– ®ãÖ tÛf …• Ò×\ ù_Q/;Ñ • ÙßÝ- SÓòÊ/j},, Áz□áa'□ôÇ,, É ne,öª§ ä)¯.Úµÿ©Î¯ *(H µ'3 ?¥r9!2uv¬ÁF©aì>(GºÄ,?¦y'ø□ö …‰°±É Sú'v B×Ÿ Ž× ™#öÑû 2§ vIZ SYÏ¯×I ÁœnzÜkA¯È$□Iî>í□sÂ¥¬4©®dhŒâ…je V• Í˄> ¶eåŒìMãøöhŠwºå»PÀ hµ Hk±eAÝ Þ}&¦Î†·St=±2ÔG¶2 }GÀl "& ªåø»³Ý»9?"› `"^ ±ÂÌ1 5ÝÀÎtµ«ƒëæ4AÙ VþžE) ÅÆ \!ki□Ë ‡ Dá 2‹è™ ÞN{H @S °c'£â¬iJ¯ í Ñ»O=I êy □.Î^{Q"lh5~ /þÊàu°- ˆµüc[DÊz6□oÜ[õ³/!‡sd!□Øw`ûûxÌ+«ðúÌÎ²□¿†h[²□ü'ßóÞ " ü‡Ý&ù ÕÇü™Ä•27 □Œ |^ uÆmÚ8Ð5à©Kâi± OâYWq>\ ®Å³ÁgRŠeêJç h¶È € A^%áYCóSâÓ/þ¬□gAî7 Ø;â¤Ä" ^Í½¢ûU2□ð#¿ä° n ¼*Ã 9zµ)ºÆ ^OêDH.²- É,šµJcsÿø-L–K€¡áÏ'?ÛFšb• ûX~¿a(¹ ¨ Üý PÌ–01ëºRJ®v¡®Ÿ[O€

127. Bérenger, J.-P., *Perfectly matched layer (PML) for computational electromagnetics.* 2022: Springer Nature.

128. Johnson, S.G., *Notes on perfectly matched layers (PMLs).* arXiv preprint arXiv:2108.05348, 2021.

129. Liu, Q.-H. and J. Tao, *The perfectly matched layer for acoustic waves in absorptive media.* The Journal of the Acoustical Society of America, 1997. **102**(4): p. 2072-2082.

130. Jiang, T. and Y. Xiang, *Perfectly-matched-layer method for optical modes in dielectric cavities.* Physical Review A, 2020. **102**(5): p. 053704.

131. Sun, W., Q. Fu, and Z. Chen, *Finite-difference time-domain solution of light scattering by dielectric particles with a perfectly matched layer absorbing boundary condition.* Applied optics, 1999. **38**(15): p. 3141-3151.

132. Jiao, D., et al., *Time-domain finite-element simulation of three-dimensional scattering and radiation problems using perfectly matched layers.* IEEE transactions on antennas and propagation, 2003. **51**(2): p. 296-305.

133. Samad, A., et al. *Modelling of propagation characteristics of acoustic pulse from partial discharge in polymeric insulating materials.* in *acoustics*. 2024. MDPI.

134. Dissado, L., et al., *Weibull statistics in dielectric breakdown; theoretical basis, applications and implications.* IEEE Transactions on electrical insulation, 1984(3): p. 227-233.

135. Miller, H.C., *Flashover of insulators in vacuum: review of the phenomena and techniques to improved holdoff voltage.* IEEE transactions on electrical insulation, 1993. **28**(4): p. 512-527.

136. Ku, C. and R. Liepins, *Dielectric Breakdown of Polymers.* Electrical Properties of Polymers-Chemical Principles, 1987: p. 102-199.

137. Fournier, D. and L. Lamarre. *Interfacial breakdown phenomena between two EPDM surfaces.* in *1992., Sixth International Conference on Dielectric Materials, Measurements and Applications.* 1992. IET.

138. Tonglai, Z., et al., *The estimation of critical temperatures of thermal explosion for energetic materials using non-isothermal DSC.* Thermochimica Acta, 1994. **244**: p. 171-176.

139. Schick, C., *Differential scanning calorimetry (DSC) of semicrystalline polymers.* Analytical and bioanalytical chemistry, 2009. **395**: p. 1589-1611.

140. Grzelak, A.W., P. Boinard, and J.J. Liggat, *The influence of diol chain extender on morphology and properties of thermally-triggered UV-stable self-healing polyurethane coatings.* Progress in Organic Coatings, 2018. **122**: p. 1-9.

141. Mishra, A.K., et al., *FT-IR and XPS studies of polyurethane-urea-imide coatings.* Progress in organic coatings, 2006. **55**(3): p. 231-243.

142. Furukawa, M., et al. *Microphase separation of bulk and ultrathin films of polyurethane elastomers.* in *Macromolecular Symposia.* 2008. Wiley Online Library.

143. Vasanthan, N., *Crystallinity determination of nylon 66 by density measurement and fourier transform infrared (FTIR) spectroscopy.* Journal of Chemical Education, 2012. **89**(3): p. 387-390.

144. Fang, J., et al., *Needleless melt-electrospinning of polypropylene nanofibres.* Journal of nanomaterials, 2012. **2012**: p. 1-9.

145. Chang, S., *Analysis of polymer standards by Fourier transform infrared spectroscopy-attenuated total reflectance and pyrolysis gas chromatography/mass spectroscopy and the creation of searchable libraries.* Forensic Science Intership Marshall University Forensic Science Program, 2012.

146. Johnson, J.F. and R. Cole, *Dielectric polarization of liquid and solid formic acid1.* Journal of the American Chemical Society, 1951. **73**(10): p. 4536-4540.

147. Zhang, M., et al., *Modelling the low-frequency electrode dielectric response based on transformer equivalent oil-paper insulation model.* IET Science, Measurement & Technology, 2019. **13**(5): p. 700-707.

148. Kuffel, J. and P. Kuffel, *High voltage engineering fundamentals.* 2000: Elsevier.

149. Bernstein, B.S. and J.W. Tarpey, *Electrical insulation materials.* Electrical Power Cable Engineering, 2003: p. 58.

150. Weibull, W., *A statistical distribution function of wide applicability.* Journal of applied mechanics, 1951.

151. Lau, K.Y., *Structure and electrical properties of silica-based polyethylene nanocomposites.* 2013, University of Southampton.

152. Fothergill, J., *Estimating the cumulative probability of failure data points to be plotted on Weibull and other probability paper.* IEEE Transactions on Electrical Insulation, 1990. **25**(3): p. 489-492.

153. Matsubayashi, Y., et al., *Relationship between dielectric strength and mechanical properties of alumina films fabricated by aerosol deposition.* Ceramics International, 2022. **48**(19): p. 28815-28821.

154. Xiang, D., L. Liu, and Y. Liang, *Effect of hard segment content on structure, dielectric and mechanical properties of hydroxyl-terminated butadiene-acrylonitrile copolymer-based polyurethane elastomers.* Polymer, 2017. **132**: p. 180-187.

155. Azmi, A., et al., *Structure-dielectric property relationship in polypropylene/multi-element oxide nanocomposites.* IEEE Transactions on Nanotechnology, 2021. **20**: p. 377-385.

156. Guo, X., et al., *Investigation of the Space Charge and DC Breakdown Behavior of XLPE/α-Al2O3 Nanocomposites.* Materials, 2020. **13**(6): p. 1333.

157. Sikorski, W., et al., *On-Line partial discharge monitoring system for power transformers based on the simultaneous detection of high frequency, ultra-high frequency, and acoustic emission signals.* Energies, 2020. **13**(12): p. 3271.